THERMO-MECHANICAL MODELING OF LASER-ASSISTED SIDE MILLING PROCESS

DISSERTATION

Submitted in Partial Fulfillment of the Requirements for

the degree Doctor of Technical Sciences in

Mechanical Engineering

by

Dipl.-Ing. Hassan Adrian Zamani

Dissertation Committee:

Prof. Christof Sommitsch
Prof. Bernhard Sonderegger

Faculty of Mechanical Engineering and Economic Sciences

Institute of Materials Science and Welding

August 2014

Declaration

I declare in lieu of oath, that I wrote this thesis and performed the associated research myself, using only literature cited in this volume.

Abstract

Lately, the high cost and low productivity of machining hard materials such as Ti-6Al-4V has drawn major attention to the development of a modular and scalable tool system with integrated laser as one piece of equipment. The present study focuses on a new concept of laser-assisted milling with a spindle and tool integrated laser beam guiding. A modular tool with the mechanical interface is joined to a spindle which consists of a focal lens and a prism for deflecting the laser beam on the working plane. The laser beam is located in front of the cutting insert and moves synchronously with the cutter. In order to optimize the process with respect to the force reduction, various machining conditions were investigated, both experimentally and by simulation. For this purpose, the material behavior at high temperature was described with the thermo-plastic shear instability consideration for the Johnson-Cook equivalent stress. The approach was compared and validated with the results of hot comparison tests. Furthermore, a completely coupled moving laser heat source with a mechanical simulation has been developed to link the laser parameters to machining conditions. Finally, the numerical 3D FEM simulations were carried out with the commercial software DEFORM 3D. A Johnson-Cook type material model was applied in the simulation and specifically modified for very high strain rates and system temperatures, which is called nonlinear thermal softening (NTS). In this material modeling approach with respect to the thermo-plastic shear instability attention, the thermal softening coefficient does not drop more linearly as the strain rate exceeds a critical value. Results such as temperature distributions and maximum cutting forces could directly be compared to the experimental findings. The simulation results expressed ample agreement with the experimental results.

Kurzfassung

In letzter Zeit haben die hohen Kosten und die niedrige Produktivität der Zerspanung harter Materialien wie beispielsweise Ti -6Al-4V große Aufmerksamkeit auf die Entwicklung eines modularen und skalierbaren Werkzeugsystems mit integriertem Laser gelenkt. Die vorliegende Studie konzentriert sich auf ein neues Konzept des laserunterstützten Fräsens mittels Spindel und werkzeugintegrierter Laserstrahlführung. Ein modulares Fräswerkzeug ist verbunden mit einer mechanischen Schnittstelle in einer Spindel, welche eine Fokusierlinse und ein Prisma zum Lenken des Laserstrahls auf der Bearbeitungsebene hat. Der Brennfleck befindet sich vor der Schneide und bewegt sich synchron mit der Schneide. Um das Verfahren in Bezug auf die Kraftreduzierung zu optimieren, wurden verschiedene Bearbeitungsbedingungen untersucht, sowohl experimentell als auch mit Simulation. Zu diesem Zweck wurde das Werkstoffverhalten bei hoher Temperatur mit der thermoplastischen Scherinstabilität für die Johnson-Cook Vergleichsspannung beschrieben. Der Ansatz wurde verglichen mit den Ergebnissen eines Warmstauchversuches. Ferner wurde eine vollständig gekoppelte bewegte Laserwärmequelle mit mechanischer Simulation entwickelt, um Laserparameter mit den Zerspanungsbedingungen zu verbinden. Schließlich wurden die numerische 3D FEM Simulationen mit der kommerziellen Software DEFORM 3D durchgeführt. In der Simulation wurde ein Materialmodell von Johnson-Cook angewendet, welches speziell für hohe Dehnraten und Temperaturen modifiziert wurde. Dieses nennt sich nicht-lineare thermische Entfestigung (NTS). In diesem Ansatz zur Modellierung des Materials ausgerichtet auf die adiabatische Scherinstabilität sinkt der thermische Entfestigungskoeffizient und nicht mehr linear, sobald die Dehnrate einen kritischen Wert überschreitet. Ergebnisse wie Temperaturverteilungen und maximale Schnittkräfte wurden mit den experimentellen Ergebnissen verglichen. Die Simulationsergebnisse erzielten eine solide Übereinstimmung mit den experimentellen Ergebnissen.

Acknowledgments

I would like to express my deepest gratitude and respect to my advisor, Professor Christof Sommitsch, Dean of Faculty of Mechanical Engineering and Economic Sciences and Head of Institute of Materials Science and Welding, for his guidance, motivation and intellectual support during the course of my doctoral research.

I am indebted to Professor Bernhard Sonderegger who is also a member of my committee. He has contributed to the overall research and his efforts have been instrumental for integrating my work on developing thermal and material modeling within scientific goals of the thesis.

My appreciation extends to Professor Maria Cecilia Poletti for stimulating discussions and profound advice. She leads the team I was a member of in the area of material modeling and simulation. Warm appreciation is given to my other colleagues, Dr. Fernando Gustavo Warchomicka, DI Dilek Halici, who assisted me in performing hot compression tests.

My special thanks to DI Jan-Patrick Hermani, Frauenhofer Institute for Production Technology (IPT), for providing important collaboration in the manufacturing fields and performing laser assisted side milling tests and requiring measurements to determine of laser absorption coefficient. I am also grateful to Dr. Annette Walter, Sill Optics GmbH & CoKG, for her support in this work and for precise description of optical modules.

The research work presented in this Dissertation is part of the TooLAM project and I would like to acknowledge the financial support of the European Union and the Austrian Research Promotion Agency (FFG) within the EraSME program.

Finally, I would like to thank those who helped me during my study at the Graz University of Technology.

List of Symbols

A, B, C	material constants in Johnson-Cook material model
A_C	tool-work piece contact areas
A_{circle}	circular cross section
$A_{ellipse}$	elliptical cross section of beam
A_L	laser spot area
A_m	absorption coefficient
A_{mf}	absorption coefficient factor
A_{m0}	initial absorption coefficient
A_p	absorptivity of the parallel polarized ray
A_s	absorptivity of the perpendicular polarized ray
A_{sb}	assumed surface for shear band
A_{SP}	uncut chip thickness
A_w	work piece area
A_x	number of rotations at the measurement range
A_0, B_o, C_o, D_o	indices in transfer matrix
a, b, c, d, e	material constants in TANH material model
a_d	thermal diffusivity
a_e	width of cut
a_p	depth of cut
a_1	material constants for shear instability
a_2	material constants for nonlinear thermal softening
a_3	material constants for shear instability
b_1	material constants for shear instability
b_2	material constants for nonlinear thermal softening
b_3	material constants for shear instability
c_p	specific heat
D	material constants in TANH material model
D_c	damage evolution parameter
D_{CL}	Cockcroft and Latham damage value
D_{JC}	Johnson-Cook damage value
D_1	material constants for Johnson-Cook damage model
D_2	material constants for Johnson-Cook damage model
D_3	material constants for Johnson-Cook damage model
D_4	material constants for Johnson-Cook damage model
D_5	material constants for Johnson-Cook damage model
d_f	mill diameter
d_0	diameter of beam
F	tangential force
F_c	cutting force
F_{max}	maximum forces
$F_{max,i}$	local maximum cutting force
F_t	thrust force
f_z	feed per revolution
h	heat transfer coefficient between work piece-enviroment
h_{int}	heat transfer coefficient between work piece-tool
h_L	heat transfer coefficient between work piece-laser spot area
h_{SP}	instantaneous uncut chip thickness
$h_{SP,II}$	instantaneous uncut chip thickness at zone II
I	collimation lens position
I_L	laser power density
i	number of local maximum
K	beam quality number
k	shear flow stress AB
k_{AB}	shear flow stress along
l	length of shear zone

l_a	cutting length
L_{sb}	assumed thickness for shear band
l_w	work piece length
M^2	Beam Quality Factor
m	thermal softening component
m_0	initial thermal softening component
$\bar{m}$	shear factor
N	normal force
n	strain hardening component
n_{eq}	equivalent strain hardening exponent
$\vec{n}$	rotation velocity
P_L	laser power
p	mean compressive stress
p_A	compressive stress at point A
p_B	compressive stress at point B
$\dot{Q}$	heat flux
Q_L	laser input heat flux
q	heat
$\dot{q}$	heat flux density
$\dot{q}_a$	absorbed laser power density
q_f	generated heat due to friction
r_F	mill radius
r_o	transverse offset
r_{oB},θ_{oB},r_{oF}, θ_{oF}	input and output distance and angle respecting optical axis
r_0	radius of the laser beam
S	material constants in TANH material model
T_{AB}	temperature along AB
T_e	temperature of enviroment
T_{Le}	temperature of local enviroment
T_m	melting temperature
T_r	room temperature
T_{sL}	temperature of local surface
T_t	temperature of tool
T_W	initial work piece temperature
T_w	temperature of work piece
t_b	bottom time domains
t_i	interaction time
t_u	upper time domains
V	volume of work piece
V_{sb}	shear control volume
$\dot{V}_{SP}$	uncut chip volume rate
$V_{SP,II}$	volume of uncut chip at zone II
v_c	cutting velocity
v_f	feed velocity
W_p	plastic work
$\dot{W}_p$	plastic work rate (heat generated rate)
w_0	beam waist radius
$w_{0,A}$	focal beam radius
X_b	bottom work piece geometry ratio
X_u	upper work piece geometry ratio
$Z_{R,A}$	Rayleigh length
z	number of tooth

Greek letters

α	rake angle
α_A	cross section factor
β	heat partition coefficient

ε	equivalent (effective) plastic strain
ε_{AB}	equivalent strain along AB
ε_c	critical strain
ε_f	strain fracture
$\dot{\varepsilon}$	equivalent (effective) plastic strain rate
$\dot{\varepsilon}_m$	lower limit of the critical strain rate
$\dot{\varepsilon}_0$	reference strain rate
Δ	Laplace operator
Δf_x	componential displacements in X
Δf_y	componential displacements in Y
Δk	variation of the shear flow stress
Δs_2	thickness of shear zone
$\Delta\varepsilon$	different between the incremental equivalent plastic strains for an element
Θ	divergence angle
θ	incidence angle
θ_o	offset angle
θ_R	resultant force
λ	thermal conductivity
λ_f	frictional angle
λ_o	wave length
μ	Coulomb friction coefficient
ρ	density
σ_{AB}	flow stress along AB
σ_{eq}	flow stress
σ_H	hydrostatic pressure
σ_n	normal stress (contact pressure)
σ_1	positive part of the principal stress
σ_2	main normal stresses
σ_3	main normal stresses
φ	angular position of cutting point in the working plane
φ_a	exit angle
φ_c	engagement angle
φ_e	entrance angle
φ_f	feed angle
ϕ	shear angle

Bold letters

$\boldsymbol{k}$	extinction coefficient
$\boldsymbol{n}$	refraction coefficient
$\boldsymbol{\varepsilon}$	emissivity
$\boldsymbol{\sigma}$	Stefan–Boltzmann constant

Contents

1 Introduction

1.1 Motivation

The machining processes have the main share in manufacturing and shaping the diverse components in the industry. The key of sustainability in the machining processes can be defined with the following words involving its priority: to achieve high surface integrity with low costs and a high material removal rate. Apart from the complex geometry and outdated technology, this goal is not always accessible linking to the physical, chemical and mechanical work piece material properties.

Advanced materials such as Titanium alloys and Nickel-based super alloys are good representatives for so-called hard to machine material. Because of high strength at the moderate and high temperatures (which on the other hand makes plausible the application of these alloys in the aerospace industry), high hardness, low thermal conductivity and reaction with the tool material do not make the machining of these materials cost-friendly. More specifically, here, the high cost means excessive tool wear which increases the number of used cutting inserts during machining of super alloys. To improve the machinability of this material, various innovative and competitive machining processes are applied where the most relevant processes are ultrasonic machining, plasma machining, high pressure water jet machining, electro-discharge machining and laser-assisted machining.

The heating of material to reduce the mechanical strength and to reach a softening temperature using the laser beam in front of the cutter is called laser-assisted machining (LAM). The hybrid machining process decreases the cutting forces and the subsequent tool wear and also presents a positive effect on the surface integrity. On the other hand, absence of coolant also supports environmental preventive care.

The central aim of using the localized heat source is the improvement the machinability without adverse consequences on the finished part. The fundamentals of the LAM process look easy to understand and logical, but it gives no warranties for sharing only benefits of the laser. There are many factors from different of points of view which can bring entirely inverse results than expected initially. As a clear example, the overheating from a material science point of view sometimes results in surface hardening instead of softening in alloys with a potential to phase transformation (LAM of Ti-6Al-4V) among other forms of thermal loading. This adversely affects the machining process in terms of efficiency and profitability.

Therefore, as first steps in the realization of an effective laser assisted machining, the major influencing factors related to design, machining, and laser parameters should be brought together with the material properties.

1.2 Objectives of Research

A thermo-mechanical process model for the laser assisted machining of high strength metallic and ceramic materials will reduce time consuming and expensive testing periods. A finite element model (FEM) for a laser-assisted milling with the integrated optical and mechanical modules can be used as an auxiliary tool to predict the required machining and laser parameters for different materials, operation modes and target geometries. Such a model is highly desired by respective end users and will be helpful to optimize any laser-assisted cutting process such as milling and turning.

Consequently, the terminal objective of this thesis is identified as:

1. Using the adiabatic shear instability criterion to model chip formation (2D) and model validation via compression tests
2. To adjust the material modeling approach for 3D simulation of laser-assisted milling and validation via the resulting cutting forces
3. To develop and validate a machining integrated 3D laser heat source model
4. The process- and geometric-dependent optimization of machining operations with respect to force reduction

1.3 Organization of Dissertation

The dissertation involves four chapters:

The present chapter is divided into two parts. After a short review of the cutting processes and applied analytical approaches, the state of research of laser assisted machining in the case of Ti-6Al-4V will be outlined.

Chapter 2 introduces a novel laser assisted milling in detail (optical elements, mechanical components and process control conditions) and presents experimental results with various laser and machining parameters.

Chapter 3 focuses on the numerous material modeling approaches used to predict the chip morphology and validation compression test. Also, the shear instability criterion will be modified for 3D material modeling.

Chapter 4 presents a 3D simulation of the novel laser assisted milling. First, the applied three dimensional thermal model will be described in detail. Furthermore, the experimental and numerical trials to determine the absorption coefficient for the according processes will be recounted. Also, it gives a short observation of the frictional and heat transfer behavior at the tool and work piece areas. Finally, the measured result of laser assisted side milling will be compared to the 3D simulation results.

1.4 Principle of Orthogonal Cutting

The main difference in the modeling of machining operation compared to the other forming processes can be stated within the deformation zone. The plastic deformation in the machining process is limited only in the small area around the tool (cutter) tip. If the cutting edge is perpendicular to both the cutting velocity and feed velocity direction, it is called orthogonal cutting. The orthogonal cutting process is normally used for the observation and understanding of the cutting process and the chip formation. The forming zone in the cutting process is divided into three sub-zones which are called primary, secondary and tertiary shear zone. Figure 1-1 shows the location of these zones in orthogonal cutting. The primary shear zone is a region which the material flow direction changes along cutter rake face. Then the chip is formed. The high strain (up to 6), strain rate (up to 10^{6} s^{-1}) and temperature (over 300 °C) are identified as attributes of this zone [1]. The frictional phenomena at the tool rake face-chip interface causes plastic deformation which is known as secondary shear zone. Here, the interface temperature can be achieved even up to melting temperature of the work piece material. The secondary shear zone is normally divided into two sticking and sliding regions [2, 3]. The tertiary shear zone is created as a result of the tool clearance face with the machined surface. The compression stresses in the tertiary shear zone are more remarkable than the shear stresses.

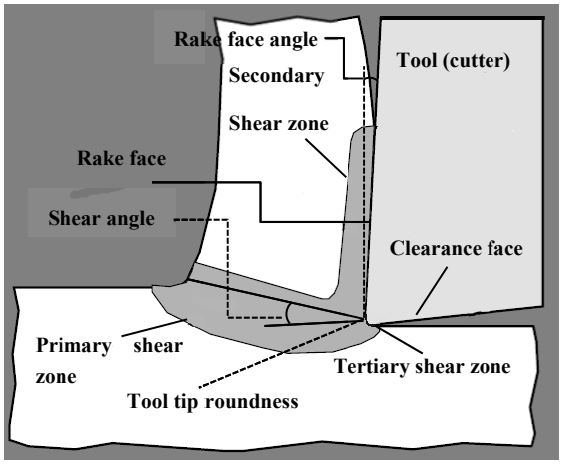

Figure 1-1: Deformation zones in the orthogonal cutting process [4].

Each of these forming zones is at the center of attention from the modeling of machining process point of view. Broadly speaking, the material modeling and process force modeling focus on the primary shear zone, friction, heat transfer and tool crater wear modeling consider the secondary shear zone. The modeling of the residual stresses in the finished material, surface integrity and tool flank wear modeling take into account the tertiary shear zone.

1.4.1 Chip Formation Mechanisms

Chip formation in machining can be split into two groups: continuous and segmented chip formation. The type of chip formation depends on the plastic material behavior in the cutting condition. In another words, with increasing the formability of material, the tendency of continuous chip formation increases, too. The stress-strain curve in terms of formability or the Friedman diagram [5, 6] in terms of fracture mechanisms (ductile metals do not fracture on the shear plane) are a good reference to define the type of chip formation. Continuous chip formation delivers a better performance regarding a reduction in amount and fluctuation of cutting forces as well as surface finish [7, 8].

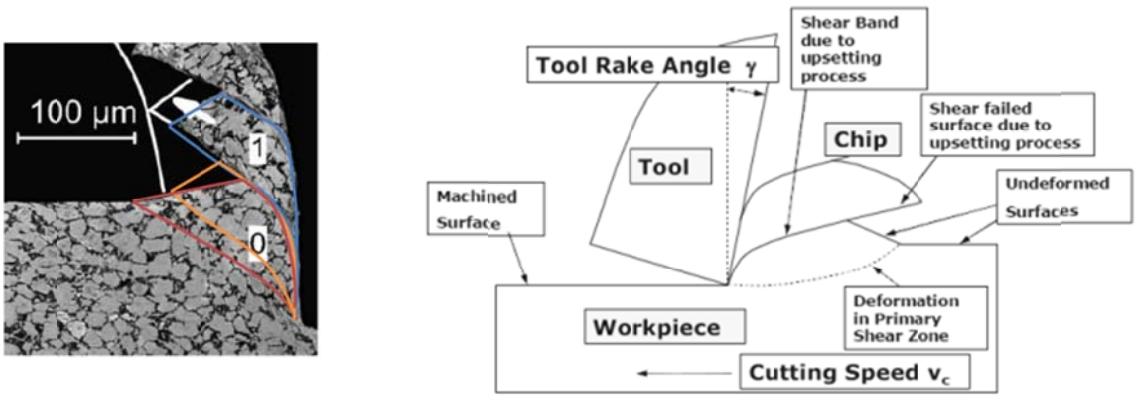

Figure 1-2: Chip segmentation mechanism according to Komandary [9].

The segmented chip formation can be attributed to thermo-plastic instability [10] at high cutting speeds. Poor thermal properties of work piece material such as thermal conductivity and thermal capacity (e.g. titanium and nickel alloys, hardened steels) shift the segmentation to more moderate cutting speeds. Komandary states a catastrophic shear (adiabatic shear) takes place as the thermal softening overcomes the strain hardening effect. This means that the heat generated due to the plastic deformation localizes in a narrow region with high shear strain. An approach to formation of the segmented chip begins with a shear deformation along the maximum shear strain direction in the primary shear zone which causes an inclination at the free surface of the work piece. At the same time, with advancing the tool, the materials in front of the tool cutting edge are upset and have a tendency to move along the maximum shear strain direction. The thermo-plastic instability promotes this displacement in the form of slippage (Figure 1-2) [11, 12].

1.4.2 Analytical Calculation of Machining

The analytical calculation in machining process is restricted to orthogonal cutting for continuous chip formation (steady state) and sharp tool. On the assumption that width of cut is very much bigger than depth of cut, the rigid plastic plan strain can be achieved. The goal of analytical models is to determine the angle of maximum shear strain direction with the cutting direction which is called shear angle, ϕ. The main approach to achieve this goal can be derived from the flow field (velocity discontinuity or streamlines).

In early studies [2, 3, 13, 14], the deformation zone is confined to a plane with a discontinuity in velocity, however is known now that shear deformation occurs in a deformation zone where cutting velocity changes continuously into a chip velocity. Simple relations help us to find first predictions in the cutting of metals. These relations consist of work piece velocity where similar to a turning process, the cutter does not move. As the work piece velocity transits the shear plane, it changes into chip velocity. With respect to the rake face angle (inclination of cutter which can be positive or negative) and assumed shear angle, the velocity on the shear plane can be determined. The proportion of tangential and normal velocity on the shear plane expresses the shear strain.

Ernst and Merchant developed [3, 14] a purely mechanical model to determine the shear angle. The model does not consider the effect of stain, strain-rate, and temperature on material behavior during the cutting. They proposed that the shear angle trend to reach a value on the required energy is minimal. In this model, the deformation zone is also taken as a surface where work piece velocity changes instantaneously into chip velocity with considering a tangential component of velocity. Instantaneous change in velocity means that the maximum shear strain rate and consequently the maximum shear stress take place on this surface. The maximum shear surface (it is a straight line), acts like a slip line and the mean compressive stress is constant along the shear plane. Furthermore, the shear flow stress is constantly

parallel to the slip line (no work hardening). From Merchant's force circle [14], the cutting force (F_c) and thrust (or feed) force (F_t) can be found. All forces on the chip tool interface and across the shear plane are in equilibrium. As mentioned above, the minimum cutting force takes place on the shear plane; this means that the derivation of the cutting force with respect to the shear angle should be equal to zero:

$$\frac{dF_c}{d\phi} = 0 \qquad \textbf{Equation 1-1}$$

and from that the shear angle can be calculated as:

$$\phi = \frac{\pi}{4} + \frac{\alpha}{2} - \frac{\lambda_f}{2} \qquad \textbf{Equation 1-2}$$

where α is the rake angle and λ_f is frictional angle. With the assumption that the tool tip is sharp, the same resultant force which is divided into normal (F) and tangential (N), acts on the tool-chip interface. Then, basing Coulomb's law, the coefficient of friction at the tool-chip contact area is (in fact, the cutting and thrust forces can be measured easily by a dynamometer in orthogonal cutting):

$$\mu = \frac{F}{N} = \frac{F_c + F_t \tan\alpha}{F_c + F_t \tan\alpha} \qquad \textbf{Equation 1-3}$$

In a similar manner, Rowe and Spick [3, 14] propose that the shear plane is located where the total energy on the shear plan and on the rake face is minimal. They also state that the increase in the contact length and shear flow stress leads to the higher rate of work done and its minimum shifts to the lower values of ϕ. Consequently, the cutting and thrust forces increase.

Attempts by Lee and Shaffer [2, 14, 15] to obtain the shear angle by means of a slip line field were concluded in following relation:

$$\phi = \frac{\pi}{4} + \alpha - \lambda_f \qquad \textbf{Equation 1-4}$$

However, the mean compressive stress (p) and the shear flow stress (k) remain constant in their simple triangular plastic zone with parallel slip lines. Chakrabarty [14] proposes a slip line model with respect to a linear strain hardening effect above shear plane where the mean compressive stress varies with ϕ, $\left(\phi \leq \frac{\pi}{4}\right)$:

$$p = k\left(1 + \frac{\pi}{2} - 2\phi\right) \qquad \textbf{Equation 1-5}$$

The triangular region undergoes a uniform compression (above the shear plane) with an amount less than two times of the shear flow stress for a work hardened material.

Also, there are some models by Fang and Dewurst [15, 16] that take into account the built-up edge and rounded edge tool, when the chip is curled because of forgoing the strain hardening effect. Since the slip line theory is complicated and is not easy to put into effect realize as a computer program, its application is limited in the calculation of the cutting process.

A more realistic and predictive analysis of the cutting process can be achieved with considering the strain hardening, strain rate and temperature on the material properties, which was introduced by Oxley [14]. In aim of a comprehensive view of this model, more details are provided here. First, by Oxley's model it is considered that the shear flow stress changes along the slip lines. Oxley took the shear zone in his model between two parallel boundary lines (CD and EF, as is illustrated in Figure 1-3) and shear flow stresses along AB, CD and EF were taken while the shear flow stress changes when the material moves form CD to EF. Based on the slip line theory, AB should be rotated with $(\frac{\pi}{4} - \phi)$ until it meets the free surface. The mean compressive stress on the free surface is equal to the shear flow stress on the AB.

$$\frac{p_A}{k_{AB}} = 1 + 2\left(\frac{\pi}{4} - \phi\right) \qquad \textbf{Equation 1-6}$$

and the variations of mean compressive stress along the shear plan (AB) can be calculated using the length (l) and thickness of shear zone (Δs_2):

$$p_A - p_B = \frac{\Delta k}{\Delta s_2} l \qquad \textbf{Equation 1-7}$$

The variation of the shear flow stress along the shear (Δk) zone can be calculated by the separation into the partial variation and using a flow stress equation. Also, the shear strain rate can be determined by the shear velocity on the AB to the shear zone thickness while the shear strain is the fraction of shear velocity on the normal component of velocity on AB. With the assumption of the constant shear flow stress and linear variation of p along AB, the angle between AB and resultant force (θ_R) can be determined from a shear angle and friction angle subtract and rake angle:

$$\theta_R = \phi + \lambda_f - \alpha \qquad \textbf{Equation 1-8}$$

Based on Boothroyd's work [14] from a power balance, the temperature evolution and average temperature in the primary shear zone was calculated by Oxley. The triangular secondary shear zone was assumed as a rectangular and the tool-chip interface undergoes a full plastic deformation.

Oxley's theory was modified in terms of shape of primary shear zone (unequal divided shear-zone model or pie-shaped model) by several researchers [17, 18]. Another application of Oxley's approach is to invert determination of material constants in constitutive material models [18, 19, 20, 21, 22] from the measured process forces. Oxley's model more than other analytical methods calculates machining problems. Also, Oxley's approach was used with other thermal model (primary and secondary with assumption of moving heat source models) [23] and different constitutive material models [24, 25].

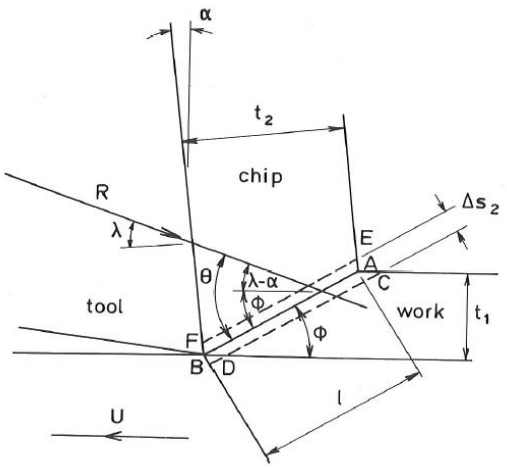

Figure 1-3: Parallel primary shear zone in Oxley's model [14].

Latterly [17, 24, 25], Oxley's model was extended for the JC material model, history dependent power law material and the mechanical threshold stress model. Moreover, they assumed that the β as a fraction of total plastic works up to AB which converts to heat:

$$\int_{T_W}^{T_{AB}} \rho c_p dT = (1-\beta) \int_0^{\varepsilon_{AB}} \sigma_{eq} d\varepsilon \qquad \textbf{Equation 1-9}$$

Furthermore, the average shear stress along the shear plan was adopted with the deformation work per unit volume in the primary shear zone which introduces the effect of strain and temperature in the Hencky equation along the alpha slip line. Another study of Lalwani et al. [25] offered an equivalent strain hardening coefficient instead of n in Oxley's model for Johnson-Cook's material model:

$$n_{eq} = \left(\frac{d\sigma_{AB}}{d\varepsilon_{AB}}\right)\left(\frac{\varepsilon_{AB}}{\sigma_{AB}}\right) \qquad \textbf{Equation 1-10}$$

1.5 The Finite Element Method in Machining

Today, most studies in modeling of machining utilize the Finite Element Method as an effective instrument to solve machining problems. The application of FEM to machining

covers the extensive areas such as chip formation, thermal and mechanical loading as well as surface integrity and tool wear [26, 27, 28, 29, 30, 31, 32]. The machining process involves high strain rate, strain and temperature in a very small region in comparison to the whole work piece, thus it is not an easy task for numerical modeling. According to special aspects of simulation of machining, Lagrangian, Eulerian and Arbitrary Lagrangian-Eulerian (ALE) formulation have been used [33, 34, 35]. The determination of a maximum shear angle as a classical problem in analytical solutions is no more significant in FEA, and instead of it, definitions of the proper material model [36, 37], friction model [38, 39, 40], chip formation, mesh generation and also computation time play a central role to get realistic and predictive results. Furthermore, thermo-mechanically coupled modeling in FEA enables researchers to study the effect of generated or input heat on the mechanical, deformation and microstructural behavior during the machining process.

In order to give an overview of how far the analytical solutions are from the FEM simulations, the approach used by Lalwani was calculated in this work for an orthogonal cutting of Ti-6Al-4V was compared with the common 2D-FEM calculation at the same physical and mechanical boundary conditions (density= 4302 Kg/m³, for simplification thermal conductivity and specific heat were taken from linearization of data, which are listed in Table 3-3 in section 3.3 5.8609+0.0147T W/m°C and 541.19+0.2168T J/Kg°C, respectively). The required input parameters for this calculation are cutting velocity =120 m/min, depth of cut=0.5 mm, width of cut=10 mm, rake face angle=11° and initial work piece temperature=25 °C). The required material constants were taken form Lee-Lin [41] work, which are listed in Table 3-1 in section 3.1.The calculated forces, temperature at shear plane, temperature at tool-chip interface, strain and strain rate distribution are presented in Figure 1-4.

The first and most important advantage of an analytical solution is the swift computation time and that it provides only a comparative value as a result which makes the interpretation of results easy. As it can be observed, the divergence between the analytical and FEM solution in the case of cutting force in the X direction is relatively low (3.2 %) and for the Y direction it is up to 30% which is an acceptable successes for fans of these methods. The maximum strain and temperature between the tool face and chip also expresses a good correlation between two results (up to 6 % for interface temperature and 16 % for the related strain).

In spite of the fact that the clarification of the strain, strain rate and temperature in the primary shear zone are not in consistence with each other, the analytical solution did not have any information about the distribution of each state variable. It should be mentioned that today the FEM is as an efficient routine to solve the diverse conventional and non-conventional machining processes.

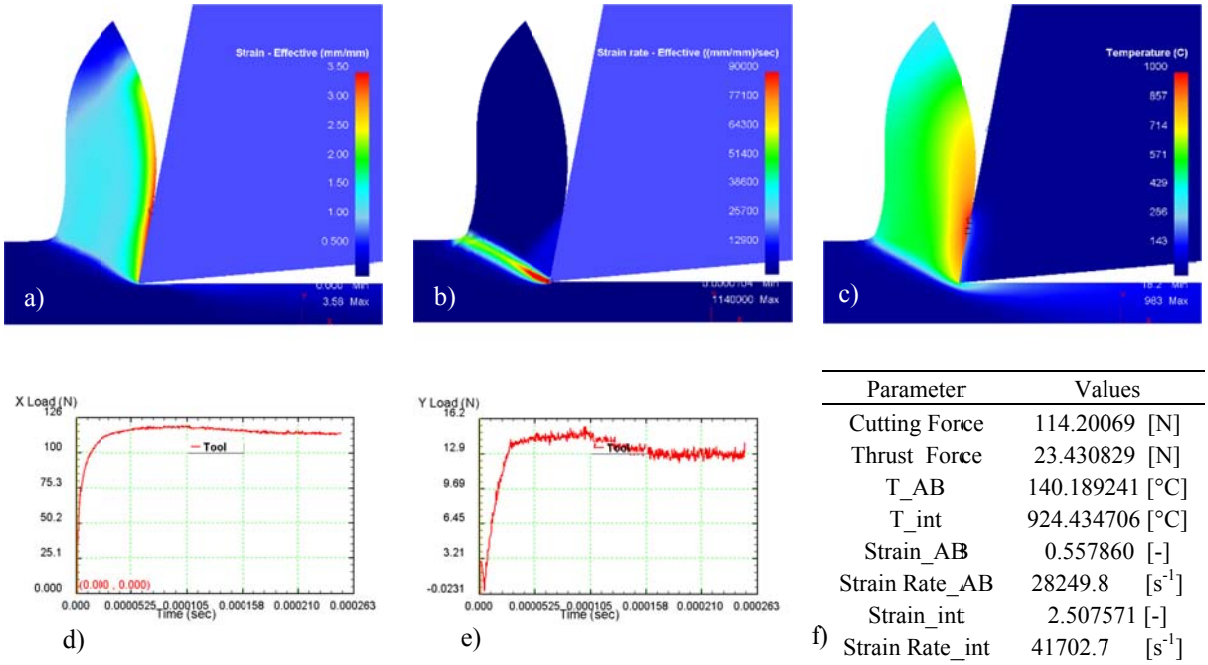

f)

Parameter	Values	
Cutting Force	114.20069	[N]
Thrust Force	23.430829	[N]
T_AB	140.189241	[°C]
T_int	924.434706	[°C]
Strain_AB	0.557860	[-]
Strain Rate_AB	28249.8	[s^{-1}]
Strain_int	2.507571	[-]
Strain Rate_int	41702.7	[s^{-1}]

Figure 1-4: The comparison between the (a) strain, (b) strain rate, and (c) temperature distribution and (d, e) cutting forces with (f) analytically results of orthogonal cutting of Ti-6Al-4V (cutting velocity=120 m/min, rake face angle=11 °)

1.6 Machining of Ti-6Al-4V

Titanium changes its crystal system at 882 °C from the body-centered cubic (bcc) β-phase into the hexagonal close-packed (hcp) α-phase which is steady at room temperature. This transformation temperature can be increased or decreased by some alloying elements, what are known as α-stabilizers (Al, Sn, O, N) and β-stabilizers (V, Mo, Fe, Cr, Mn), respectively. Ti-6Al-4V as an (α+β)-alloy has a β-transus at 1000 °C. Depending on the previous forming process temperature and cooling rate, the microstructure of (α+β)-alloys can be varied from equiaxed (below the β-transus), fully lamellar (above the β-transus), or bi-modal α-microstructure, leading to different mechanical properties. The different microstructural morphology is illustrated in Figure 1-5. In general terms, the fully lamellar microstructure is more adequate for machining. The lamellar α-phase (lath-like) is a result of the precipitation of the α-phase from the retained β. The lamellar α-microstructure has less hardness in comparison to the equiaxed morphology which leads to a reduction of tool wear, cutting force value and fluctuations [42, 43]. The thickness of α-phase lamellae depends on the cooling rate inversely. With increasing the lamellae α-phase, the material sticks less in the tool tip which decreases the built up edge [42]. The common as-received condition of Ti-6Al-4V for the machining is the annealed (at 720 °C) with bi-modal microstructure.

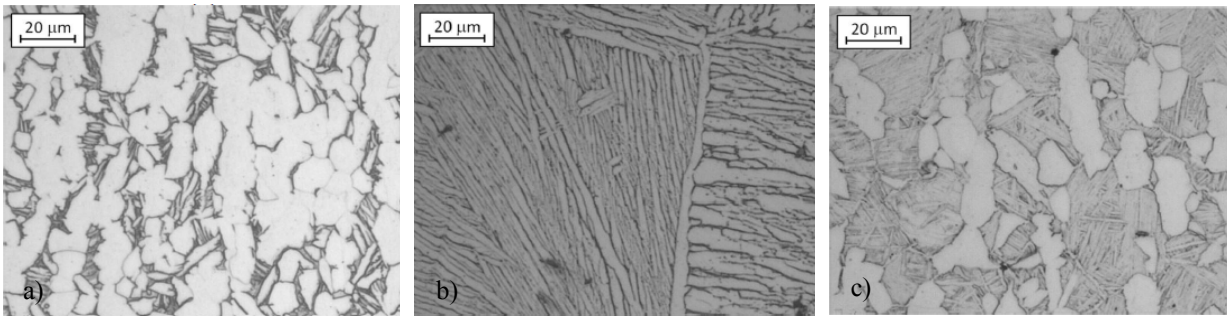

Figure 1-5: Microstructural morphology of Ti-6Al-4V (a) equiaxed (b) fully lamellar (c) bi-modal α-microstructure [42].

As mentioned, titanium due to some inherent properties is not popular in machining. Several factors such as low thermal conductivity (it leads to temperature localization on the tool-chip interface where it increases thermal loading in tool approximately two times more than the machining of carbon steels [44]), low elastic modulus, high strength and hardness even at elevated temperatures, high chemical reactivity with tool material at cutting temperature and welding of the work piece material to the tool (built-up edge) support this drawback. These aspects, beside the arising tool wear and machining costs cause the poor surface quality. There are a number of standard strategies in machining of titanium alloys which make the machining of Titanium alloys easier like low cutting speed, positive rake angle, sharp edge tool, high feed rate, large amount of cooling fluid, continuous feeding, tool coating [45]. In the cutting velocity between 30 up to 90 m/min [44, 46] the tool life (carbide) with increasing of feed rate and cutting velocity dropped dramatically (up to four times less). Since the frictionally generated heat increases with velocity at very high cutting velocities (more than 120 m/min [47, 48]), it decreases the cutting forces indirectly.

The tool wear phenomena in machining of Ti-6Al-4V alloy consist of crater wear (on the rake face), flank wear (on the clearance face), notch wear and chipping. Using the cemented tungsten carbide (WC-Co) tool is appropriate for cutting speeds under 50 m/min. The coated carbide tools (PVD multilayer TiN/TiCN/TiN or TiCN+Al2O3) can be reached at a higher cutting velocity (up to150 m/min) [49]. During the machining of Ti-6Al-4V alloy with carbide tools, cobalt can be diffused by cutting the tool into the titanium chip due to high interface temperature and hard WC grain carried away with it [50]. A forming of interlayer titanium carbide (TiC) as a result of diffusion of titanium atoms into the carbide tools and making a seizure zone shifts the cobalt diffusion to the higher temperatures (750 °C). The high speed machining (up to 350 m/min) of Ti-6Al-4V can be carried out with cubic boron nitride cutting (CBN) and polycrystalline diamond (PCD) tools. As shown in Table 1-1, the softening of these tool materials takes place at higher temperatures at which the softening of Ti-6Al-4V is already achieved. Also, the diffusion of nitrogen atoms from the tool and reaction with titanium begins at 1100 °C, where an increase in the tool wear will appear.

Similar to the WC-tools, the formation of a seizure titanium carbide (TiC) layer reduces the diffusion rate at the interface of the tool-chip [49].

Table 1-1: Softening points of tool materials [49].

Tool Material	Softening point temperature [° C]
High speed steel	600
WC	1100
Al_2O_3	1400
CBN	1500
Diamond	1500

1.7 Fundamentals of Laser Assisted Machining

The idea of laser heating comes from locally heating the work piece before the cutting by using a high energy density. The laser beam is capable of being focused which makes it possible to heat only a small area near the cutting tool (cutting insert) without any additional thermal loading the insert with the adjusting the laser spot position [45]. The laser source is also simple to control and it is suitable for control system programing. An effective control system supports the fulfilling of the process boundary condition like laser power, machining velocity, feed rate, and depth of cut.

Around ten years after developing the laser by Theodore Maiman in 1960, the research and investigation in the laser assisted machining of aerospace alloys with the CO_2 laser began [51]. The CO_2 laser was first used for laser assistance, because it generated sufficient power. Today, the fiber lasers (Nd: YAG, Yb: YAG) are able to reach high powers and because of the high absorption advantage in processing metals over a shorter wavelength, lasers are used frequently. However, the wide range of (CO_2 or fiber laser) wavelength from 300 to 10,000 nm and cost effective lasers provide a high potential for material processing.

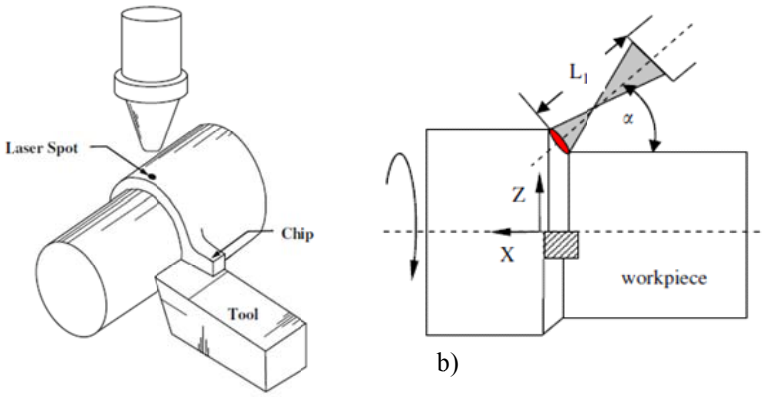

Figure 1-6: Laser assisted turning (a) laser beam normal on the work piece (b) laser beam with incident angle on the chamfer [52].

The most significant machining processes which are interesting for laser assistance are turning and milling. In the turning process where the work piece rotates and cutting tool does not move, the using of the laser equipment and set-up (the position of laser spot on the work piece surface and beam angle) is easier in comparison to the milling process. It means that the laser equipment does not need to move in the turning process [52]. Figure 1-6 shows the laser assisted turning process with a normal irradiation of laser beam on the work piece and the case of laser irradiation on the chamfer surface (cutting edge) with an incident angle.

Figure 1-7 shows the principle and features of two possible approaches in laser assisted milling. There are two alternatives for integrating the laser beam into the milling process: first, the laser as a separate apparatus outside of the tool-spindle mill system; second, as a tool-spindle integrated laser system in terms of equipment without any additional peripheral device. With the laser irradiated form outside of the tool, the production boundary condition such as internal bore diameter, spindle-mill diameter, the tool length does not affect the process realization. The laser beam movement corresponds only to the tool movement in the feed direction. The feed direction velocity is slower than the tool rotation velocity which makes it possible to apply low laser powers. However, because of that, the laser device cannot accompany the milling tool overall, and the machining of complex geometry is not conceivable.

The laser beam integrated tool-spindle system [53, 54, 55] is an effort to make the laser assisted milling a normal routine for machining of hard to machined material in the automotive and aerospace industries. As the irradiation of the laser beam is only limited on the cutting edge surface, the risk of undesirable microstructure transformation is decreased. Although this approach opens new possibilities, the realization and process control of a laser beam integrated tool spindle system is challenging. A consistent reduction of forces in three directions and consequential tool wear demand a uniform heat distribution in the according uncut chip volume before the cutting insert [56]where the milling direction varies. Only as an example here, every machine vibration which causes the non-equivalent machine mass distribution and especially at high rotations velocities changes the laser beam position. It means the good result of LAM is always in connection with a construction of mechanical parts, arrangement of optical elements, a maintainable process control and material depending thermal, mechanical and kinematical boundary conditions. The fabrication and process boundary conditions accompanied with a related process control will be discussed in detail in the next part.

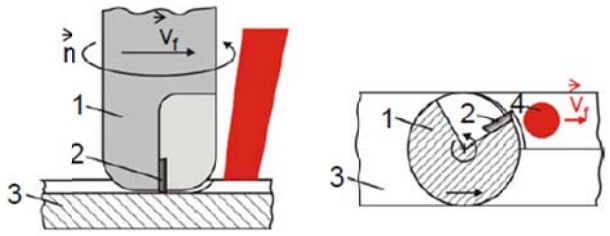

- Irradiation in front of the milling spindle on the work piece surface
- Movement of laser spot in feed direction
- Laser spot diameter ≈ width of cut

➔ Extensive irradiation and thermal damage of work piece and cutter insert

➔ Not satisfied for 3D milling

➔ Permanent maintenance of optical elements

- Irradiation in front of cutter insert on the cutting edge
- Movement of laser with cutter
- Laser spot diameter ≈ cutting edge surface

➔ Exact irradiation and low thermal damage of work piece and cutter insert

➔ 3D milling possible

➔ Protection of optical system

- 1: milling tool, 2:cutting insert, 3: work piece, 4: laser spot
- v_f: Feed velocity, $\vec{n}$: rotation velocity

Figure 1-7: The difference between two laser assisted milling processes according to the position and delivery of laser beam [57].

1.8 Laser Assisted Machining of Ti-6Al-4V

In order to make the machining of titanium easier, the work piece temperature increases locally in front of cutting zone using laser beams. As a result, flow stress decreases and total cutting forces requirements come down. However, the temperature of machined work piece should be kept below β-transus temperature (1000 °C), which, as mentioned before, results in an undesirable microstructure variation. The martensitic transformation (as a non- diffusional phenomenon) in the laser assisted machining of Ti-6Al-4V is relevant, which causes surface hardening, micro crack generation and cutting insert collapse. For this purpose, Figure 1-8 shows a CCT diagram for Ti-6Al-4V alloy. It can be seen as temperature exceeds 1000 °C, a cooling rate greater than 3 $°Cs^{-1}$ [58] is enough for presenting martensitic transformation (α'(α")) in microstructure, as the cooling rate arises up to 18 $°Cs^{-1}$, can be expected a fully martensitic microstructure. Even temperatures over 850 °C (especially by using high pressure air as process gas) leads to a partially martensitic transformation. These temperatures are achieved easily in LAM processes on the surface work piece. Here it should be mentioned that at slow cutting velocities, the input heat flux has adequate time for penetrating through

the work piece which can be useful to minimize and save the heat input. But on the other hand, the risk of phase transformation in machined surfaces increases. Obviously, for high velocities, the request of high powers increases. An important guideline in LAM of Ti-6Al-4V can be stated like this: the temperatures at the lower limit of depth of cut should be lower than 800 °C. Here, also the evaluated temperature in the tertiary shear zone should be considered (100-150 °C).

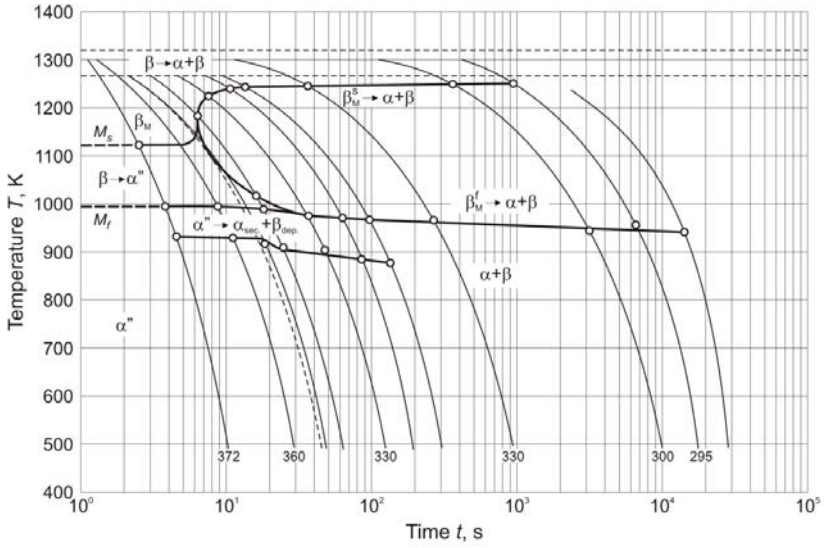

Figure 1-8: CCT diagram for Ti-6Al-4V alloy [58].

As investigated by some researchers [52], amount and fluctuation of all force components (feed, thrust and cutting force) during LAM due to the softening of the work piece are significantly reduced. However, LAM process parameters (laser power, laser spot size and incident angle) and cutting condition (cutting speed, feed rate and depth of cut), which have an effect on the heat input and the heat transfer, affect the amount of the reduction of force components.

Sun and Brandt [59] investigated the effect of laser beam on the chip formation and morphology at three different cutting velocities (20, 80, 230 m/min) in the case of laser assisted turning. The presented chip segmentation at low velocities in LAM in comparison to the conventional machining is a result of molten layer in the cutting zone. As the surface temperature exceeds the melting point of titanium (Ti6Al4V), the formability drops dramatically because of surface or grain boundary melting. In the conventional machining of titanium alloys, chip segmentation can be attributed to thermo-plastic instability at high cutting speeds.

Surface quality in LAM of titanium alloy is analyzed from the viewpoint of mechanical (plastic deformation, micro- and macro cracking, residual stress), metallurgical (transformation of phases, grain size) and thermal (heat affected zone) aspects [60, 61]. In general, the surface integrity in LAM is better than the conventional machining which leads to

higher fatigue strength. LAM does not affect the surface roughness of machined surface in comparison to conventional machining. The surface roughness is between 0.4 and 0.6 μm independent of the laser power. In LAM, forces (stresses) required for material removals are reduced and the common defects such as grain pull-out and material build-up are less than the conventional case. The compressive residual stresses move in the direction of tensile stresses in LAM. This effect is more considerable with increasing the laser power and decreasing the cutting speed. Distinctive microstructure and hardness changes were not reported in literature. The microstructure is principally affected by temperature alteration and the heat affected zone is removed mainly by machining. However, it has been observed that the density of twining [62] (main deformation mechanism in Titanium with hcp structure) in the surface layer in LAM is lower than in conventional machining.

According to the tool wear during LAM of Ti-6Al-4V, two points should be considered; the reaction of titanium with the tool material (wear diffusion mechanism) increases with the temperature, and parallel to it, the cutting forces and the mechanical load created on the tool surface, respectively. Dandekar [61] showed that the cobalt-diffusion increases as long as the material removal (the material temperature as it moves in the primary shear zone) temperature exceeds an optimum temperature. Using the liquid nitrogen (LN2) for the cooling of the rake face and as well as a TiAlN coating decreases the tool wear considerably for conventional machining. Furthermore, CBN and PCD tools (because more mechanical and chemical stability at high temperatures) presents a longer tool life in comparison to WC-tools during LAM.

2 Novel Laser Assisted Side Milling

2.1 Tool Concept

The relative movements between tool, work piece and laser beam makes the laser assisted milling more complicated than turning. The laser beam integrated machine-tool system as a solution is susceptible for industrial application. Here, after a brief description of the laser beam integrated machine tool system progress, the machine system used in this study (new successor of used machine by Rosen [53]) will be observed.

The presented laser tool machine system in this research was developed in framework of TooLAM project. The project is cooperation between Fraunhofer IPT (coordinator, open real time process control system, System performance testing and optimization), IWS Graz University of Technology (modeling of material behavior, process design and optimization), Sill Optics GmbH (development of active beam forming system), Rineck GmbH (scalable tool system design), Alfred Jaeger GmbH (spindle system with interfaces for mechanical coupling, optics and process gas), TECHSOFT GmbH (CAM system and NC-control software module), Huf Tools GmbH (Manufacturing of demonstrator geometries) and IPG Laser GmbH.

2.1.1 First Generation

The laser itinerary from a fixed laser source on the working plane can be stated that as a main challenge in manufacturing a laser integrated machine tool system. This route can reduce the required component parts, the complication and the production cost in industrial series of an integration of the laser beam with the machining tool. In this connection, the interaction between the optical and mechanical components should not be impacted negatively by the thermal load on the machine tool and machining process.

An aggregate conventional machine tool consists of a motor spindle and cutting tool which are joined together by a HSK (Hollow Shank Tooling) tool holder. The HSK-tooling provides highly accurate positioning due to face contact even at high speeds. The basic structure of the motor spindles is often the same and regardless of manufacturer comprises a rotor, stator, clamping device, rotary feed through and central coolant tube. High pressure coolant is transported over the feed through into the hollow spindle and from there into the cutting tool.

In the first efforts to develop a laser integrated spindle [63], the central coolant bore (without any new special spindle construction) was used for axial beam delivery. A fixed mounting of glass fiber for the delivery of laser beam into the tool end is difficult because of the relative movement between the machine frame and the rotating spindle. In Figure 2-1, three different design concepts for modular laser integrated spindle with axial beam delivery in a four axis milling machine tool MH600C from the MAHO Company are presented.

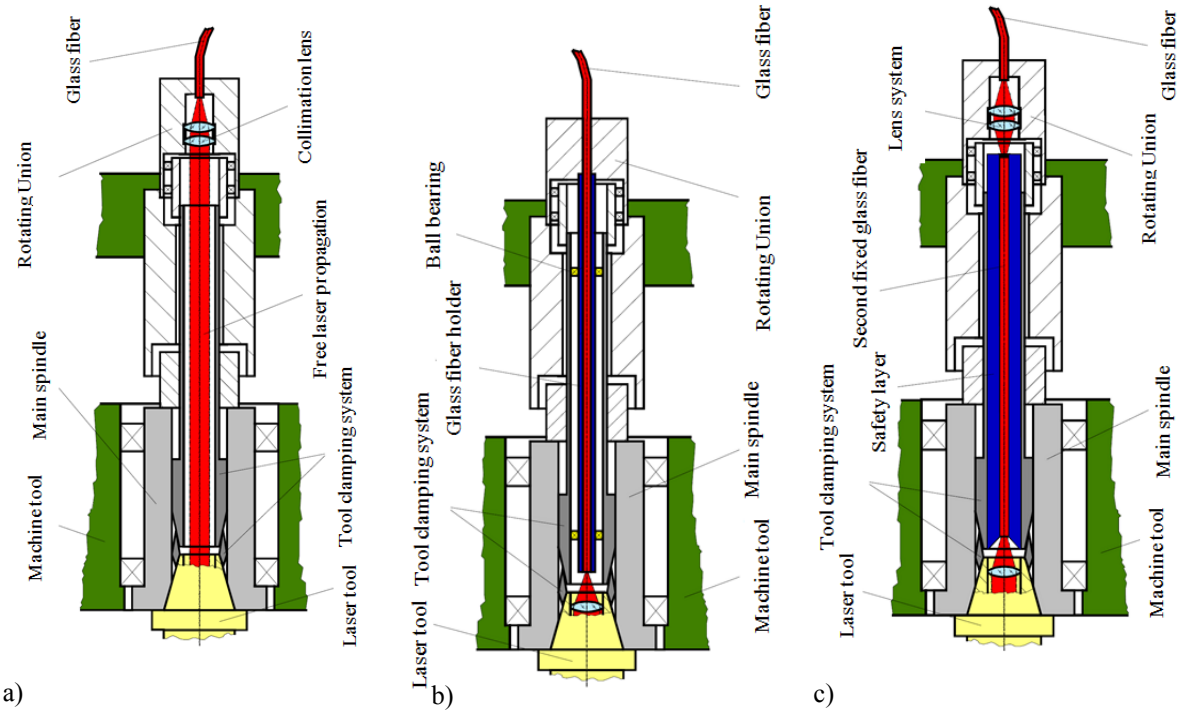

Figure 2-1: Axial spindle-integrated laser beam delivery concepts, (a) Free propagation ,(b) End fiber fixed and (c) Fiber-fiber coupled [63].

In the first concept, the laser beam delivery into the tool end is achieved by free propagation where the assembled optical lens in the rotary feed collimates the laser beam. The small central bore restricts the application of this concept. In the second one, the glass fiber is conducted through the spindle just before the cutting tool and the optical lens is assembled on top of the cutting tool. In the third design, which was used for further investigation by corresponding researchers, two glass fibers are used. The first glass fiber from the laser source is collimated in the rotary feed through and focuses into the second glass fiber. Next, collimation is carried out by the mounted optical lens on the top of cutting tool.

Some of advantages and disadvantages of the each modular laser integrated spindle can be found in Table 2-1. Despite the rotation of the mounted glass fiber with the spindle, a time-synchronized focusing on the cutting edge was not possible. Because of that, the research was bound only with blade-repair by the laser powder melting in defected areas.

Table 2-1: Comparison between three possibilities in laser guidance through spindle [63].

	Advantage	**Disadvantage**
Free propagation	• simple design • few optical lenses • high beam quality	• restriction by small central bore diameter
End fiber fixed	• no power loss • high beam quality	• complicated construction • no supply of process gas
Fiber-fiber coupled	• required low conducting space through spindle • supply of process gas	• complicated construction • requirement of additional optical systems

2.1.2 Second Generation

In the next steps, Rosen [53] realized a modular laser integrated machine tool and set it up for the side milling of diverse materials. In this machine tool system, the collimated laser beam is conducted into a cutting tool based on the free propagation inside the spindle. From the spindle, collimated laser beams have to find a seat on the cutting edge in front of the cutter. This key challenge blossoms the idea that the route of the beam can be deflected through mounting the reflective or transmissive optical components in a cutting tool.

Figure 2-2 illustrates the fundamental system design and the optical approach for the active laser beam guiding. As can be seen, the glass fiber from the laser source station is guided towards the hollow spindle shaft via an adjustable rotary feed through a union with an optical lens and a protective glass. The collimation components build a nearly parallel beam which propagates through the hollow rotor shaft. The process gas is passed into the spindle system to

ensure the stable beam propagation through the whole system. The rotary feed through system further provides the necessary gas flow for the cooling of thermally loaded optical and mechanical components. Furthermore, applying process gas improves the thermal process efficiency through the immediate removal of the achieved machining chip out of the beam path.

The modularly designed cutting tool consists of four units: HSK interface, optical module, housing module and cutter holder. The HSK 100-C tool holder is a mechanical interface which connects the spindle housing with the optical systems. Also, the process gas is regulated and distributed by passing through the tool holder. The optical system is the main special section of this tool which is made of a thermal neutral nickel iron alloy (Invar). This module consists of a focusing lens, a protecting glass and two mirrors (passive reflector). The mirrors deflect the incoming laser beam and conduct it on the cutting edge in front of cutter. The positions and angles of mirrors determine the distance between the laser spot and the cutter as well as the angle of incident. The mirrors are fixed on the brass and aluminum holders which absorb the scattered proportion of the beam.

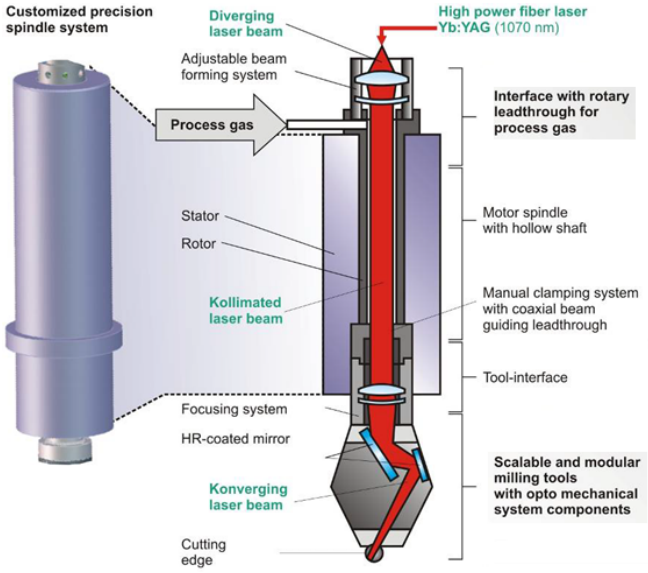

Figure 2-2: Modular laser assisted machine-tool system [51].

The rotatably mounted housing module captures and transports the dynamic process forces into the entire system. Also, the housing module supports the tool system balancing at high speeds (up to 10000 min^{-1}). The height-adjustable cutter holder is installed at the housing module which makes vertical and radial setting of the cutter position possible.

The advantages of a modular system design with optical and mechanical interfaces guarantee the scalability of all system modules, e.g. dimensions and aspect ratios of the milling tools. Additionally, modularity of the complete cutting tool system enables the essentially fast and

easy adjustment of laser beam parameters, as well as accessibility to all key mechanical and optical system components. One deficiency of this cutting tool can be seen in a multiple redirecting of the laser beam by the reflector mirrors, which decreases the beam quality. On the other hand, the scattered beams affect the thermal load and thermal efficiency of the process. Hence, a necessity of a special gas cooling system and optical system comes into consideration. Also, the small diameter of the entire cutting tool system (24 mm) does not support the precise position of the laser spot on the cutting edge as the cutting speeds increase. Another important point of view is that the high machining productivity still is not attainable.

2.2 Optical Design

This chapter provides an overview of the procedure for laser tracing techniques used in the design of some optical systems. The first one is the Ray transfer matrix analysis and its application to the Gaussian beams forming. Then, it is outlined that how to define the characteristic dimensions of machine tool system in order to attain the demanded laser parameters.

2.2.1 Optical Requirements and Influencing Factors

The Ray transfer matrix analysis [64] is a concept that traces a light beam during propagation through a rotationally symmetric optical system. The effect of an optical element on an input light beam with a transverse offset r_o and an offset angle θ_o from the optical axis using a 2 × 2 matrix can be calculated as follows:

$$\begin{bmatrix} r_{oB} \\ \theta_{oB} \end{bmatrix} = \begin{bmatrix} A_0 & B_o \\ C_o & D_o \end{bmatrix} \begin{bmatrix} r_{oF} \\ \theta_{oF} \end{bmatrix} \qquad \textbf{Equation 2-1}$$

This ABCD matrix is the multiplication product of the ABCD matrices of the each optical component in the system.

In practice, laser beams are used with a nearly Gaussian beam profile which behaves differently by passing through an optical component. Beam Quality Factor M^2 based on the divergence at beam waist radius (radius of beam at narrowest point) is a value to define beam focus ability. Measurements of laser beam quality on a variety of real laser beams is useful for predicting the effectiveness of laser beams for practical applications such as materials processing. The parameter M^2 describes how close a beam is to a perfect Gaussian beam where in this case $M^2 = 1$ and for a non-prefect Gaussian beam, $M^2 > 1$. Also, K as inverse of M^2 is called as beam quality number. This can be determined [53, 63]:

$$K = \frac{1}{M^2} = \frac{\lambda_o}{\pi}\frac{1}{w_0}\frac{2}{\Theta} = \frac{\lambda_o}{\pi}\frac{4}{d_0\Theta} = \frac{\lambda_o}{\pi}\frac{1}{BPP} \qquad \textbf{Equation 2-2}$$

where BPP stand for beam parameter product, $\Theta/2$ is at a half divergence angle and w_0 beam waist radius ($d_0/2$, as you can see in Figure 2-3), λ_o is the laser wave length.

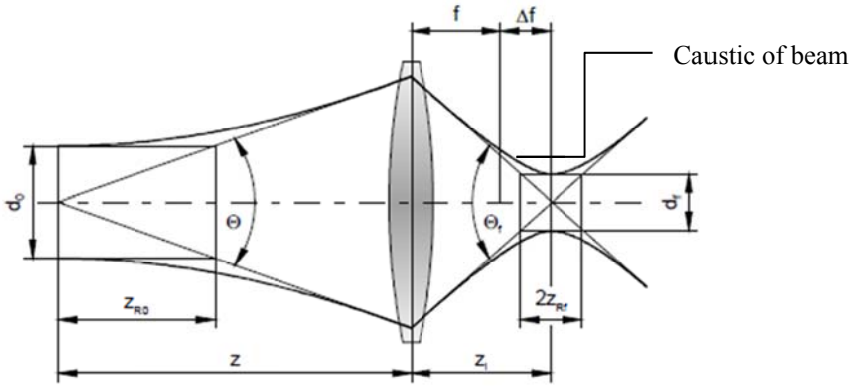

Figure 2-3: Focal diameter and Rayleigh length in a simple optical system [63].

The propagation of a laser beam (diameter of beam) in the area of waist beam increases with distance from optical components and beam wave length. Also, the according diameter decreases with the laser quality number. On the other hand, the focal radius ($w_{0,f} = d_f/2$) is also affected by the beam quality number and wave length, as can be estimated from:

$$w_{0,f} = \sqrt{\frac{\lambda_o}{\pi}\frac{Z_{R,f}}{K}} \qquad \textbf{Equation 2-3}$$

where Z_R stands for Rayleigh length which characterizes the distance from the beam waist as the beam cross section is doubled (or the beam diameter in order of $\sqrt{2}$).

The whole optical system arrangement in three variants with a defined distance between each optical component which is used in the present novel laser assisted milling is illustrated in Figure 2-4. The laser beam meets the collimation lens after passing a certain distance and then the laser propagates through the spindle with a diameter of 16 mm and passes the focus lens. In a distance of 9 mm of the focus lens, the prism changes the direction of the beam from the spindle rotation axis (or initial optical axis) on the final tool bottom. The prism is positioned with a distance of 96 mm vertically from the final tool bottom.

The position of the collimation lens has a significant effect on the propagation of the laser beam through the spindle hollow shaft and the focusing on the cutting edge. Based on the above mentioned approach (ABCD matrix), the resulting focal diameter is calculated. The results of position variations of the collimating lens in the real machine tool system are presented in Figure 2-4. As can be observed, when the collimating lens is placed at its

maximum position (43.38 mm), the generated beam is nearly parallel and the laser beam is focused on the working plane with a diameter of approximately 0.6 mm (each check box is 0.1 mm) in comparison to 1.2 for the minimum position of collimating lens (40.38 mm). Furthermore, with the decreasing the position of the collimating lens, the radial position of the laser spot from the central axis from 15.3 mm to 15.82 mm increases.

Besides the analytical results, the measurement of laser caustic was performed by Mode Scan instrument in IPT Fraunhofer (Figure 2-5) to determine the six beam propagation parameters (caustic of laser beam) easily and reliably for any real beam. Furthermore, it is possible to measure the laser spot size and its variation with the collimating lens position at the working plane. Also, with the measuring of the laser power before that of the collimating lens and at the working plane, the laser power efficiency (or laser power loss) is recognizable. In Figure 2-6 it can be observed that the beam is not exactly circular and a symmetric elliptical distribution is visible. The laser spot radius (with the measurement of M^2: 18.7, beam quality number: 0.053, divergence angle: 50.568 mrad, Rayleigh length: 9.867) on the working plane is about 0.5 mm, which is in range of a calculation with I=43.38 mm.

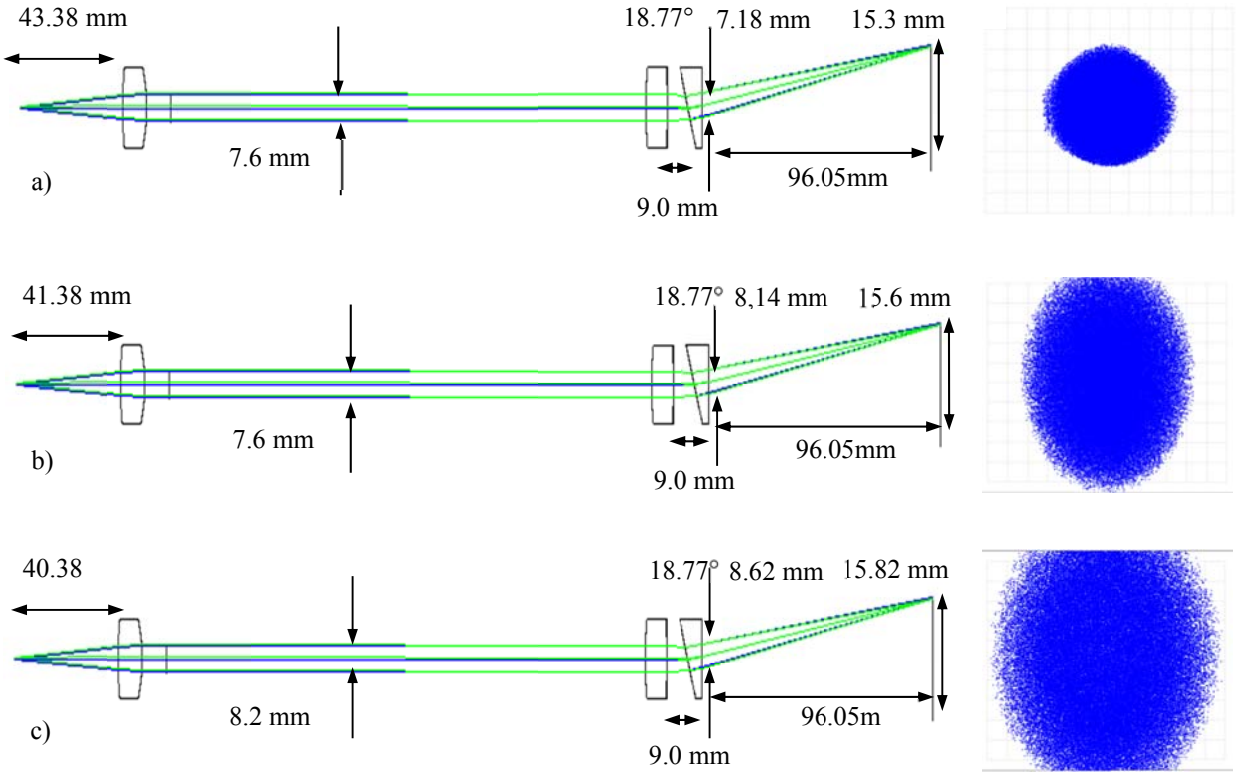

Figure 2-4: Effect of optical element arrangement on the size and geometry of the laser spot based on the geometric image analysis, (a) I= 43.38 mm, (b) I=41.38 mm and (c) I= 40.38 mm [65].

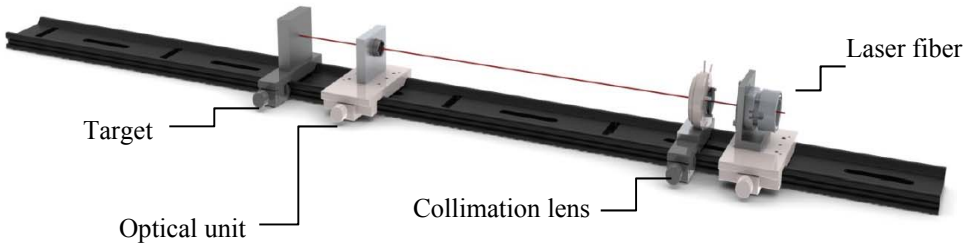

Figure 2-5: Experimental setup for the measurement of laser beam caustic [66].

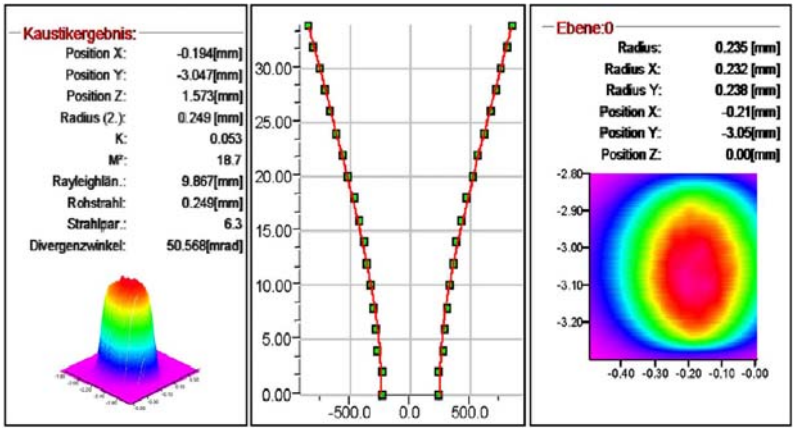

Figure 2-6: Result of caustic of laser beam on the working plane [66].

Figure 2-7 shows two tracks of laser beams on the black checkered paper (each check box is 1 mm) in a distance of approximately 14 mm (set point is 15 mm) from each other. The right one presents the track of collimated laser beam before the focus unit while the left one shows the track of focused beam after passing and deflecting of the focus unit. The depicted results demonstrate the effect of a variation in the position of the collimating lens on the position and size of the resulting laser spot size on the eventual working plane. These results also confirm that an optimal distance from the lens outside to the fiber end is 43.3 mm.

In order to locate a laser beam at a working plane (i.e. cutting edge), the series of optical components with respect to type, material and geometry should be arranged precisely. Apart from these, for the goal of designing an effective laser system with low laser power loss and high laser quality at the working plane, the distance between each optical component as well as the thickness of the same element is very important. In this research project, a new optical system was designed and integrated in the cutting tool holder to improve the beam quality at cutting edge. The optical system consists of two separate units: collimation and focus unit.

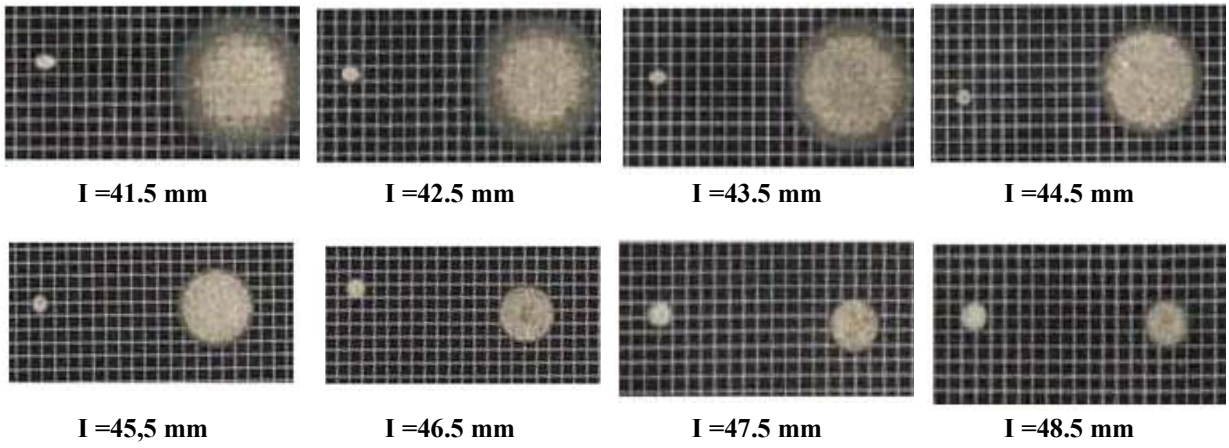

Figure 2-7: Variation of laser spot size before (right ones) and after passing optical unit (left ones) with the collimation lens position [66].

2.2.2 Collimation Unit

The divergence beam from the laser source via glass fibers is propagated coaxial to the rotation axis of the spindle shaft. In addition, the collimation unit adjusts the precision of overlapping of the optical axis on the rotation axis. The details of the applied collimation unit at the present laser assisted machine system are illustrated in Figure 2-8. The optical fiber coupler connects the optical fiber with the unit case. The mechanical adjust unit fixes the collimation unit or rather fiber glass in the direction of X and Y. The water coolant system protects the fixed collimation lens from overheating. Because of the small number of surfaces, the only spherical lens used is made of quartz (diameter: 50 mm, edge thickness: 0.8 mm, middle thickness: 9 mm) with the focal length of 60 mm and decreases the aberration which causes the power loss [53] .Via a timing belt drive it is possible to set the suitable caustic of the laser beam to improve the laser beam quality on the working plane. The complete collimation unit is mounted on the spindle over the rotary feed through which the supplied air pressure protects the unit from penetration of liquids and particles. For the optical coupling is important that the interface between the rotating and fixed fiber glass is located at the collimated beam path.

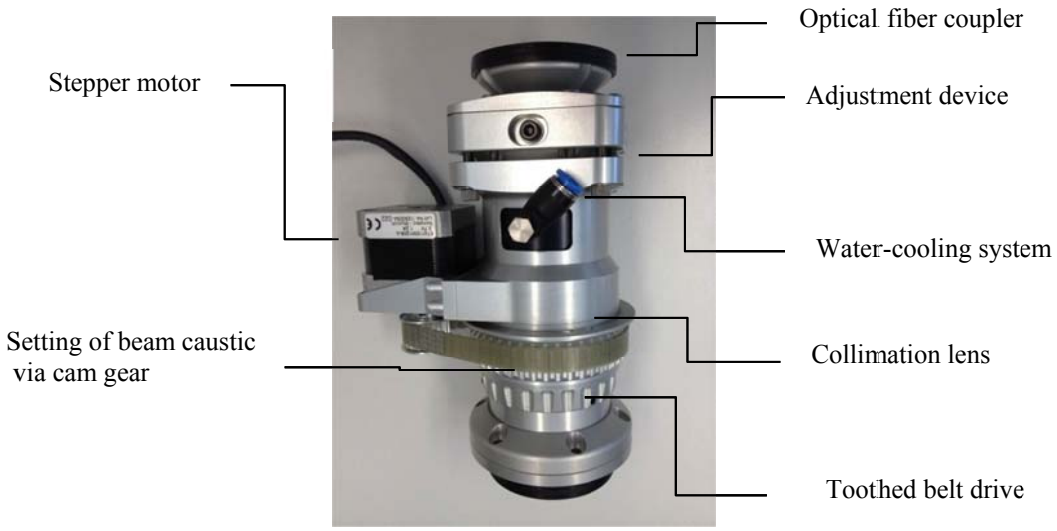

Figure 2-8: (a) Collimation unit and (b) geometry of applied collimation lens [67].

2.2.3 Focus Unit

In the focus unit, a nearly parallel incoming beam through the hollow shaft is first converted to a converging beam and then is deflected and focused on the cutting edge. The focus system consists of a focus lens (S1LDX5151/126) with the focal length of 120 mm (diameter: 33 mm, edge thickness: 0.8 mm, middle thickness: 10 mm) and a prism from optical glass with the inclination angle of 18.77 ° (diameter: 20 mm). The lens and prism are combined within one assembly unit which is accurately mounted inside the milling tool using a cylindrical pin.

2.3 Spindle-Tool Design

The reliable use of the innovative laser assisted machining process requires appropriate spindle-tool concepts that at high speeds ensure the position accuracy of the laser beam. There are several factors which decrease the process precision, along with expected benefits of laser assisted milling such as an increasing tool life. In broad terms, the requirements comprise high machine and tool rigidity and respectively dynamic (tool vibration) and thermal stability. The key components which need special attentions are the bore diameter (rotator design), the height of spindle or rather the distance which the laser beams have to propagate through it (consequently spindle mass balance), holders which fix optical elements, the planned bores for the cooling system (process gas) and finally the mechanical interfaces which support the modular construction concept. With increasing the spindle diameter, in addition to general problems in the spindle, the dynamic clamping on the interface between the cutting tool and spindle system is critical.

The relevant components of the applied spindle-tool system in the present work are shown in Figure 2-9. The height of the entire spindle-tool system is 885 mm while the maximum diameter is 210 mm. The spindle consists of three main parts: rotor, stator, and spindle

reception .Via the rotary feed at the end of the spindle (after the collimating unit), the process gas and compressed air is supplied first into the center of the main spindle. The process gas is passed centrally into the tool and radially outward just before the end of the spindle and is transferred into the top of the cutting tool. The internal process gas can afford pressure of up to 40 bar. However, the process gas flow rate should not interrupt the whole process significantly.

In this work, the cutting tool is joined to the spindle using a HSK 63 interface, which is smaller than the previous model (HSK 100). Here, as can be seen in Figure 2-9, the cutting tool consists of four modules: tool housing, focus unit, tungsten carbide core and cutting insert holder. Because of the symmetrical design and consequently a mass balance, two diagonal inner bore are prepared, where from one of them, the laser beam is guided on the cutting edge. A tungsten carbide core is provided for fixing the cutting insert holder with the main cutting tool housing. The path of laser beam as well as the process gas flow is shown in Figure 2-10.a.

The main tool housing involves a hole space with a stepped design (nut) where the optical module inside can be assembled. A ring-shaped holder fixes the optical model using a cylindrical pin from one side and on the other side it is fixed by a conical seat. The sum of the maximum deviation in position of the laser spot at the working plane (nominal value is 15.3 mm) based on production tolerance and position deviation is 0.29 mm. Table 2-2 shows the effect of each component on the resulting deviation of laser spot on the cutting edge.

Table 2-2: Results of deviation of laser spot position [66].

	Deviation/Tolerance	**Position deviation of laser spot [mm]**
nut	+/- 0.05°	0.013
fitting key joint	4 H7/g6	0.014
ring shaped holder	+/- 0.05°	0.013
cylindrical pin	2 H7/h8	0.015
orientation surfaces at lens	+/- 0.05°	0.013
orientation surfaces at prism	+/-0.02 mm	0.014
tool holder axis to optical axis	+/- 0.05°	0.08
sum		0.29

The cutting insert holder (Figure 2-10.b) with the diameter 33.9 mm also includes toothing with scaling to adjust the radial and circumferential position of the laser spot. The cutting holder is able to carry two inserts in different manners (the screw fixing for metal based insert or sticking for ceramic one).

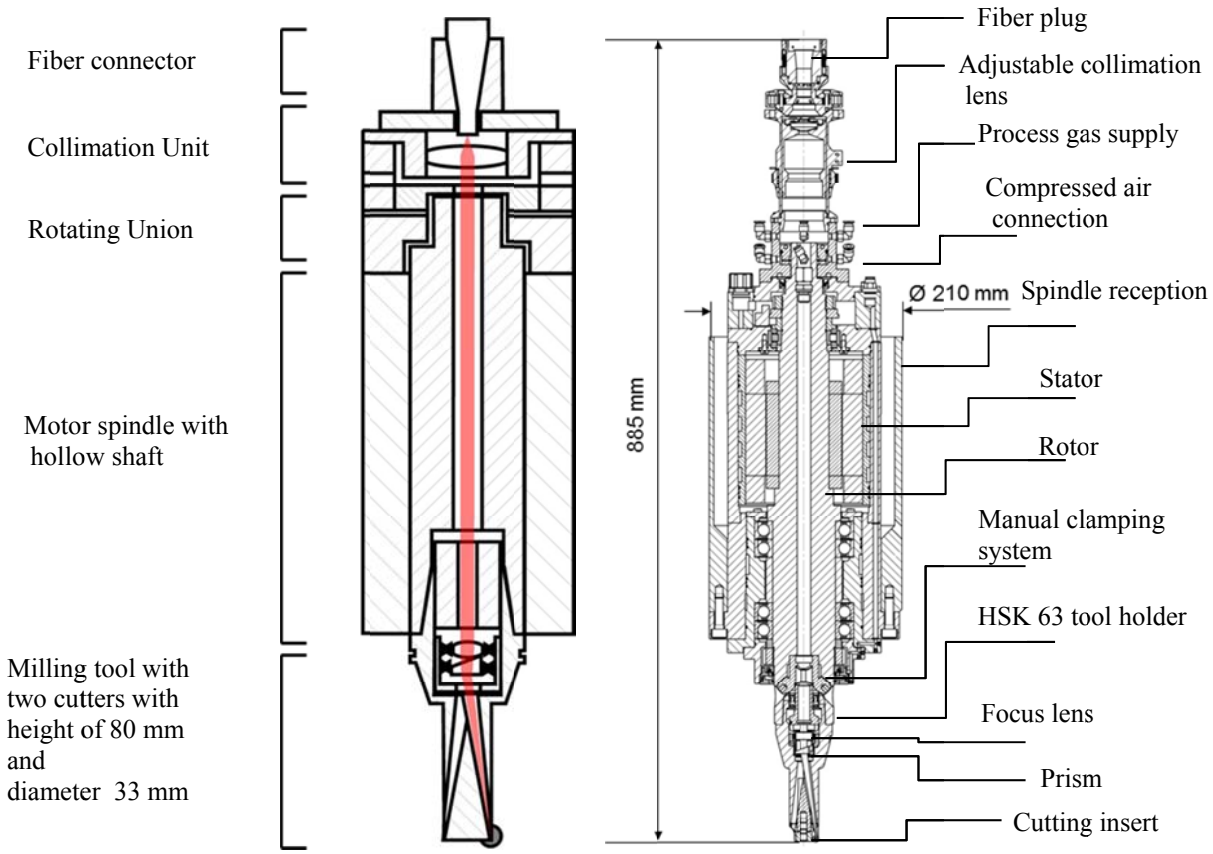

Figure 2-9: Laser integrated tool-spindle system [67].

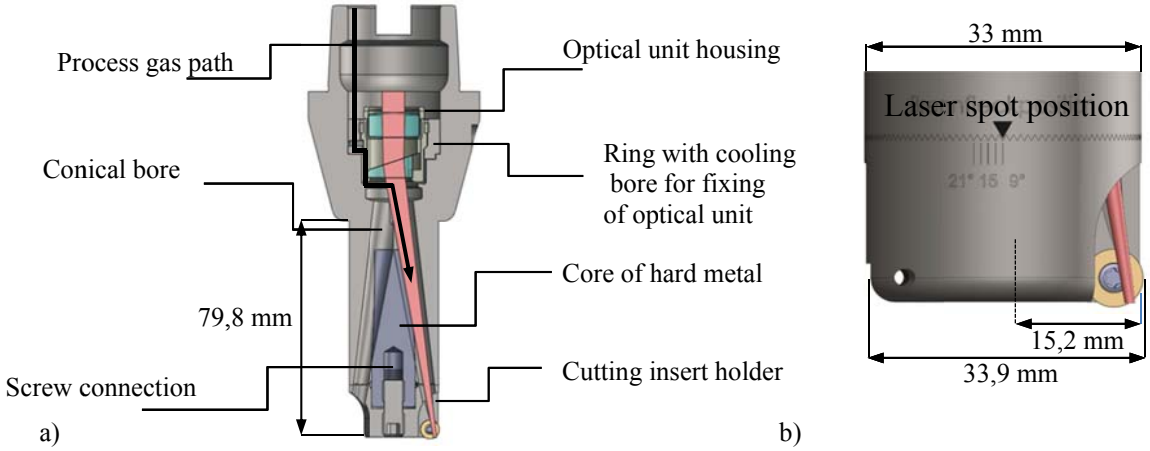

Figure 2-10: (a) Milling tool with integrated laser beam delivery and (b) cutting insert holder [67].

2.4 Control of Process

In the broad term, the main goal of process control in the according laser assisted milling is to synchronize the switch off/on laser on the tool entrance/exit on the tooth trajectories during milling. Figure 2-11 shows the control system route which was implemented in the LabVIEW

software. After calculating the current angle of the spindle and the rotational speed (RPM) of the spindle, four analog signals minimum and maximum chip thickness as well as a tool entrance and exit angle are used to apply laser power control. This information is transformed from the NC machine through the analog module installed on the CompactRIO. The following sections focus on the determination of these four parameters which later will be used also for 3D process simulation.

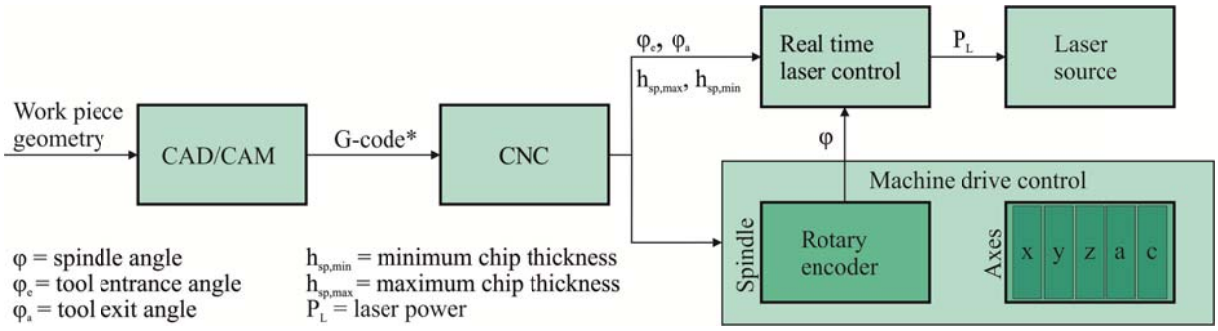

Figure 2-11: Process control map [67].

2.4.1 Determination of Entrance and Exit Angle

In the milling process, the cutting insert rotates about one common vertical axis (cylindrical spindle) and moves in the feed direction. Referring to the relation between the rotational direction and feed direction, the milling process is divided into up milling and down milling. Down milling is generally understood as the milling cutter moving in the direction of its rotation. With regard to synchronization motion, down (climb) milling in comparison to up milling has some advantages, such that the chip thickness decreases with the chip generation progress. With consideration of the 2D milling plan, the feed and the cutting velocity can be calculated by below relations:

$$v_f = f_z . z . \vec{n} \qquad \textbf{Equation 2-4}$$

$$v_c = \vec{n} . \pi . d_f \qquad \textbf{Equation 2-5}$$

where v_f is the feed velocity [mm/s], v_c is the cutting velocity [m/min], f_z is the feed per revolution [mm], z is the number of teeth, $\vec{n}$ is the rotation velocity [min^{-1}] and d_f is mill diameter [mm].

As can be seen from Figure 2-12, the spindle coordination system moves in the direction of feed, thus, the engagement angle or bias angle which is attributed as the difference between entrance and exit angle of cutter with respect to the origin of the cutting mill is:

$$\varphi_c = \varphi_a - \varphi_e = \arccos\left(1 - \frac{2a_e}{d_f}\right) \qquad \textbf{Equation 2-6}$$

where φ_c is the engagement angle, φ_a is the exit angle, φ_e is the entrance angle, a_e is the width of cut and d_f is the tool diameter. The continuously exact determination of the entrance and exit angle has a particular meaning for adjusting of the laser power with the uncut chip thickness. In the 2D- milling plane, to simplify the modeling procedure, a great flexibility is offered for the calculation of the relevant required angles with componential displacements in X and Y direction with defining φ_f as the feed angle (actually, the feed angle is incrementally a description of the engagement angle).

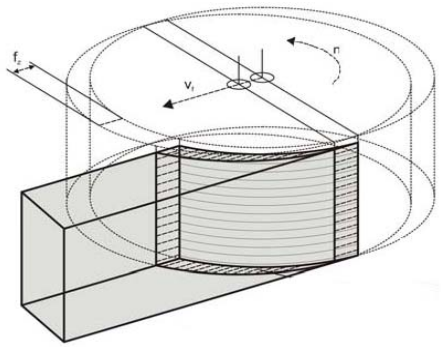

Figure 2-12: Direction of rotational and deed velocity in down (climb) milling [68].

In the machining of the industrial and complex components, the 2D machining with only one directional milling path is not satisfied [69]. Hence, it is essential to expand the model for 3D milling level by defining a fixed reference coordination system on the work piece. Using a transformation matrix, the displacements from the spindle coordination to the work piece coordination are transformed. The multiplicand transformation matrix consists of a displacement matrix (for origin transformation) and three rotation matrixes round the X, Y and Z axis.

The main aspect that differentiates 2D milling from 3D milling is the width of cut which changes at the beginning and finish of paths as well as the direction changes (curved path). For this purpose, the cutting length (l_a) according to the work piece coordination system is defined as the cutting progress respectively the work piece length (l_w), which can be determined from:

$$l_a = \sqrt{a_e d_f - a_e^2} \qquad \textbf{Equation 2-7}$$

Figure 2-13 shows the variation of the cutting width and consequently the resulting feed angle (from the incremental form of Equation 2-6) at the tool entrance, full engagement and tool

exit. The comparison between the cutting length and related displacement in the work piece coordination defines the milling phase. The entrance and exit angle at the beginning and end of the path presents a same value. Then, the exit angle increases and reaches a constant angle while the entrance angle is constant till the tool exit phase. It increases after that.

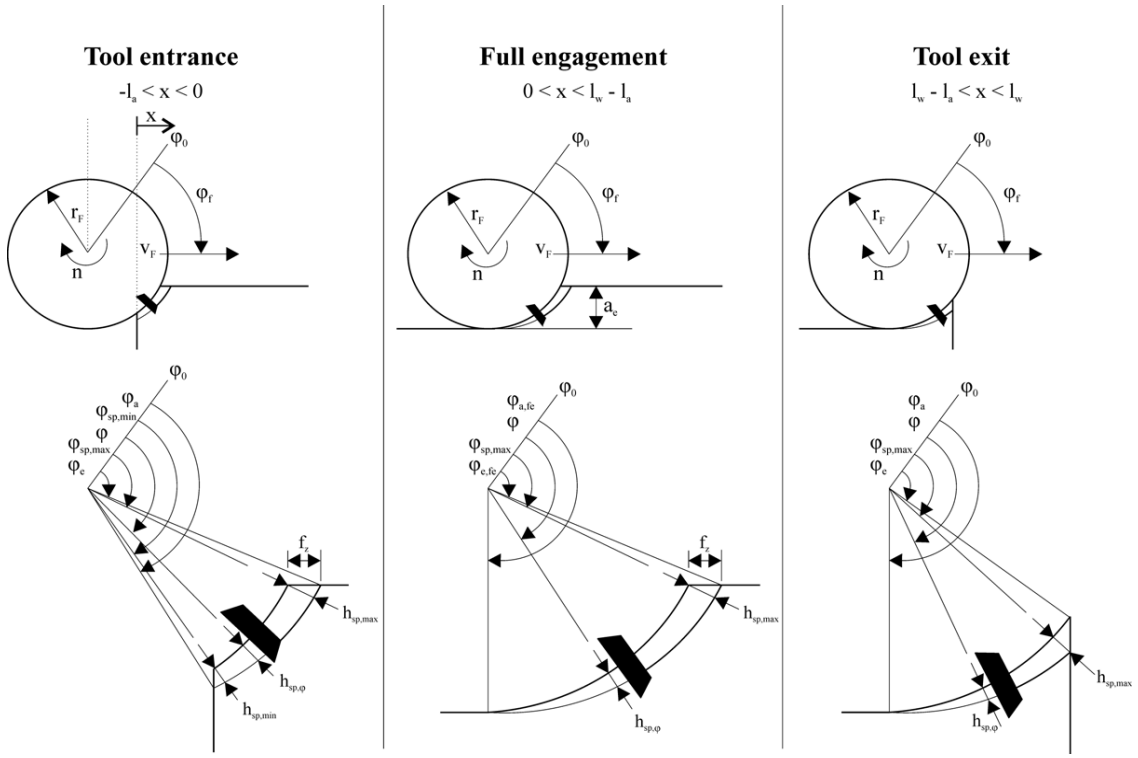

Figure 2-13: Three tool engagement conditions in down (climb) milling [70].

2.4.2 Determination of Uncut Chip Thickness

Along with a determination of the entrance and exit angle in the side milling process, the important concern in control of laser assisted milling is to find out the instantaneous uncut chip thickness during the milling process. Figure 2-14 gives a geometrical schematic of the milling process regarding variation of the uncut chip thickness during the insert rotation. Actually, in the down milling manner, as mentioned above, the uncut chip thickness decreases with the insert rotation. With the neglecting chip thickness at zone I and an assumption which states that the path of insert rotation is circular (in comparison to the trochoid), Martellotti [56] developed a model to calculate the instantaneous uncut chip thickness for one insert:

$$h_{SP,II}(\varphi) = r_F + f_Z \sin\varphi - \sqrt{r_F^2 - (f_z \cos\varphi)^2} \qquad \textbf{Equation 2-8}$$

where h_{SP} is the instantaneous uncut chip thickness at zone II, r_F is the mill radius, f_Z is the feed per insert and φ is the angular position of the cutting point in the working plane.

Additionally, another potential is to simplify the Martellotti model with the assumption that the feed per insert is much smaller than the cutter radius, thus Equation 2-8 can be reduced to:

$$h_{SP;II}(\varphi) = f_Z \sin\varphi \qquad \textbf{Equation 2-9}$$

To calculate the cross section of the uncut chip thickness (A_{SP}), as can be seen in Figure 2-14, with choosing an infinitesimal length it can be assumed that the upper and bottom uncut chip thickness is equal and:

$$A_{SP;II}(\varphi) = a_p h_{SP}(\varphi) \qquad \textbf{Equation 2-10}$$

where a_p is the depth of cut.

Also, for an infinitesimal angular position of the insert it is valid:

$$dl = r_F d\varphi \qquad \textbf{Equation 2-11}$$

The instantaneous volume of uncut chip at zone II ($V_{SP,II}$) can be found from below integration:

$$V_{SP;II,i} = \int_{\varphi_i}^{\varphi_{i+1}} A_{SP,i}(\varphi)\, d\varphi \qquad \textbf{Equation 2-12}$$

Figure 2-15 shows the achieved results for a mill diameter of 34 mm, feed rate of 0.07 mm per revolution and width of cut of 8 mm. It should be mentioned the for the small feed rates,

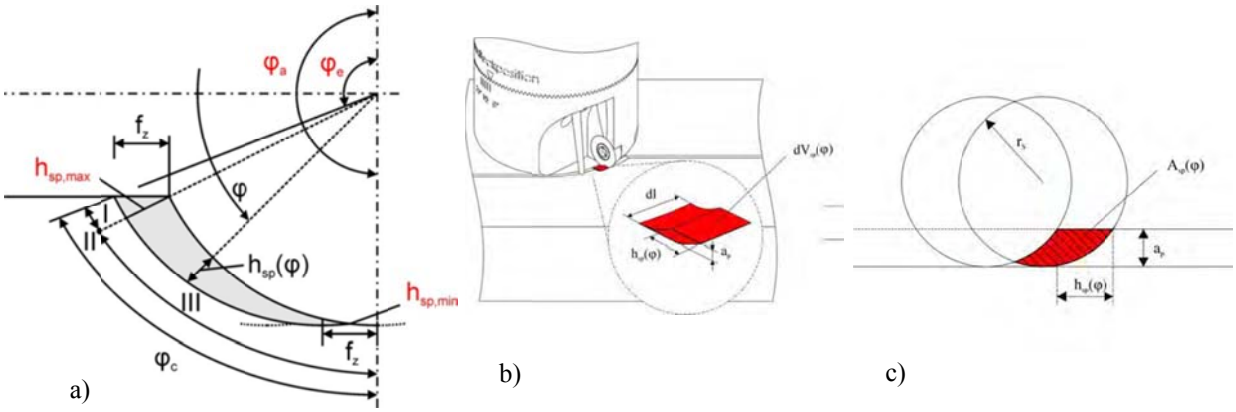

Figure 2-14: (a) Top view of chip thickness course during a full revolution (b) elemental chip volume (c) chip area in relation to radius of cutting insert [53, 70].

the instantaneous volume of uncut chip in area I is less than the maximum volume in area II and does not have a remarkable effect on the laser adjustment.

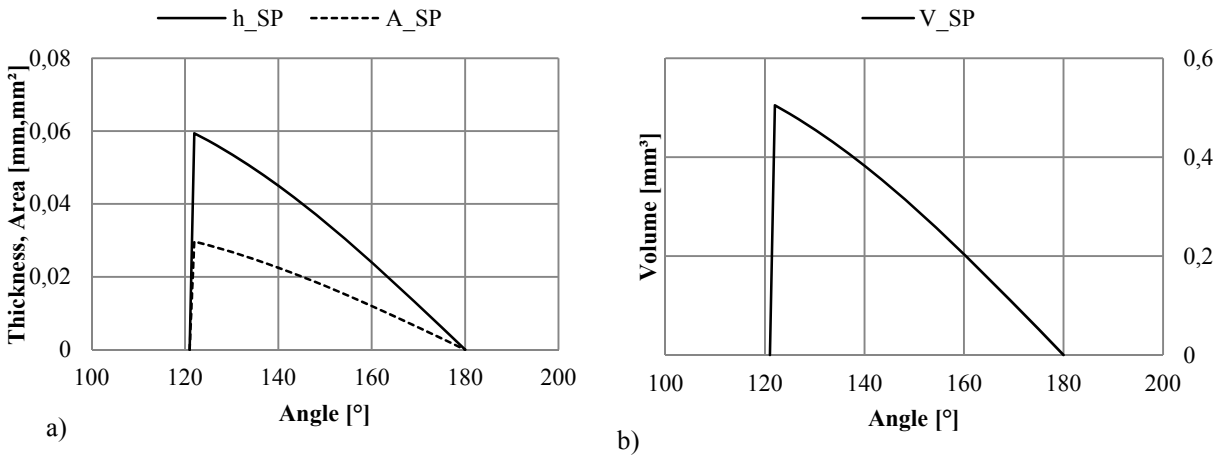

Figure 2-15: (a) Variation of chip thickness, chip surface and (b) volume with engagement angle.

In the next step, the laser power (P_L) should be adjusted with the uncut chip thickness with the time during one rotation of the insert:

$$P_L(t) \propto \dot{V}_{SP}(t) \qquad \textbf{Equation 2-13}$$

where $\dot{V}_{SP}(t)$ is the uncut chip volume rate.

For more convenience for controlling the laser power in the process, the laser power profile with time is linearized with respect to the entrance and exit angle. Furthermore, because of process related conditions, the laser power does not go to zero at the exit angle and with defining a minimum value. It means that the slop of laser power line in Figure 2-15.b is slighter in comparison to the chip volume. Only after that, for angles greater than the exit angle the laser power turns off.

2.5 Experimental System

Laser-assisted milling experiments with an integrated laser–tool system (Figure 2-16.a) were carried out on a Satisloh G1 3+2 axis machining center with Bosch Rexroth MTX P60 NC control. An IPG YLR high fiber laser (Yb: YAG with a wavelength of 1070 nm) with a peak power output of 6 KW via a light conducting cable was applied to the laser radiation. The machining mode was set up for the side milling and the depth of cut was of 0.5 and 1 mm for Ti-6Al-4V. All the experiments were performed with round inserts (RDHX 07 07 MOT with D=7, D1= 2.7, S= 2.38 mm and the rake angle 11°) using TiAlN-coated cemented carbide (Figure 2-16.b). The process gas was delivered in the machine spindle system with 35 liters per minute. The dimensions of the work piece are 81 mm x 81 mm which provides the milling of 10 paths. As the first step for each milling surface, the edge of the work piece with respect to the planed depth of cut was chamfered (Figure 2-16.d and .e). The chamfering prevents the different cutting insert engagement conditions between the first contacts and the next [70].

The first sharp edge of the work piece conducts a notch in the cutting insert and also a variation in the laser absorption which makes the chamfering necessary. The work piece was clamped with a Kistler piezo-based three dimensional force measurement which determined the process forces in 3 directions (the coordinate system is shown in Figure 2-16.c; the feed direction is along the X axis) during the machining experiments.

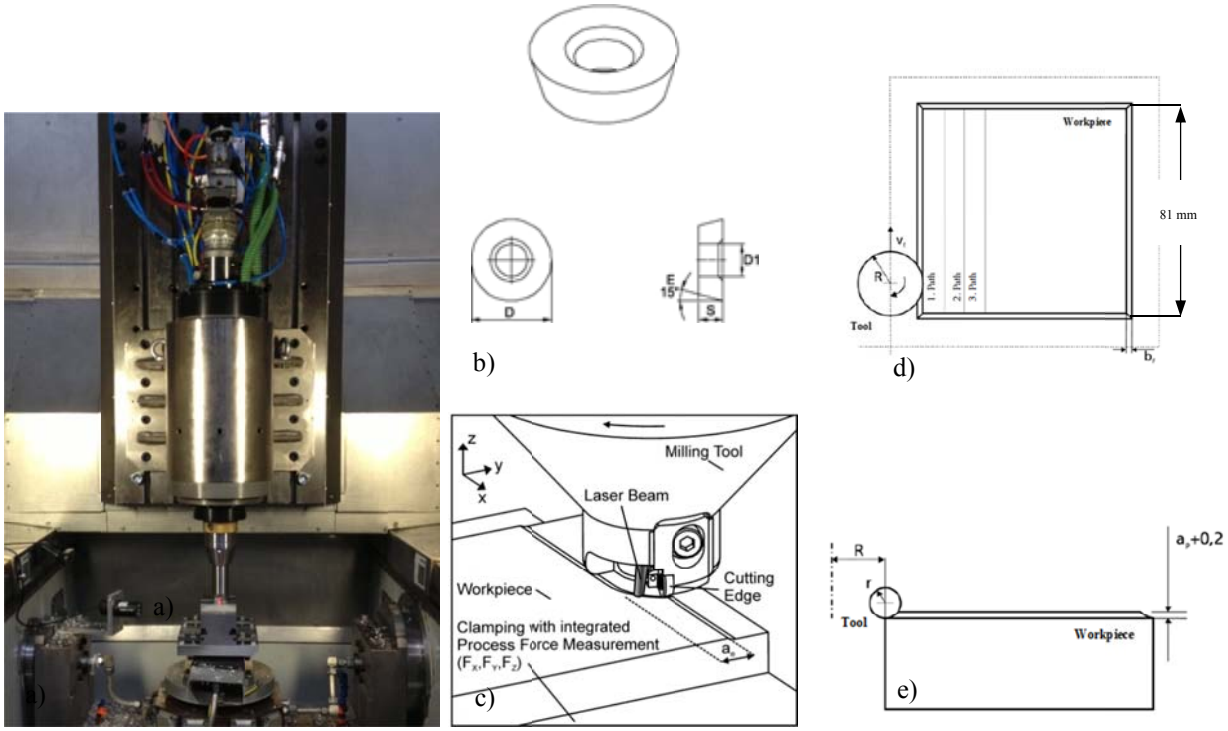

Figure 2-16: Experimental setup (a) aggregate laser assisted side milling-TooLAM, (b) cutting insert geometry, (c) x, y, z coordination, (d) work piece geometry and milling paths and (e) side view [51, 67, 70].

Each electric charge produced by the dynamometer was converted to voltage signals by a charge amplifier. For one path of the milling, the maximum forces in each revolution (with the frequency of 200 up to 450 kHz) were averaged. The forces were saved automatically with a program based on NI LabVIEW.

2.6 Experiment Result

Before discussing and interpreting the achieved results in this section, the method of evaluation of viewed forces (NI LabVIEW) is stated. Generally, the milling process is not a quiet process. The permanent engagement and releasing of the cutter with tool, tool machine vibration, work piece repositioning and unexpected cutter breakage follows the fluctuation of cutting forces. In the according laser assisted milling, each vibration in the tool leads to a shifting of the laser spot and consequently in the force reduction. In order to find a value as

reference cutting force in this study, an average among the maximum forces is defined (Figure 2-17) as it was introduced and performed in Fraunhofer IPT by Hermani.

In the first step, bottom (t_b) and upper (t_u) time domains were defined. These domains are based on the geometry of work piece, tool and cutting velocity where they can be identified from:

$$t_b = \frac{X_b}{v_f}.60 \qquad \textbf{Equation 2-14}$$

$$t_u = \frac{X_u}{v_f}.60 \qquad \textbf{Equation 2-15}$$

where X_b and X_u can be found in the length of work piece (l_w), tool diameter (d_f) :

$$X_b = d_f + 1 \qquad \textbf{Equation 2-16}$$

$$X_u = l_w - d_f + 1 \qquad \textbf{Equation 2-17}$$

Afterwards, the number of rotations at the measurement range ($A_x = 5$) is defined and then the number of local maxima is found by:

$$i = (t_u - t_b)\frac{\vec{n}}{60.A_x} \qquad \textbf{Equation 2-18}$$

Then, the average of the maximum forces (F_{max}) can be calculated as a value for the analysis of cutting process and next for the validation of simulations:

$$F_{max} = \frac{\sum F_{max,i}}{i} \qquad \textbf{Equation 2-19}$$

where $F_{max,i}$ is the local maximum cutting force.

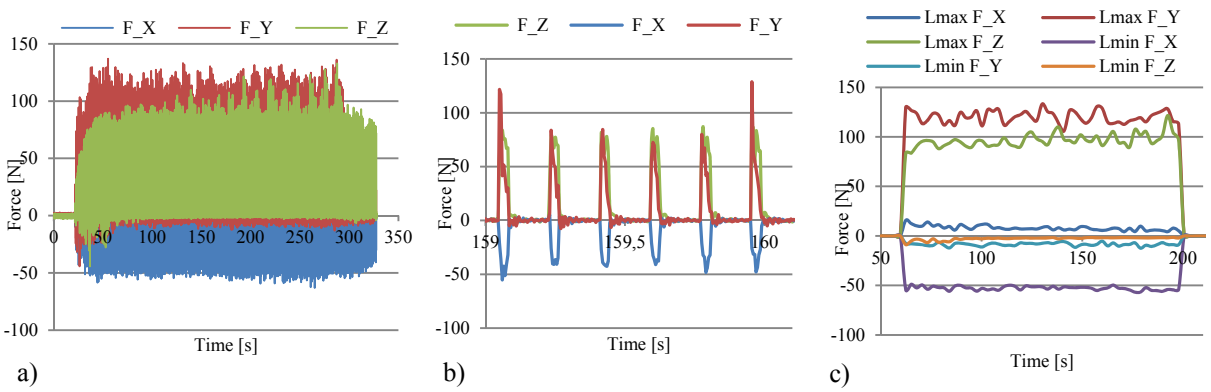

Figure 2-17: (a) achieved process forces from the Kistler force measurement device, (b) force in a time domain, (c) local maximum and minimum cutting forces [70].

2.6.1 Effect of Laser Power and Cutting Velocity on the Force Reduction

A first view on the result of experimental trials shows generally a reduction in three components of forces in all cutting conditions for all applied laser powers as illustrated in Figure 2-18. The left column diagrams (Figure 2-18.a, .b and .c) present the main cutting force (F_Y) for three cutting velocities (25, 50, 100 m/min) and three feed rates (50, 70, 90 µm/rev) for diverse laser powers up to 1758 W. The right column diagrams (Figure 2-18.d, .e and .f) shows the forces in feed direction (F_X) and normal to working plane (F_Z) with changing the laser power up to 1428 W in the same three velocities and feed rates.

As the laser power is turned off (Laser power=0 W), in connection with the common machining of Ti-6Al-4V alloy, the cutting forces increase with the feed rate and decrease slightly with the cutting velocity. As the laser power is on, the main cutting force in the Y direction decreases gradually with laser input down to a power of approximately 600-800W. The largest reduction between the conventional and LAM can be observed for a cutting velocity 25 of m/min and a feed rate 90 of µm/rev, although variations get small at laser powers higher than 1250 W. But this laser power leads to less force reduction at the velocity of 100 m/min. With an increase of the cutting velocity, the higher laser powers (1750 W) are more meaningful. Obviously, this could be attributed to the fact that for higher cutting velocities the material has less time to be heated. Here in this process, the heat dissipation is not relevant for all cutting velocity because of high rotation velocity. With increasing feed rate, the forces increase but the absolute amount of reduction in forces changes only slightly. The higher laser powers bring more force reduction for a feed rate of 90 µm/rev at three cutting speeds.

The experimental results show the reduction of main cutting force (F_Y) more regularly than the force in a direction normal to the milling surface (F_Z). The vertical force component (F_Z) generally decreases at low laser power (lower than 1250 W). Between 1428-1758W, the force reduction is not clear due to a number of uncertain aspects in the experiment. The best results were achieved for laser power 1071 W for all three feed rates and cutting speeds.

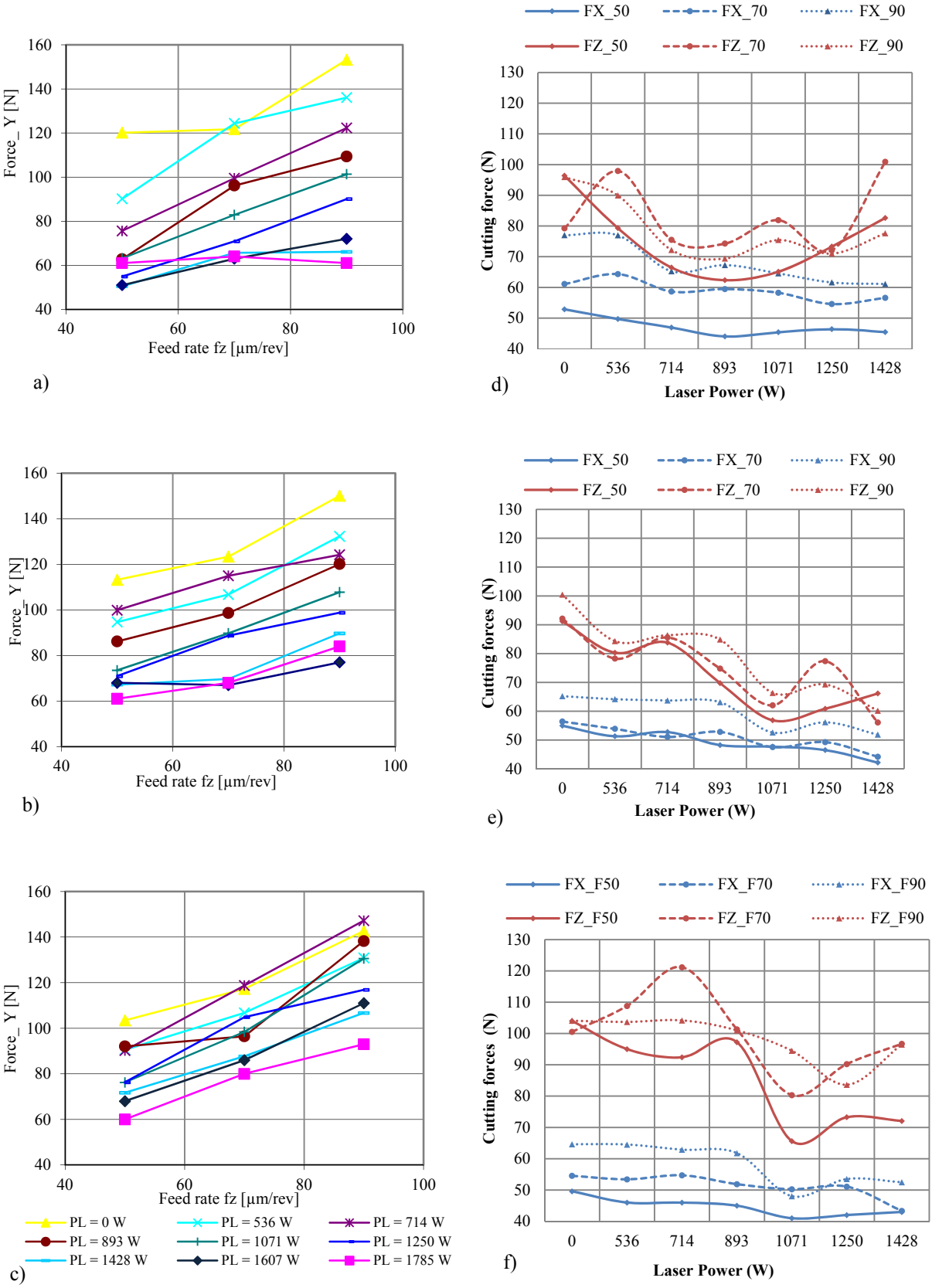

Figure 2-18: The variation of the main cutting force F_Y with the laser power, (a) cutting velocity of 25 m/min, (b) 50 m/min and (c) 100 m/min and the variation of F_X and F_Z with the laser power, (e) cutting velocity of 25 m/min, (e) 50 m/min and (f) 100 m/min [71, 72].

The results can be explained by adhesive bonding of the chip on the tool tip as the laser power increases especially at low speed machining and low feed rate. This phenomenon increases the contact area and stress state in the vertical direction leading to unexpected results.

The influence of laser power on the forces in the feed direction is not significant. These forces (F_X) are more sensitive to the feed rate. Still, these feed forces reduce by up to 30 % at the laser power 1428W and for three cutting velocities.

Another parameter in the machining condition which indirectly improves the LAM results is cutting depth. Using the higher cutting depth support, the application of higher laser power has meaningful influence to manage the laser spot position and consequently the absorbed heat input even with the machining tool vibrations. With increasing the cutting depth, the laser spot located deeper prevents the deflection of laser beams as the beam encounters the sharp upper chamber edge. Furthermore, with increasing the depth of cut, the uncut chip thickness decreases which supports thermal softening. A deflection of the laser beam on the un-machined surface has an inverse effect in terms of surface hardening. These unwanted results happened more at higher laser powers, where the surface temperature can easily exceed the martensitic transformation temperature.

Moreover, in case of other laser parameters, increasing the laser advance more than 5 mm shows a negative effect on the amount of reduction. The effect of laser advance, position and size of laser spot has been studied also based on the numerical investigation.

2.6.2 Effects of Tool Wear on the Force Reduction

Figure 2-19.a and Figure 2-20.a show the resulting forces based on the material removal volume for the side milling process with /without laser (cutting velocity: 57 m/min, feed rate: 80 μm/rev, laser power: 900 W with the TiAlN-coated cemented carbide insert). It can be seen that the forces (main influence is on F_Y and F_Z) increase with time in both processes, but the slope of force increase is lower in the case of laser assisted milling. The forces in Y direction increase by 19 % more rapid than conventional milling while this value improves to 32 % for the Z direction using a moderate laser power. The result can be explained with the change of the tool tip shape and tool (cutting insert) wear [73]. In other words, the slope of forces with time indirectly states the progression of tool wear for both processes. Figure 2-19.b and Figure 2-20.b illustrate the final tool tip geometry after the milling processes, which confirm a reduction of tool wear in case of milling with laser. In the case of machining without laser, a kind of damage localization (which is called notch wear) can be observed alongside flank wear. The wear mechanism in LAM can be summarized only in flank wear. The notch wear has a very bad effect on the finished surface roughness.

In our study in terms of the introduced analysis (progression of cutting forces with time), using the polycrystalline diamond (PCD) insert had the best result, then also TiAlN-coated

cemented carbide insert showed a good result. The result of cubic boron nitride cutting insert (CBN) was not satisfying.

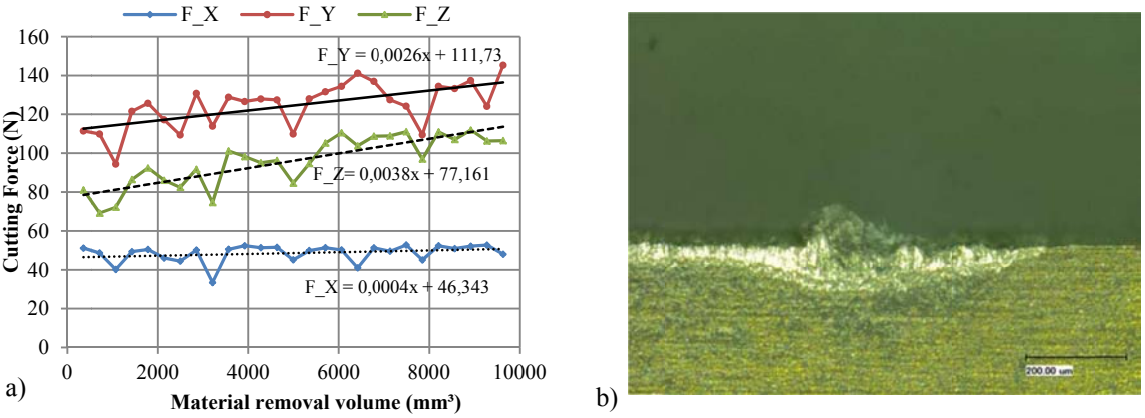

Figure 2-19: The effect of milling time on the process forces without laser (b) flank wear and notch wear appearance at the end of the milling process [74].

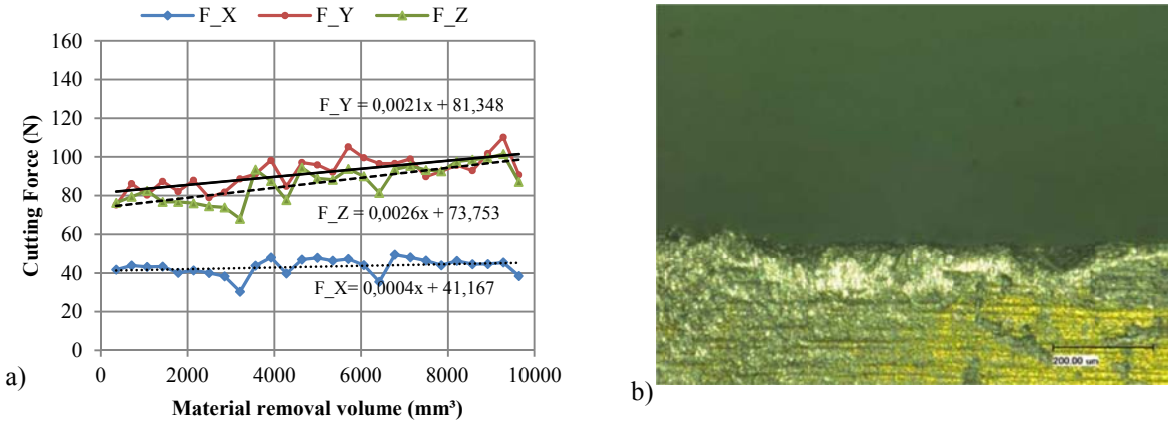

Figure 2-20: (a)The effect of milling time on the process forces with laser (b) flank wear appearance at the end of the milling process [74].

3 Material Modeling in Machining Process

3.1 Johnson-Cook Material Model

Johnson and Cook [75] introduced an empirical model for the flow stress in materials. This model is a phenomenological model which considers plastic strain, strain rate and temperature. Three multiplicative brackets represent strain hardening, strain rate hardening and thermal softening. The Johnson-Cook material model does not refer to internal variables such as crystal system, anisotropy, grain size and movement of dislocation which principally cause plastic deformation.

$$\sigma_{eq} = (A + B\varepsilon^{n})\left(1 + C\ln\left(\frac{\dot{\varepsilon}}{\dot{\varepsilon}_0}\right)\right)\left(1 - \left(\frac{T - T_r}{T_m - T_r}\right)^{m}\right) \qquad \textbf{Equation 3-1}$$

where σ_{eq} is the equivalent flow stress, ε is the equivalent (effective) plastic strain, $\dot{\varepsilon}$ is the equivalent plastic strain rate normalized with a reference strain rate $\dot{\varepsilon}_0$, T_m the melting temperature of material and T_r is room temperature, while A, B, C, n and m are the material

constants. The great advantage of the Johnson-Cook material model can be stated in the simple method of determination of its material constants.

Table 3-1: The Johnson-Cook material constants of Ti-6Al-4Ti according to different references.

	A	**B**	**C**	**n**	**m**	**Strain rate range s^{-1}**	**Maximum true strain mm/mm**	**Temperature °C**
Lee-Lin [76]	782.7	498.4	0.028	0.28	1.0	2000	0.3	
Lee-Lin [41]	724.7	683.1	0.035	0.47	1.0	500-3000	0.35	up to 1100
Meyer-Kleponis [77]	862.5	331.2	0.012	0.34	0.8	000.1,0.1,2150	0.57	
Kay [78]	1098	1092	0.014	0.93	1.1	up to 10^4	0.6	
Seo et al. [79]	997.9	653.1	0.0198	0.45	0.7	1400	up to 0.25	1000
Dandekar, et al. [61]	1080	1007	0.01304	0.6349	0.77			

The required tests (compression, tensile or torsion) are designed at constant strain rates while temperatures reach from room temperature to high temperatures. Parameter A is the yield stress at room temperature and a strain rate of 1 s^{-1}. With plotting the rigid-plastic true stress-true strain curve on a logarithmic scale, the slope of the curve is n. The amount of stress as the plastic strain reaches the value of 1 signifies parameter B. To obtain parameter C, the slope of the curve of the true-stress versus the logarithm of the strain rate is determined at constant temperatures. The parameter m, is determined by two flow stresses, one at the room temperature and another one at the high temperature while the plastic strain and strain rate do not change. The data are put in the following relation as a result of the division of two flow stresses [80]. Generally, the Johnson-Cook model reliably reproduces value of flow stresses at low strain rates. With increasing the strain rates, the fluctuations in flow stress in terms of strain rate hardening and thermal softening has been reported. At high strain rates, the deformation mechanisms can be changed, e.g. in Ti-6Al-4V alloy (which consists of a majority of the hexagonal α-phase). With increasing the strain rate increases the twin fraction, (as anisotropy dependent deformation mechanism). This deformation mechanism leads to the higher strain rate hardening at low temperature which the Johnson-Cook material model is unable to predict acceptably for this kind of material behavior. T. W. Wright [81] has evinced another bug of the model in terms of initial rate of thermal softening. It could be argued as the deficiency of the model when it comes to generating the deformation localization and plastic instability. The rate of the thermal softening goes into infinity as $m < 1$ and goes into zero as $m > 1$ at room temperature. Furthermore, if the thermal softening parameter is supposed to

be equal one, the rate of thermal softening does not change until the temperature reaches melting point.

However, the proposed constitutive material model by Johnson and Cook is extensively used in the finite element simulation of diverse material processing. Furthermore, several research studies have been performed to determine the material constants for a wide range of materials (Table 3-1). These arguments create a platform to modify the model in the areas with high strains, strain rates and temperatures, in fact, where there is still a lack of informative experimental outcomes.

3.2 Johnson-Cook Material Model in Simulation of Machining Process

The Johnson-Cook material model is the most widely used flow stress rule in simulation of cutting processes. From the point of view of the calculated cutting forces and achieved chip morphology, the material model has been evaluated by many researchers. Now and again, the model's constants were optimized by minimizing the error between the calculated cutting forces and the experimentally determined one. Applying Johnson-Cook's material model solely does not bring the segmented chip morphology which is demanded with scholars in the field of the simulation of machining process.

3.2.1 Modified Johnson-Cook Material Model at High Strains

Since the result of the split Hopkinson pressure bar (SHPB) is limited to the strain ranges of 0.3-0.4, the typically predicted strain values in the machining process (0.5 up to 5) cannot be covered. Therefore, the understanding of the local material behavior during the cutting process still is located in the grey area. A modified Johnson-Cook material model has been used by Calamaz [82] and Sima [83]. The modifications consider the strain softening which is defined as decreasing the flow stress with increasing strain over a critical strain value. From the metallurgical viewpoint, the decreasing of the localized flow stress at the high strain is justified by the dynamic recovery and/or recrystallization which leads to a microstructural rearrangement. The microstructural evolution consists of the dynamically fine recrystallized grains (nano-scale) with a low dislocation density.

Experimental investigations by Rittel [84, 85] and Duan et al. [86] are presented also by means of microstructure changing in the adiabatic shear bands of serrated chips of Ti-6Al-4V and hardened high strength steel (30CrNi3MoV). Rittel showed that a micro-structural evolution at the area near the shear localization occurred before the formation of the adiabatic shear band which is in opposition to attendance of the equiaxed grains at the center of the shear band [87]. Both studies are based on the microscopical analysis of the potential shear band (interrupted test at lower strains than cause adiabatic shear) and shear band areas.

Rittel's investigations stated the very similar microstructures for both tests which were concluded for a prior dynamic recrystallization procedure. On the other hand, the result of Peirs et al. [87] showed major finer elongated grains (below 100 nm) in shear band with an equiaxed portion in the center of band at the low deformed test while these nano-scale grains were not observed at the high strain test. Needle-like martensitic morphology was justified for high temperatures in shear band.

The above mentioned modified model takes into account the serrated chip formation as a result of dynamic recrystallization instead of the overcoming the thermal softening. This means that the dynamically fine recrystallized grains deform easier and consequently also the localization of the shear deformation.

The modified model (TANH) helps to predict better saw-tooth chip formation in Ti-6Al-4V and INCONEL 718. The reason for this is a hidden failure model (but here instead of an update, the value of stress components equal to zero, the stresses decrease continuously) with a critical strain value.

$$\sigma_{eq} = \left(A + \frac{B\varepsilon^n}{exp(\varepsilon^a)}\right)\left(1 + Cln\left(\frac{\dot{\varepsilon}}{\dot{\varepsilon}_0}\right)\right)\left(1 - \left(\frac{T - T_r}{T_m - T_r}\right)^m\right)\left(D + (1 - D)\left[tanh\left(\frac{1}{(\varepsilon + S)^c}\right)\right]^e\right) \quad \textbf{Equation 3-2}$$

where $D = 1 - \left(\frac{T}{T_m}\right)^d$, $S = \left(\frac{T}{T_m}\right)^b$.

The effect of the model constants on the flow stress curve is listed in Table 3-2 where it has been studied numerically by Sima.

Table 3-2: The effect of defined material model constants in the modified Johnson-Cook material model (TANH) on the flow stress.

Modified J-C model (TANH) parameters	Effect on the flow stress curve
S	Decreasing the critical strain value depending temperature
D	Decreasing the flow stress at the high strains depending temperature
a	Slope of the flow stress decreasing after the critical strain value at high strains
b	Position of maximum flow stress (critical strain value)
c	Slope of the flow stress decreasing after the critical strain value at low strains
d	Magnitude of strain softening

Figure 3-1 compares schematically the original Johnson-Cook material model with the modified one. As it can be seen in contrast to the modified form, with increasing strain the

value of stress continuously increases which is not appropriate for a simulation of machining process with high values of strains (1 up to 5).

A considerable disadvantage of this modification turns out to find out the material constants. Unfortunately, no comprehensive and experimental investigations have yet been done to systematically determine theses constants. The material constants are limited to the Ti-6Al-4V and Inconel 718 which are based on the numeric fitting.

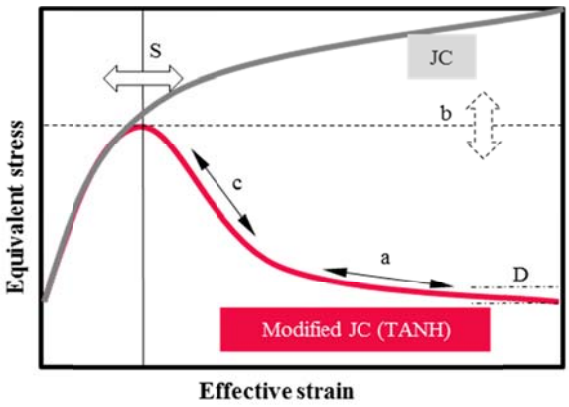

Figure 3-1: Schematic comparison between the Johnson-Cook model and TANH modified model.

3.2.2 Cockcroft and Latham Crack Criterion

Cockcroft and Latham criterion [88] predicts the crack that is initiated as the value of the following integral reaches a critical damage value, D_{CL}:

$$D_{CL} = \int_0^{\varepsilon} \sigma_1 \, d\varepsilon \qquad \textbf{Equation 3-3}$$

Where σ_1 is the positive part of the principal stress (for machining), ε is the effective strain, σ_1 is zero for the negative value of principal stress.

Since this model is an energy balance equation and the total plastic work remains constant during deformation, data from uniaxial tensile stress tests are sufficient for all temperatures, strains and strain rates [89]. As can be concluded from above mentioned integral, the areas with the high strain as the compression stress due to the tool transmission to tensile stress are susceptible for crack initiation. This means the crack can occur in the primary shear zone with a distance from the tool tip. The cracks depending on the cutting velocity can be propagated up to the free surface of the work piece. The chip segmentation in machining of hard to machine material as a result of the ductile fracture came across clearly in the debate about microscopic investigation of Sun et al. [59], where he did not find any evidence of cracks in chips, but rather kind of smooth sliding material on each other.

In the finite element simulation, there are two choices as an element reaches the critical value: deleting or softening. The deleting of elements is more relevant for the modeling of the catastrophic failure and the latter is not different to the thermal softening due to shear localization which is more in conformity with the original model of Cockcroft and Latham which uses the equivalent stress instead of the positive part of principal stress. It means the value of D is equal to the area under the curve flow stress versus the strain until a critical strain.

3.2.3 Johnson-Cook Damage Model

In comparison to Cockcroft and Latham fracture models, the Johnson-Cook damage model [78] considers different factors such as triaxiality of the stress state, temperature, the strain rate and strain. The model is conceived to predict the critical fracture strain based on the accumulative incremental strain which includes the previous loading. In the finite element analysis, the fracture begins at an element greater than one, where the damage value (D_{JC}) in a given element is calculated in accordance with:

$$D_{JC} = \sum \left(\frac{\Delta \varepsilon}{\varepsilon_f} \right) \qquad \textbf{Equation 3-4}$$

where $\Delta\varepsilon$ is the difference between the incremental equivalent plastic strains for an element and ε_f is the strain fracture at the respective time step which is determined with:

$$\varepsilon_f = \left[D_1 + D_2 exp\left(D_3 \frac{\sigma_H}{\sigma_{eq}} \right) \right] \left[1 + D_4 ln\left(\frac{\dot{\varepsilon}}{\dot{\varepsilon}_0} \right) \right] \left[1 + D_5 \left(\frac{T - T_r}{T_m - T_r} \right) \right] \qquad \textbf{Equation 3-5}$$

σ_H is the hydrostatic pressure:

$$\sigma_H = \frac{\sigma_1 + \sigma_2 + \sigma_3}{3} \qquad \textbf{Equation 3-6}$$

Where the σ_1, σ_2 and σ_3 are the main normal (principal) stresses.

As can be seen in Equation 3.5, the constants D_1, D_2 and D_3 are related to the stress state, D_4 characterizes the model dependency at high strain rates while the parameter D_5 controls the material behavior at high temperatures. Generally the material under compression states tends to build the shear fracture. Hence, as the failure appears under tensile states, this tendency goes in the direction of fracture due to the void formation and void growth. It means if the triaxiality stress state ($\sigma^* = \sigma_H/\sigma_{eq}$), is between -1/3 and 0, the Johnson-Cook damage model takes into account only the shear fracture and the required strain for fracture decreases with increasing the triaxiality stress. From another side, if the triaxiality stress exceeds 1/3, the damage model is restricted in fracture due to the void growth [90]. Since the amount of

damage in FEM simulations increases continually with the simulation step, the according model is suitable for ductile fracture which is also related to gradual growing of voids.

The Johnson-Cook damage model in the simulation of machining has been used as damage criterion for chip breakage prediction [91, 92] and also as a chip segmentation criterion [93, 94]. Zhang [94] has used the Johnson-Cook damage model to determine the damage initiation and energy based fracture model for decreasing the flow stress afterwards in a shear limited contact area system.

3.2.4 Thermo-plastic Shear Instability

Under specific conditions, the plastic strain can be localized and leads to the catastrophic shear which is called adiabatic shear. It is proposed that the flow instability begins as the flow stress achieves a maximum value:

$$\left(\frac{d\sigma_{eq}}{d\varepsilon}\right) = 0 \qquad \textbf{Equation 3-7}$$

As can be seen, the instability initiates as the slope of the stress-strain curve becomes negative which means the thermal softening overcomes the strain hardening. In other words, the heat generation due to the plastic deformation drops the flow stresses more than the increasing of flow stresses due to the work hardening.

With the consideration that the plastic flow is a function of strain, strain rate and temperature:

$$\sigma_{eq} = \sigma_{eq}(\varepsilon, \dot{\varepsilon}, T) \qquad \textbf{Equation 3-8}$$

Then, the differential $d\sigma_{\mathrm{eq}}$ can be written:

$$d\sigma_{eq} = \frac{\partial\sigma_{eq}}{\partial\varepsilon}d\varepsilon + \frac{\partial\sigma_{eq}}{\partial\dot{\varepsilon}}d\dot{\varepsilon} + \frac{\partial\sigma_{eq}}{\partial T}dT \qquad \textbf{Equation 3-9}$$

which it can be rewritten in form of:

$$d\sigma_{\mathrm{eq}} = (Strain\ hardening)d\varepsilon + (Strain\ rate\ hardening)d\dot{\varepsilon} + (thermal\ softening)dT \qquad \textbf{Equation 3-10}$$

Bai [95] had solved the above mentioned instability criteria analytically with a series of assumptions using the first law of thermodynamics, Fourier's equation and equation of motion. He drew a conclusion from his calculations that adiabatic deformation and no work hardening are two significant ways in instability of flow. However, here is achieved the same criteria for instability of plastic flow with an assumption that the strain rate is constant during the deformation in case of adiabatic deformation:

$$d\dot{\varepsilon} = 0$$ **Equation 3-11**

Therefore, the equation leads to:

$$d\sigma_{eq}|d\dot{\varepsilon} = 0 = \frac{\partial \sigma_{eq}}{\partial \varepsilon} d\varepsilon + \frac{\partial \sigma_{eq}}{\partial T} dT = 0$$ **Equation 3-12**

and we obtain:

$$\frac{\partial \sigma_{eq}}{\partial \varepsilon} d\varepsilon + \frac{\partial \sigma_{eq}}{\partial T} dT = 0$$ **Equation 3-13**

then the instability criteria simplifies to:

$$\frac{\partial \sigma_{eq}}{\partial \varepsilon} d\varepsilon = -\frac{\partial \sigma_{eq}}{\partial T} dT$$ **Equation 3-14**

or

$$\frac{(Strain\ hardenning)}{(Thermal\ softening)} = -\frac{dT}{d\varepsilon}$$ **Equation 3-15**

then, it is assumed that the plastic work converts into heat:

$$q = W_p = \int \sigma_{eq}.d\varepsilon$$ **Equation 3-16**

If the process is the adiabatic at each time increment, it means that the heat conduction can be neglected, and then it can be concluded:

$$\rho c_p dT = \sigma_{eq}.d\varepsilon$$ **Equation 3-17**

and put in the equation, we obtain:

$$\frac{\frac{\partial \sigma_{eq}}{\partial \varepsilon}}{\frac{\partial \sigma_{eq}}{\partial T}} = -\frac{\sigma_{eq}}{\rho c_p}$$ **Equation 3-18**

In order to calculate a critical strain for the beginning of the strain localization, in the case of the Johnson-Cook flow law, the strain hardening is:

$$\frac{\partial \sigma_{eq}}{\partial \varepsilon} = (nB\varepsilon^{n-1})\left(1 + Cln\left(\frac{\dot{\varepsilon}}{\dot{\varepsilon}_0}\right)\right)\left(1 - \left(\frac{T - T_r}{T_m - T_r}\right)^m\right)$$ **Equation 3-19**

and also the equation is partially differentiated with respect to temperature:

$$\frac{\partial \sigma_{eq}}{\partial T} = (A + B\varepsilon^n)\left(1 + Cln\left(\frac{\dot{\varepsilon}}{\dot{\varepsilon}_0}\right)\right)\left(\frac{-m}{T - T_r}\left(\frac{T - T_r}{T_m - T_r}\right)^m\right) \qquad \textbf{Equation 3-20}$$

Finally, put equation X and Y in equation Z to attain a polynomial equation, which critical strain (ε_c) for instability initiation is considered as unknown:

$$\varepsilon_c^{2n} + \frac{2A}{B}\varepsilon_c^n - \frac{\rho c_p n(T_m - T_r)}{Bm\left(1 + Cln\left(\frac{\dot{\varepsilon}}{\dot{\varepsilon}_0}\right)\right)\left(\frac{T - T_r}{T_m - T_r}\right)^{m-1}}\varepsilon_c^{n-1} + \left(\frac{A}{B}\right)^2 = 0 \qquad \textbf{Equation 3-21}$$

This equation, which is similar to the equation of Rafenbberg [96], should be solved for each element in each time increment in the finite element analysis. After it nucleates, a shear band would propagate forward and this post-instability process linked to a local softening or a final fracture. As can be seen in the above equation, if thermal softening parameter (m) is equal to 1, the critical strain is not dependent on the temperature, except that the density and the specific heat vary with temperature. Also, the critical strain is not related to the thermal conductivity, because with the assumption of the adiabatic condition at each unit of time, the last term of energy equation is omitted:

$$\dot{W}_p = \rho c_p \frac{\partial T}{\partial t} - \lambda \Delta T \qquad \textbf{Equation 3-22}$$

where Δ is a Laplace operator.

It should be mentioned that in the second alternative of instability in the analytical solution of Bai, where the work hardening is zero, thermal conductivity and strain rate hardening are embedded in the instability criterion.

3.3 2D FEM simulation of Orthogonal Cutting

In this section a finite element model is developed in DEFORM 2D to resolve the influence of different approaches to achieve serrated chip morphology in the orthogonal cutting of Ti-6Al-4V. The Software owns the implicit Lagrange mesh formulation and is able to handle large deformations, but requires frequent re-meshing. The software supports automatic local re-meshing, based on the impacted weighting factors [97]. In the regions of high strain, strain rate and temperature, the generated mesh is finer (in the primary shear zone and the area near the tool tip). Use of adaptive re-meshing increases the stability of the simulation where a dynamic mesh modification along the deformed or distorted elements is possible. Furthermore, in order to minimize the interpolation error during the re-meshing, the stress and strain state can be saved as nodal data, too. The DEFORM does not use any chip separation

criterion, and material flows based on the prescribed and the calculated velocity field of the free surface nodes in the direction of minimum energy. The model of work piece is assumed as plan strain geometry and consists of 10000 elements with a size ratio of 10. The tool has 4877 elements with fine mesh at the tool tip (about 0.004 mm). The model represents the work piece as a rigid-plastic part and the tool as a rigid body with a four node element for both. The rigid-plastic modeling decreases the computing time remarkably. The length of the work piece is 1 mm and its total thickness is 0.1 mm. The uncut chip thickness is 0.1mm. The cutting tool has a clearance angle equal to 5° while the rake angle is 11 ° and the rounding of the tool nose has a radius of 0.015 mm. In order to simulate the milling process, the cutting tool moves with a constant velocity in the feed direction. It is assumed that the 90% of the plastic deformation work converts to heat and 100% of friction work converts to heat. The thermal boundary conditions (convection and radiation) were considered by applying the convection heat transfer coefficients and the emissivity to all elements with external contact. The bottom surface of the work piece was fixed in three directions. Based on Zorev's model [98], the frictional condition at the tool-chip interface express with the following relations:

$$\tau = \mu\sigma_n, \quad \text{if} \quad \mu\sigma_n < \bar{m}\frac{\sigma_{eq}}{\sqrt{3}}$$

$$\tau = \bar{m}\frac{\sigma_{eq}}{\sqrt{3}}, \quad \text{if} \quad \mu\sigma_n \geq \bar{m}\frac{\sigma_{eq}}{\sqrt{3}}$$

Equation 3-23

where σ_n is normal stress, τ is shear stress, σ_{eq} the equivalent flow stress, μ is Coulomb friction coefficient and $\bar{m}$ is shear factor. The values for $\bar{m}$ and μ were kept constant at 0.7 and 0.5, respectively. The heat interface coefficient between tool and chip is taken as a constant value of 50 kW/m²K, which is assumed because of the high pressure and temperature on the rake face and chip contact area the heat transfer rate from the chip to the tool is high. Thermo-physical material properties of Ti-6Al-4V which in all simulations in this chapter have been used are listed in Table 3-3. The constants for original Johnson-Cook material model for all simulations are taken from Lee-Lin [41] in Table 3-1. The modified Johnson-Cook material model (TANH) constants are listed in Table 4-4. The critical value for Cockcroft and Latham criterion is chosen from DEFORM material library equal to 240. The Johnson –Cook damage model constants are taken from G. Kay [78] where D_1, D_2, D_3, D_4 and D_5 are -0.09, 0.25, -0.5, 0.014 and 3.87, respectively.

In order to compare the simulation result with the experimental chips, three chip characterization parameters are considered: tooth spacing, tooth depth and chip body. The experimental chips (Figure 3-2) were taken from the literature (Ye et al. [99]). A comparison has used the average space between teeth (AST) and average depth of teeth (ADT), both of which increase with the cutting velocity. Based on the reported results and microscopically images of Ye et al., the AST for cutting velocity of 3, 30 and 300 m/min are 0.03, 0.05, and 0.07 mm, while the ADT are 0.01, 0.03 and 0.06 mm, receptively. For very high cutting

speeds, the AST is 0.11 mm and ADT is 0.075 mm. It is worth noting that in our observation in next section 3.3.4, the frequency of shear instability incident is more important than AST and ADT. Also, it is significant whether occurred shear instability is strong enough for complete chip segmentation.

Table 3-3: Applied thermo physical properties of Ti-6Al-4V in simulations [100].

Temperature (°C)	Thermal conductivity (W/m K)	Specific heat (J/kg K)	Density (Kg/m³)	Thermal expansion (mm/mm° C)
25	7	546	4420	0.000007075
100	7.45	562	4406	0.0000073
300	10.15	606	4381	0.0000079
500	12.6	651	4350	0.0000085
700	15.5	694	4324	0.0000091
900	20.2	734	4294	0.0000097
995	19.3	641	4282	0.000009985
1100	21	660	4267	0.0000103
1300	23.7	696	4240	0.0000109
1500	25.8	732	4205	0.0000115
1650	28.4	759	4189	0.00001195

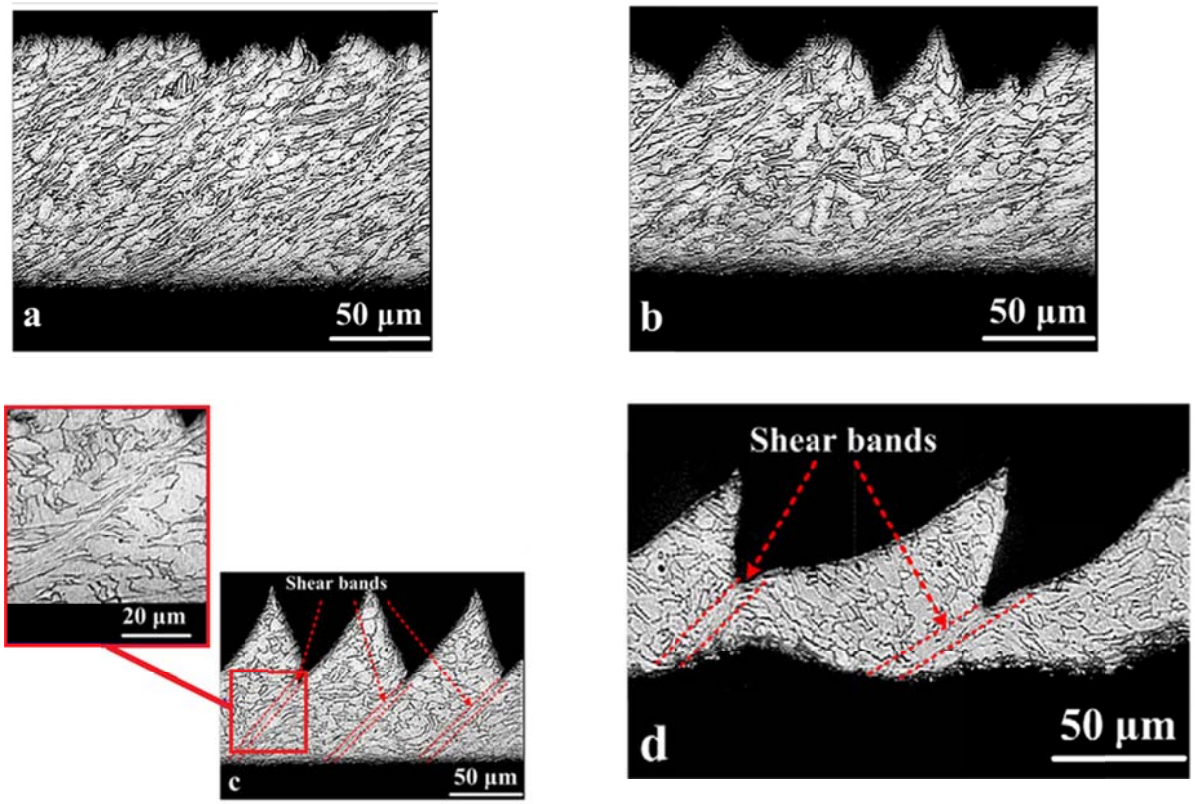

Figure 3-2: Achieved chip of Ti-6Al-4V for cutting velocities of (a) 3 (b) 30 (c) 300 and (d) 1800 m/min with feed rate of 0.1 mm/rev and a rake angle of 0°. The marked shear bands have been done by the original authors [99].

3.3.1 Chip Morphology using the Modified Johnson-Cook Material Model at High Strains

The model was implemented in DEFORM software by setting the flow stress at the different temperature, strains and strains as tabular data format. The simulations were carried out at five different cutting velocities (0.3, 3, 30, 300 m/min) with the constant uncut chip thickness of 0.1 mm. The simulation results according to the chip morphology, the effective strain and the temperature are illustrated in Figure 3-3. The results show the reaction of the model to the strain localization with increasing the cutting velocity. Generally, the effective strain is localized gradually with the increase of the cutting velocity. Figure 3-3.a shows the localized strain bands even at the low cutting velocity of 0.3 m/min. However, these bands do not propagate themselves into the free surface and following chip segmentation. The frequency between the bands is higher than the intervals at the higher velocities. Also, with increasing the cutting velocity, the contact area between the tool and chip decreases and the chip curvature increases. It can be a reason for the decreasing of heat transfer ratio between tool and chip surface with increasing cutting velocity, although the contact pressure increases (in next Section 4.2).

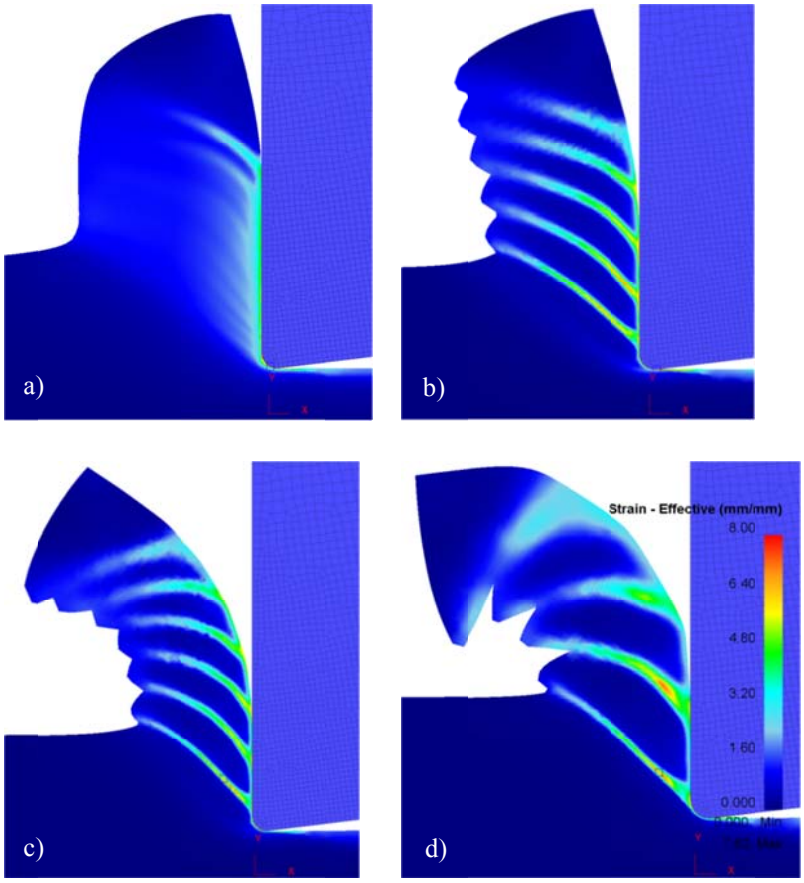

Figure 3-3: Equivalent strain distribution and chip morphology in simulation of orthogonal cutting with velocities of (a) 0.3 (b) 3 (c) 30 and (d) 300 m/min with feed rate of 0.1 mm/rev and a rake angle of 0°.

3.3.2 Chip Morphology using the Cockcroft and Latham Crack Criterion

DEFORM software uses the Cockcroft and Latham crack criterion as default setting and the damage value is calculated for each element with a strain rate above the limiting strain rate. The concerning elements with the damage value higher than the critical value (D_{CL}= 240 which is taken from DEFORM material library) are deleted with the all related element data. The following rough element surface can be eliminated with the setting boundary curvature in the weighting factor in the re-meshing after deletion of each element (Figure 3-4).

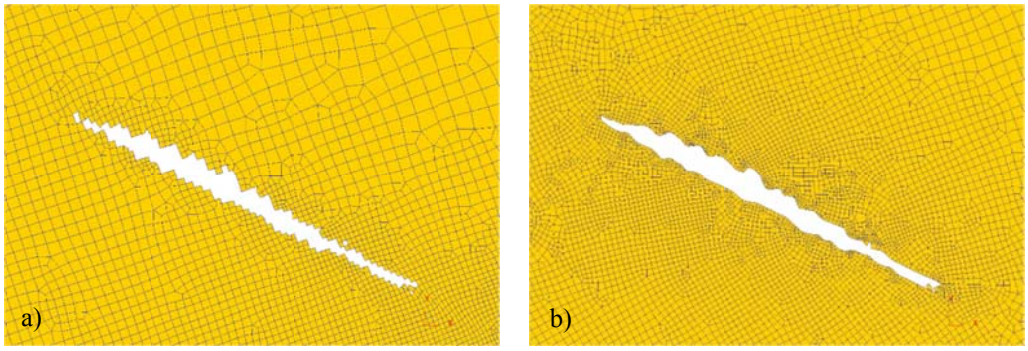

Figure 3-4: (a) Deleted elements (b) softened elements with re-meshing.

In order to keep a stability of simulation, crack appearance begins as an element with a connectivity of less than three exceeds the critical value or in other words, if an element with a maximum principle stress (positive portion) greater than the tensile strength of the material is located on the free surface. Figure 3-5 presents the fracture progress in the simulations. The periodic ductile fracture (segmented interval is approximately every 3.10^{-5} s for a cutting velocity of 300 m/min) as the underlying cause of chip segmentation in the machining process is not considered in the present work. Hence, in the current simulations, the element deletion was not studied and the flow stresses for the corresponding elements has been degraded.

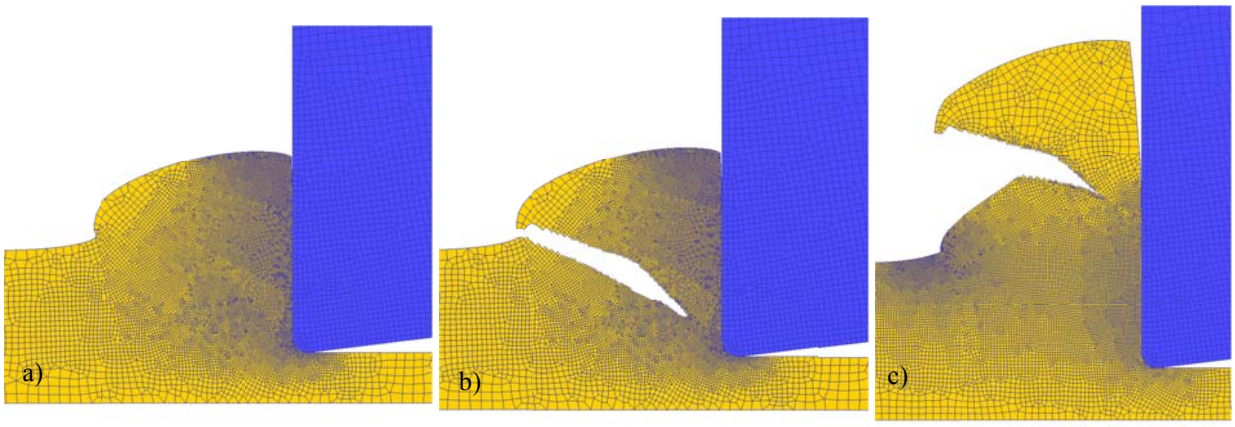

Figure 3-5: Chip evolution with the element deleting procedure at (a) 3.3e-5, (b) 3.4e-5 and 7.4e-5 s with cutting velocities of 300 m/min, feed rate of 0.1 mm/rev and a rake angle of 0°.

Figure 3-6 shows the Cockcroft and Latham crack damage distribution at low level cutting velocities (0.3, 3 and 3 m/s). As described earlier, the appropriate regions for the damage initiation is a transition area where the compressive stress state changes into the tension stress state. In these velocities, the appropriate region is located under the tool tip rather than in front of the tool tip. As the damage starts, the direction of propagation is oriented towards the positive part of the major principal stress in contrast to the maximum shear stress which it is supposed to be. With increasing the cutting velocity, the direction of propagation is prone to the maximum shear stress that leads to a bigger shear angle and follows thicker chips in comparison to the chip thickness at high level velocities.

Figure 3-7 presents the damage distribution, strain localization and temperature localization at the cutting velocity 5 m/s in the different time steps. The damage initiates (red scalar is the value above 240 which can be attributed to the critical value of Ti-6Al-4V) in front of the tool tip, in this moment the flow stress of element is decreased by up to 10 % of the original effective stress of the element which allows more shear strain in the direction of maximum shear stress. The next damaged elements are located in this direction and induce the shear localization. It should also be noted that initiation site of strain, strain rate and temperature localization are the same with the failure initiation in contrast to the previously described model. The experimental images of the chip cross section demonstrate the strain localization directly from the tool tip.

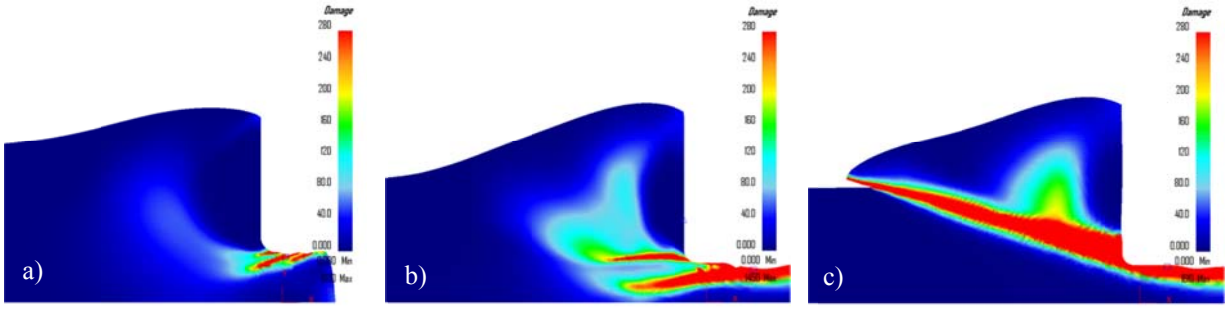

Figure 3-6: Cockcroft and Latham crack damage distribution at cutting velocities (a) 0.3 (b) 3 and (c) 30 m/min with feed rate of 0.1 mm/rev and a rake angle of 0°.

The right sides of Figure 3-7.c illustrated the temperature distribution in the achieved chip. The temperature distributions along the material model depend on the strain rate and friction behavior at the contact areas. With increasing the cutting speed, the temperature in the chip increases. But the localization of the generated temperature within the narrow bands can be justified by the dropping the flow stress as the effective strain reaches a critical value. In simple words, the displacements of the according nodes are allowed to be higher at each time step of simulation which leads to a high strain rate and strain consequently. At high strain rates, the time is not sufficient for the transfer of the generated heat due to the plastic

deformation. The temperature at the localized strain band in the simulation rises up to 500°C, which can be a reason for occurrence of the dynamic recrystallization.

3.3.3 Chip Morphology using the Johnson-Cook Damage Model

The according damage model was written in usr_msh.f subroutine which provides to save the effective strain of previous increment in a user defined variable without reference to the re-meshing procedure. The incremental and summation of the Johnson-Cook damage model were saved and were illustrated in the post processor interface. However, the subroutine does not have access to the flow stress which is requested for the modeling of chip segmentation. In this section, only the initial location of damage is presented, where the beginning of strain localization could be conducted to the high damage value along the shear band.

Figure 3-8 shows the incremental and summation of the Johnson-Cook damage model with increasing the cutting velocity at the beginning of the simulation. A first observation of results verifies that the model is not sensitive enough with the cutting velocity and consequently the effective strain rate, although the term due to the strain rate in the model is embedded. As a reason it can be stated that the constant regarding to the strain rate (D_4) fades the variation of strain rate. As mentioned earlier, the main attempt to determine the model's constants focuses on the first three ones (D_1, D_2, D_3) and torsion tests at different shear strain rates do not cover the high strain rate regime that is discovered during the simulation. As can be explored from Figure 3-8, the damage begins from the contact area in front of the tool tip which expresses high values of plastic strain which can be used as an initiation point for beginning the damage (softening). Zhang [94] has been used this model in combination with Hillerborg's fracture model and limiting shear stress on the tool-chip interface for modeling of serrated chip morphology. However, the result of these investigations does not produce clearly a transition from the continuous chip morphology into the segmented chip at least in frequency in localization attempts. This chip morphology transition happens with the varying of the rake angle where the negative rake angle increases the tendency of segmentation.

As the rake angle goes into the negative values, the hydrostatic pressure at contact area between rake face and chip increases which emphasizes the trend to the serrated chip morphology.

The result of simulation in this work shows that the value of incremental Johnson-Cook damage model at low cutting velocity (0.005 m/s) is higher than the according value at high cutting velocity (5 m/s). Because of that, the simulation is studied only at the beginning steps, the temperature at the high cutting velocity for corresponding elements (40 °C) at the according element is higher in comparison with the low one (250 °C). Because of that, the softening and strain localization is not realized in this study, the propagation and distribution of the damage model in further simulation steps is not meaningful as a tool for comparison between the different cutting conditions.

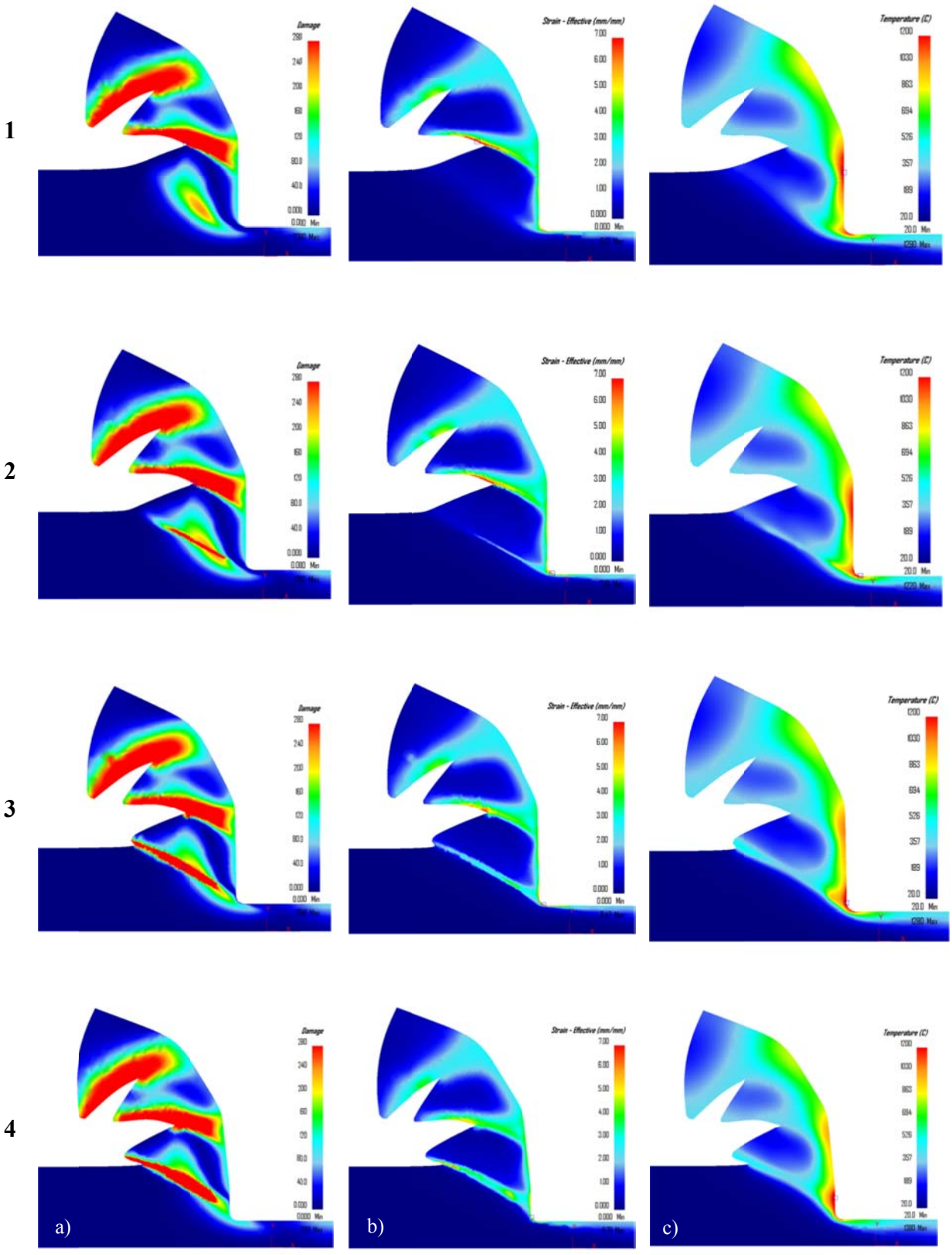

Figure 3-7: Cockcroft and Latham crack (a) damage, (b) effective strain and (c) temperature distribution with cutting velocities of 300 m/min, feed rate of 0.1 mm/rev and a rake angle of 0° for a tooth formation in four stages.

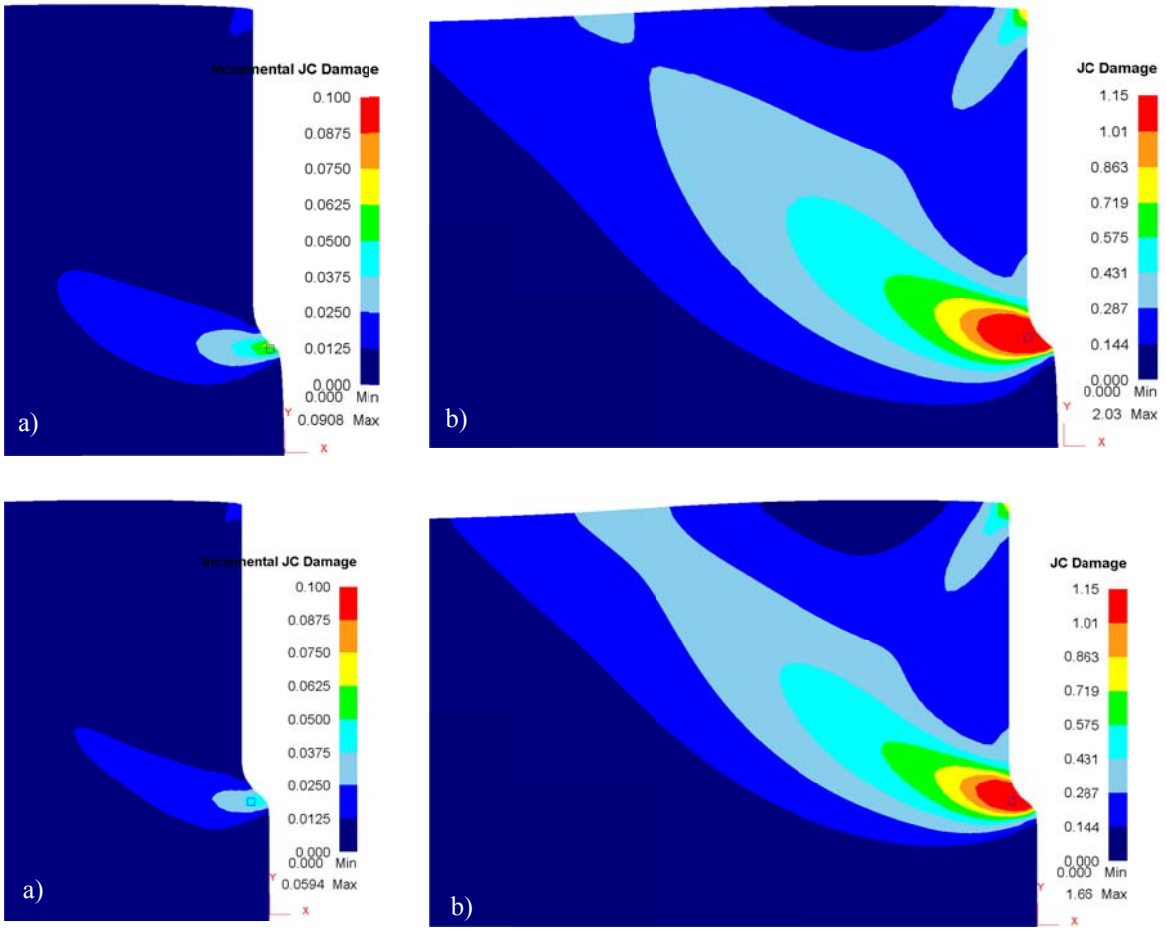

Figure 3-8: Johnson- Cook damage distribution and evolution at cutting velocities (a), (b) 0.3 m/min and (c), (d) 300 m/min.

3.3.4 Chip Morphology using the Thermo-Plastic Shear Instability

As described theoretically above, the first derivative of flow stress with respect to the strain determines the maximum value of flow stress. However, the material overcomes a way with the massive plastic deformation before every catastrophic failure. The flow stress degradation after the stress peak could be followed as a linear, parabolic, exponential or even any arbitrary manner. We define post peak flow stress as a fraction of flow stress which is calculated at each temperature, strain and strain rate from a flow equation (here the Johnson-Cook equation) as:

$$\sigma_{eq}{}^{n+1} = D_c \sigma_{eq}{}^{n} \qquad \textbf{Equation 3-24}$$

where D_c is the damage evolution parameter.

The damage evolution parameter can be attributed as a relation between the current strain and the critical strain. For example, in case of linear degradation, D_c can be calculated as:

$$D_c = \frac{\varepsilon_c}{\varepsilon}$$ **Equation 3-25**

or for the exponential one:

$$D_c = exp(\varepsilon_c - \varepsilon)$$ **Equation 3-26**

Based on this assumption, Hillerborg proposes a model for the material stiffness degradation in case of ductile fracture. In order to describe the behavior of the material in the post ultimate stress state at the present work, the exponential reduction of flow stress with a lower limit was considered for the isotropic softening of material after achieving the critical strain as:

$$D_c = exp(-a_1 \varepsilon^{b_1})$$ **Equation 3-27**

where a_1 and b_1 are a material constant and have been estimated experimentally. The effect of these constants on the value of D_c is illustrated in Figure 3-9. It should be mentioned that the applied softening path is quite different to the original description where parameter fracture energy is used which depends on the fracture toughness, elastic modulus and the Poisson's ratio.

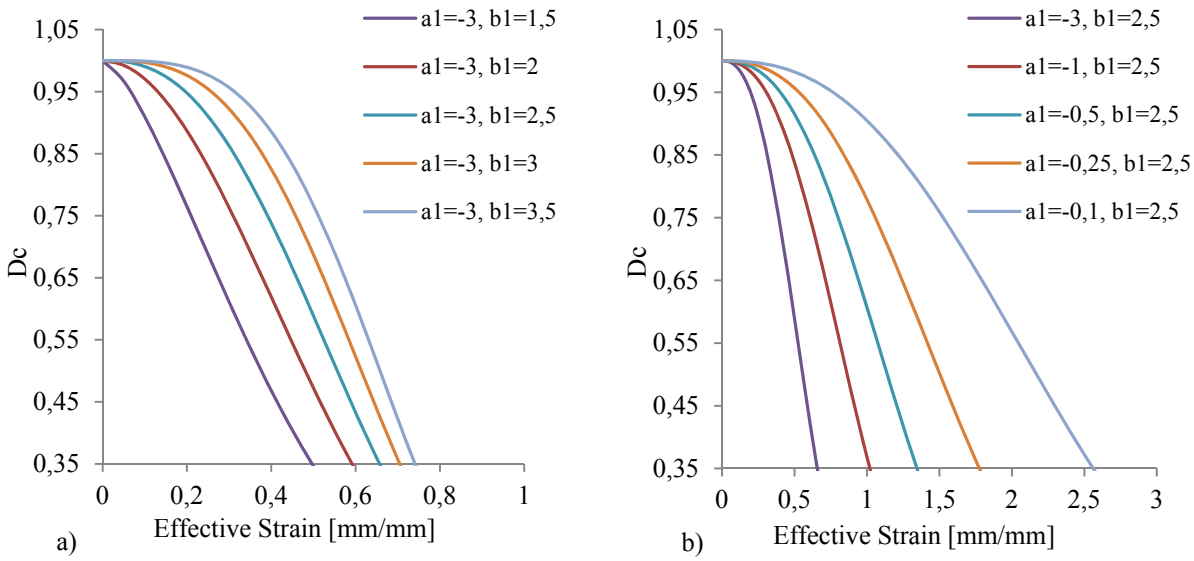

Figure 3-9: The effect of damage parameter constants on the level of flow stress reducing (a) with variation of b_1 and (b) a_1.

The deformation pattern is investigated from two points of view: the frequency and the power of localization. From this arrangement, it is concluded that the strain localization in the continuous chip formation initiates more often but the resulting softening is not adequate for further deformation in sliding the material along the shear band. In contrast to the continuous chip formation, the frequency is less, but the power of shear localization is more. The power

of localization can be defined by describing the development of the softening quantity after that the strain reaches the critical value in terms of an exponential function or the slope of degradation of the flow stress after critical strain. The typical chip morphology achieved from simulation using the thermo-plastic shear instability is illustrated in Figure 3-10.

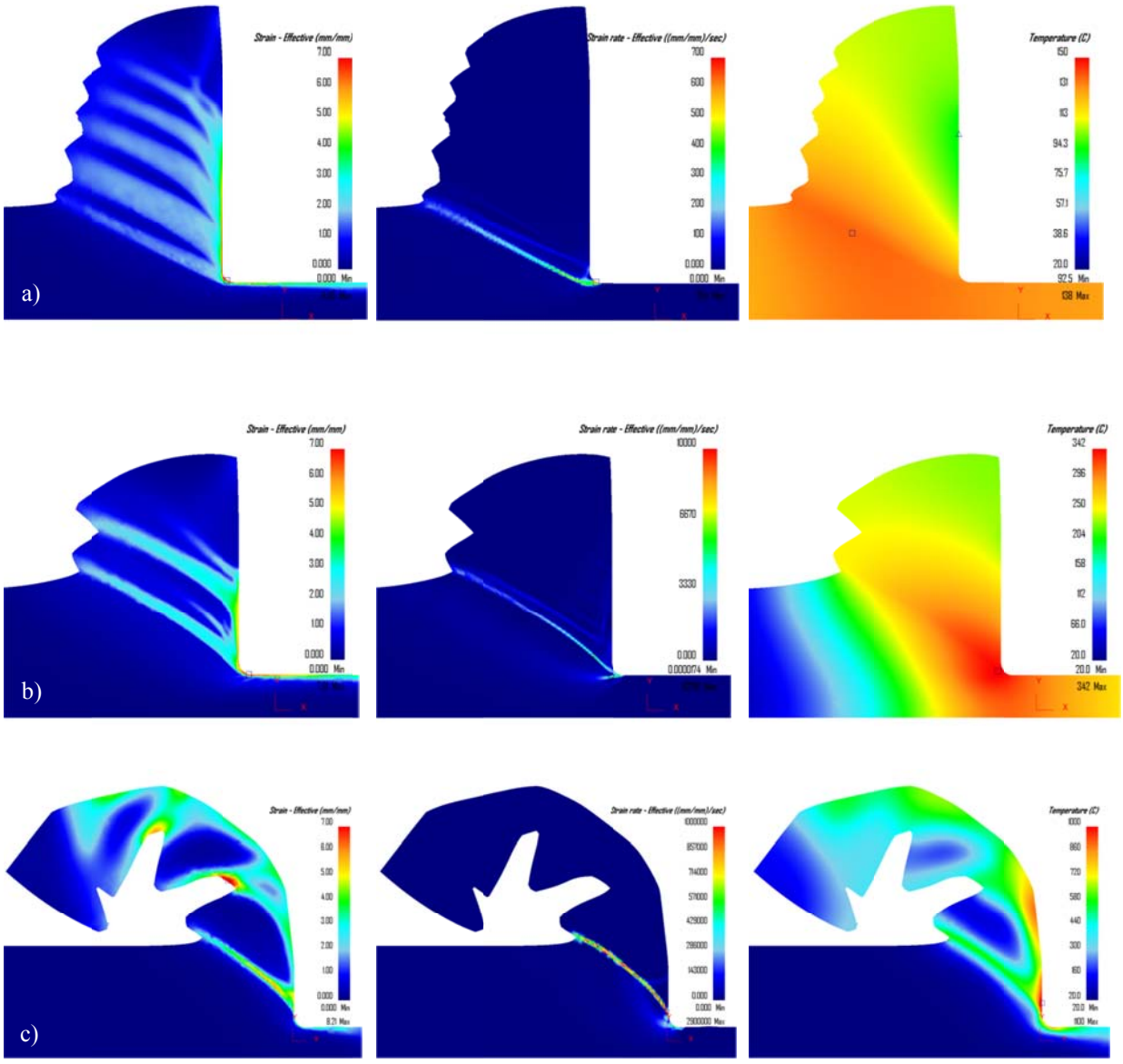

Figure 3-10: Effective strain, strain rate and temperature distribution with cutting velocities of (a) 3, (b) 30 and 300 m/min, feed rate of 0.1 mm/rev and a rake angle of 0°.

As we have mentioned, the creation of the adiabatic shear bands is a highly localized phenomenon, hence, the chip segmentation with respect to the strain pattern, the strain rate and temperature are observed. The plastic strain tends to present in the soft areas where the temperature is high, namely, the contact area between cutting insert and workpiece which refers to the terms of secondary and territory shear zones in the cutting process. On the other

hand, the primary shear zone is suitable for the adiabatic shear because of a high deformation rate. As can be observed from the strain patterns in Figure 3-10, the strain localization begins from the tool tip and tries to reach the free surface of the work piece. The strain pattern in the chip demonstrates that the manner is reproduced itself at low and high cutting velocities.

As mentioned above, the frequency and power of shear bands characterize the variation of cutting velocity. At low cutting velocities, the strain localization in the primary shear zone is repeated more. It means that the number of strain localization is more than the strain localization at high cutting velocities. As the localized strain line reaches the free surface of the work piece, it is a time for starting the next one which does not necessarily lead into a tooth or a deep tooth. The average space between teeth (AST) and average depth of teeth (ADT) at each simulation are illustrated in Figure 3-10. The AST varies from 0.0404 mm at cutting velocity 3 m/min into 0.0651 at 300 m/min while the ADT changes from 0.0157 into 0.0736 mm, respectively.

Table 3-4: Average space between teeth and average depth of teeth for

Cutting velocity [m/min]	Ave. space between teeth [mm]	Ave. depth of teeth [mm]
3	0.0404	0.0157
30	0.0585	0.0378
300	0.0651	0.0736

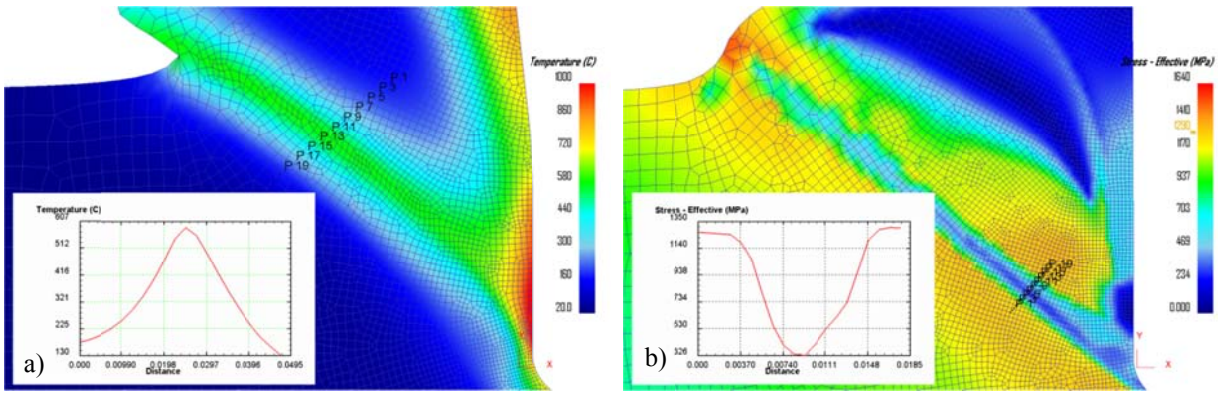

Figure 3-11: (a) Temperature and (b) effective stress distribution in shear bands.

Since at high cutting velocity the time for the heat transfer is not enough, the shear instability in addition to the strain localization leads to temperature localization. Figure 3-11.a shows that the temperature at the shear band reaches up to 600 °C which promotes also a softening affect, where the effective stress drops up to 300 MPa at shear band (Figure 3-11.b). The higher value of ADT means that the deformation takes place longer on the plane with the high strain rate. The deformation is attributed as sliding which can be resembled by a boundary layer between two stationary surfaces in fluid mechanics as is illustrated in Figure 3-12. Because of the difference between the velocities inside and outside of shear band, two upper

and bottom sides can be assumed as a fixed plate. In order to characterize the shear band response on the temperature, at least two elements in shear band should be available; hence, in these simulations the element size at the high strain rates was assumed 0.00135 mm.

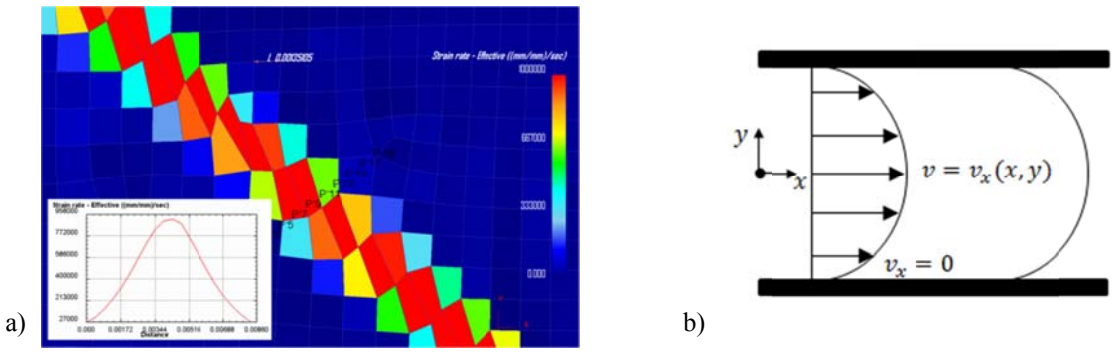

Figure 3-12: Effective strain rate distribution in (a) shear band and (b) boundary layer.

The above mentioned procedure was changed for very high (1800 m/min) and very low cutting (0.3 m/min) velocities which are not relevant in machining of Ti-6Al-4V. In order to realize this high cutting velocity, the Euler-Lagrange approach was utilized in the simulation instead of Lagrange's numerical scheme. In addition of thermo-mechanical shear instability, the energy based Cockcroft and Latham crack criterion (as it introduced in section 3.2.2) was used to achieve high softening (as second softening motor) in the areas where the direction of maximum main stress is changed (as it was explained above). The results of this simulation can be observed in Figure 3-13.

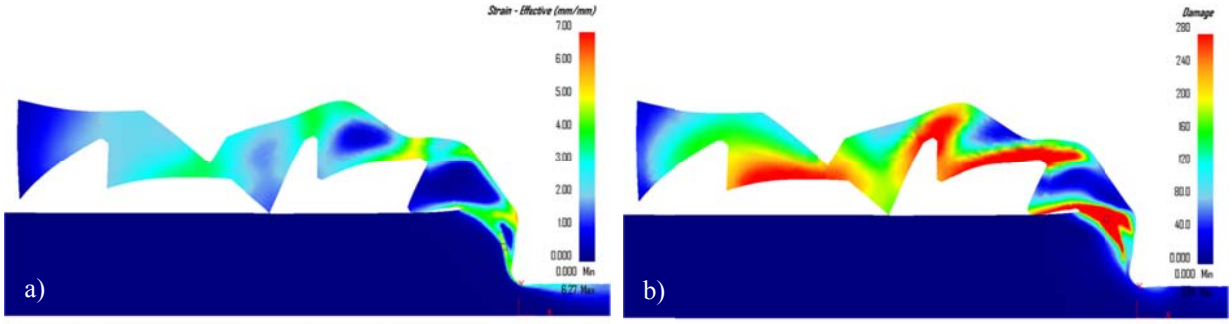

Figure 3-13: Effective strain and Cockcroft and Latham damage distribution with cutting velocities of 1800 m/min, feed rate of 0.1 mm/rev and a rake angle of 11°.

Without mentioning that the cutting velocity in theses simulation with the results of sections 3.3.1 and 3.3.2, the strain localization always begins from the cutting insert tip and it is not obligatory that the shear band propagates itself along the direction of maximum main principal stress. Also, the shear band propagation either reaches the free surface of the work piece or connects the prior band, as is illustrated in Figure 3-14. The applied manner leads to higher value of ADT and a deformed segmentation surface (Figure 3-2) which is expected at high cutting velocities. The deformed chip in contact with the tool surface gives evidence at

very high interface temperature and from the other side with increasing the velocity chip curvature increases where at high temperatures, the deformation is higher. Furthermore, it is a sign of full segmentation because of very powerful shear instability.

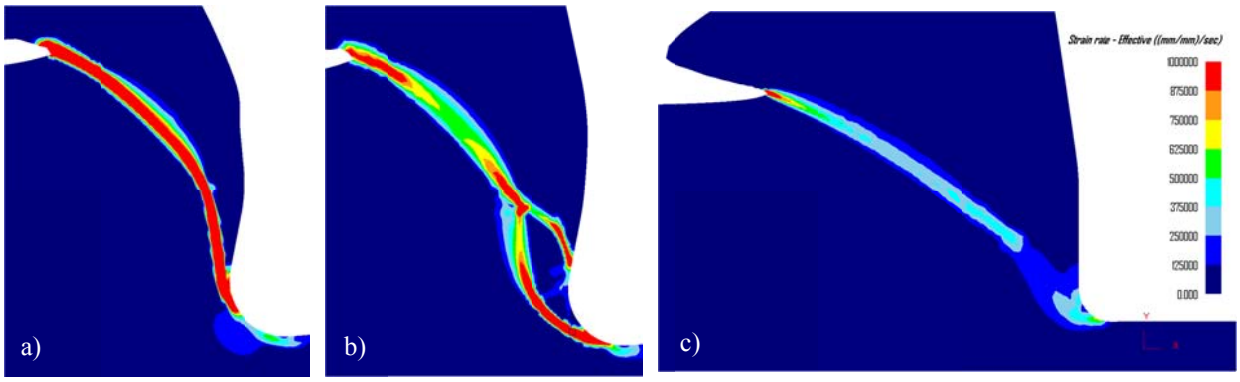

Figure 3-14: Three different paths of shear band prolongation (a) along the secondary shear zone, (b) combination of two shear bands together and (c) along the maximum shear plane.

For the very low cutting velocity, also the model was adjusted after detecting the strain failure which is attributed to the onset of adiabatic shear. It is worth noting that not necessary each critical adiabatic strain leads to a catastrophic failure in this concept. This threshold strain is used here as a point at which the deformation behavior of material begins to change. Based on this principle that at very low cutting velocities, after overcoming the critical strain, the softening behavior of material follows the strain rate, the post damage flow stress degradation can be defined as a function of effective strain rate:

$$D_c = exp(-b_3 \dot{\varepsilon}^{a_3}) \qquad \textbf{Equation 3-28}$$

Since, in these velocities, the strain rate is not so high to conclude a catastrophic failure, but increasing the strain rate leads to limited heat conduction and results in softer material. The achieved chip (Figure 3-15.a) at first sight refers to continuous chip formation which can be expected in the machining of Ti-6Al-4V [99].

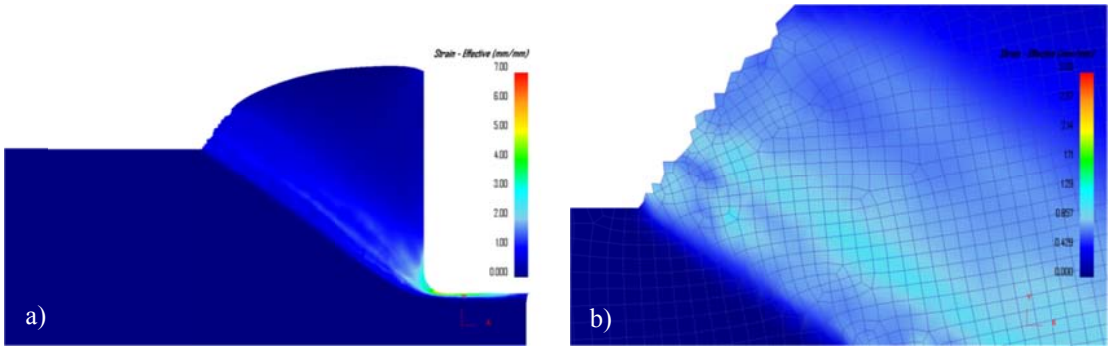

Figure 3-15: (a) Effective strain distribution with cutting velocities of 0.3 m/min, feed rate of 0.1 mm/rev and a rake angle of 0°, (b) extension of weak instability up to free surface.

A special feature of applied manner can be observed in Figure 3-15.b where the AST presents even up to 0.0034 mm and ADT up to 0.0018 mm. These low values are explanatory of high frequency of localization phenomena related the calling of threshold strain. The last two adjustments were considered here as particular cases in the thermo plastic shear instability not as a routine manner. In the Section 3.7, the model will be adjusted to use for 3D simulation where the adiabatic threshold strain solely is not adequate for FE-modeling of material.

3.4 Hot Compression Test

In order to determine the susceptibility of materials to the occurrence of adiabatic shear failure, the compression tests were performed. In this study, a Gleeble® 3800 based on a servo-hydraulic deformation system was used. The Gleeble system with a resistance heating enables the high heating rates (up to 10000°C/s). The temperature of specimens was measured by the welding of K type thermocouple (Ni – Cr [+] vs. Ni – Al [-]) on the longitudinal center of specimens. A maximum stroke rate of 2000 mm/s makes it possible to reach a strain rate of about 0.01 up to100 s^{-1} in the compression test by use of cylindrical specimens with 16 mm height and a diameter of 10 mm. The maximum stroke can be reached of 100 mm and a maximum force of 20 tons in compression test is accessible. The hot compression test using Gleeble® 3800 enables to measure directly stress - strain curves which can be interpreted from a macroscopical point of view. All compression tests with different temperatures (600 and 750 °C) and strain rates (0.01, 1, 10 and 100 s^{-1}) were carried out first to achieve a strain of 1. After an analysis of the stress-strain curves according to the maximum achieved stress state, some tests were repeated for strain 0.4 and 0.6. The aim of this procedure is to investigate the adiabatic shear evolution at different steps of formation up to the occurrence of specimen fracture. The compressed specimens were cut precisely and were prepared for metallography analyses. The metallography parts underwent macro etching (100 ml H2O, 2 ml HNO3 and 0.2 ml HF) and then micro etching (100 ml H2O, 5 ml HNO3 and 2 ml HF) for microscopic examinations at for edges of each specimen. The results of compression test will be presented in section 3.6 for validating of 2D simulations.

3.5 2D FEM Simulation of Compression Test of Ti-6Al-4V

All numerical hot compression tests were performed using the DEFORM 2D software. Table 3-5 shows the performed simulations corresponding to the true strain rate and temperature. An axisymmetric cylindrical rigid-plastic as work piece body accompanied with two flat rigid dies was assumed as model component. The work piece consisted of 7500 four nodes elements with a size ratio of 15. The cylindrical specimen has an initial diameter of 10 mm with a length of 16 mm. The billet was compressed between two dies while the imposed downward vertical displacements were applied on the top die with the constant velocity while the bottom die was constrained in two directions.

Table 3-5: Performed simulation conditions.

Name	Strain rate s^{-1}	Temperature °C	Die velocity mm/s
600_01	0.01	600	0.16
600_1	1	600	16
750_1	1	750	16
750_10	10	750	160

The initial billet temperature was 600°C and the initial die temperature was 25°C. During compression, the heat transfers through the contact area into the die where the coefficient of heat exchange between the deformed metal and the tool was assumed of 10 [W/ mm^2°C]. The specimen loses heat to the environment with a convection coefficient of 0.02 [W/ mm^2°C]. The friction behavior at contact areas between the dies and the work piece follows from the Coulomb's law with a constant coefficient of 0.3. It was assumed that the deformation work converts to heat with an efficiency of 0.9 while the whole friction work converts to the heat.

Ti-6Al-4V was used as work piece material for the studies; the thermo-physical properties of the work piece material were the same as in the previous section. The mechanical behavior was based on the Johnson-Cook material model as used earlier.

3.6 2D Material Model Validation

This section focuses on the microscopic observation of adiabatic shear instability evolution and comparison with the result of the FEM simulation using the before described approach in section 3.2.4. The formation of adiabatic shear band before the incident of fracture is classified in three levels as they are illustrated in Figure 3-16. Figure 3-16.a shows potential nucleation sites for deformation instability where the grains are elongated slightly in one direction but the deformation follows a homogenous regime [101]. Figure 3-16.b clarifies the transition from homogenous deformation into inhomogeneous which leads to a fresh shear band. This thin band is not enough matured for a catastrophic fracture like the thickly formed shear band in Figure 3-16.b. The distinct region of shear band comparison with neighboring domains in Figure 3-16.c gave evidence of the sharp gradient in the strain rate, the strain and the temperature. Figure 3-16.d shows a fracture path in the whole specimen where it is continued from the upper left side to the bottom right side.

This classification helps more for a systematic comparison between the stages of adiabatic shear band formation in simulation and corresponding trial one. The supposed regions in the top-left edge between two parallel lines with 1 till 3 (level of band formation) are identified. In the present study, the evidence of incident, power and propagation of shear bands in the corresponding strains are summarized by visual point of view. This manner is satisfactory for the determining and matching of applied model constants in the previous section.

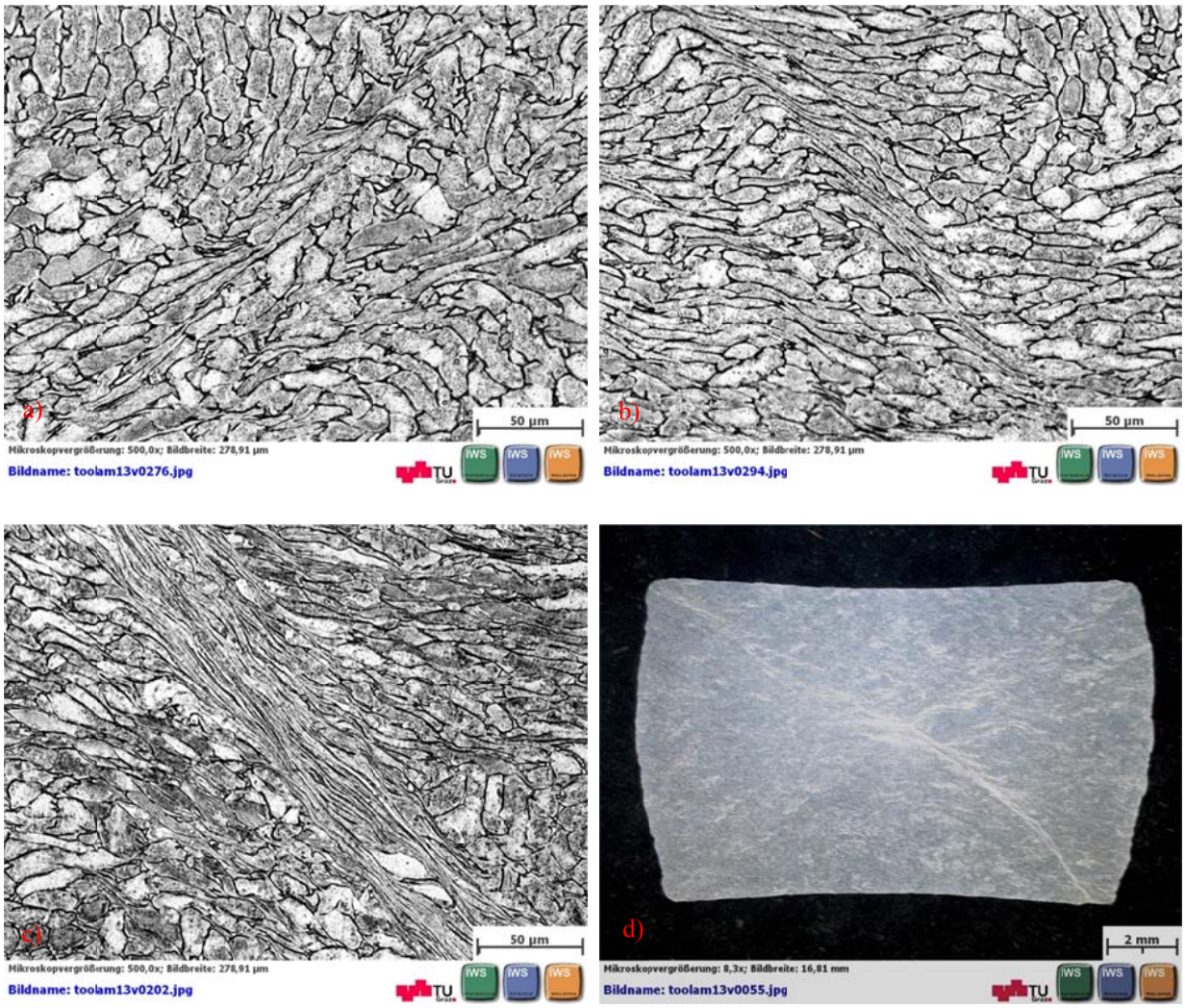

Figure 3-16: (a) Shear band nuclei (b) second type (c) third type of shear band (d) fracture path at true strain of 0.6 with strain rate 100 s^{-1} and temperature 750 °C.

Figure 3-17.a and Figure 3-17.b show the microscopically cross section of specimen at the strain of 0.4 and 0.6 for an initial temperature of 600°C and strain rate of 0.01 s^{-1} in two different types of magnification. At the strain of 0.4, any kind of strain localization is observed while at strain 0.6 can be seen in Figure 3-17.d the second level of shear band. The simulation results in Figure 3-18.a do not show any strain localization and flow stress falling until strains of 0.6. However, the simulation predicts a catastrophic failure at the strain 1 which is in agreement with the experiment in Figure 3-18.c. Because of the Johnson-Cook material model (which is suitable for high rate deformations with defining of reference strain rate of 1 in flow stress equation) is used for determination of shear instability, the general stress state in experimental condition for the low strain rates (0.01 s^{-1}) is less than the simulation results. The final failure simulations happened as all elements along the strain localization areas reach a value of less than 100 MPa.

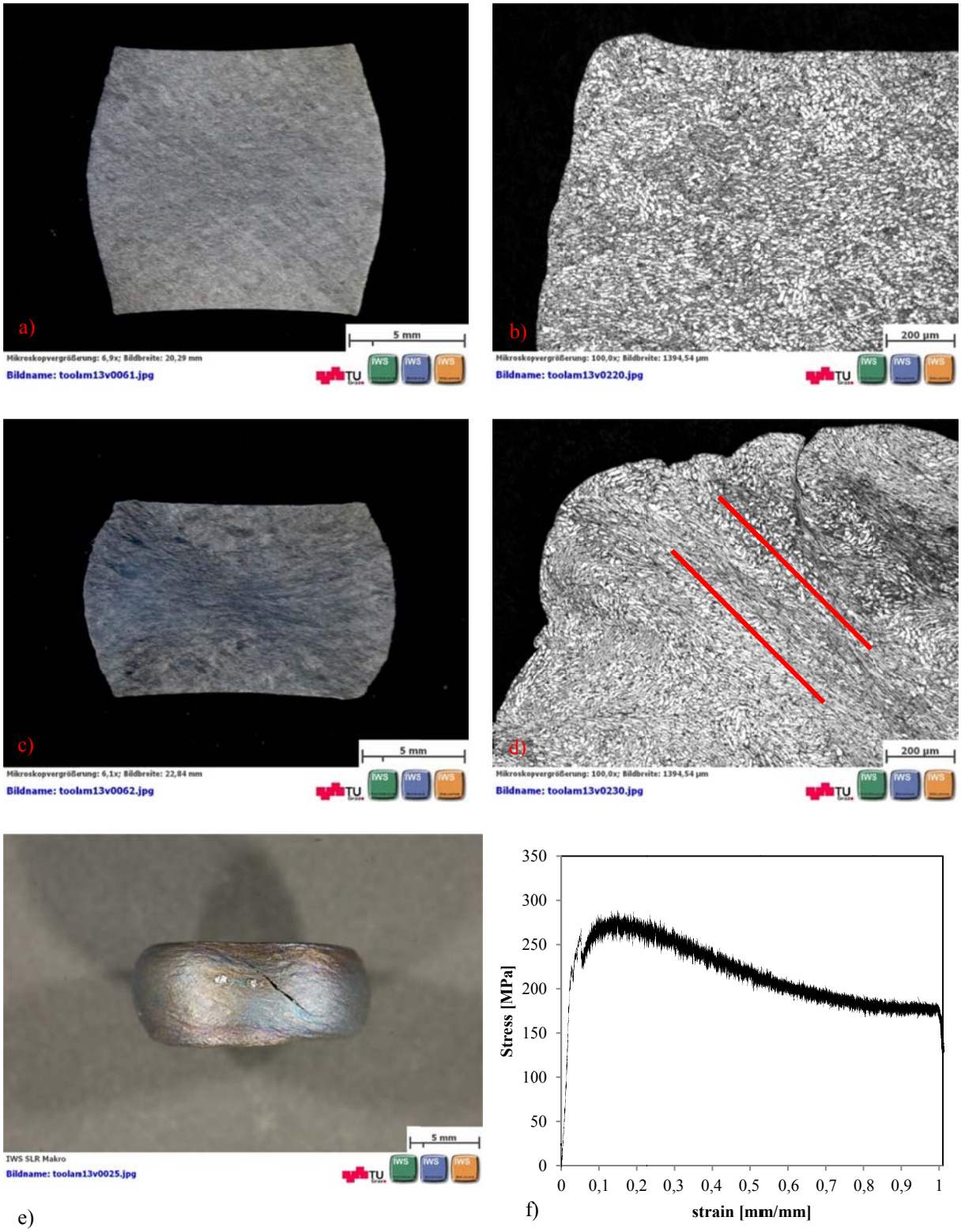

Figure 3-17: (a) The stereo cross section and (b) top-left corner at true strain of 0.4, (c) The stereo cross section and (d) top-left corner at true strain of 0.6, (e) true strain of 1 and (f) engineering stress-strain diagram with strain rate 0.01 s^{-1} and temperature 600 °C .

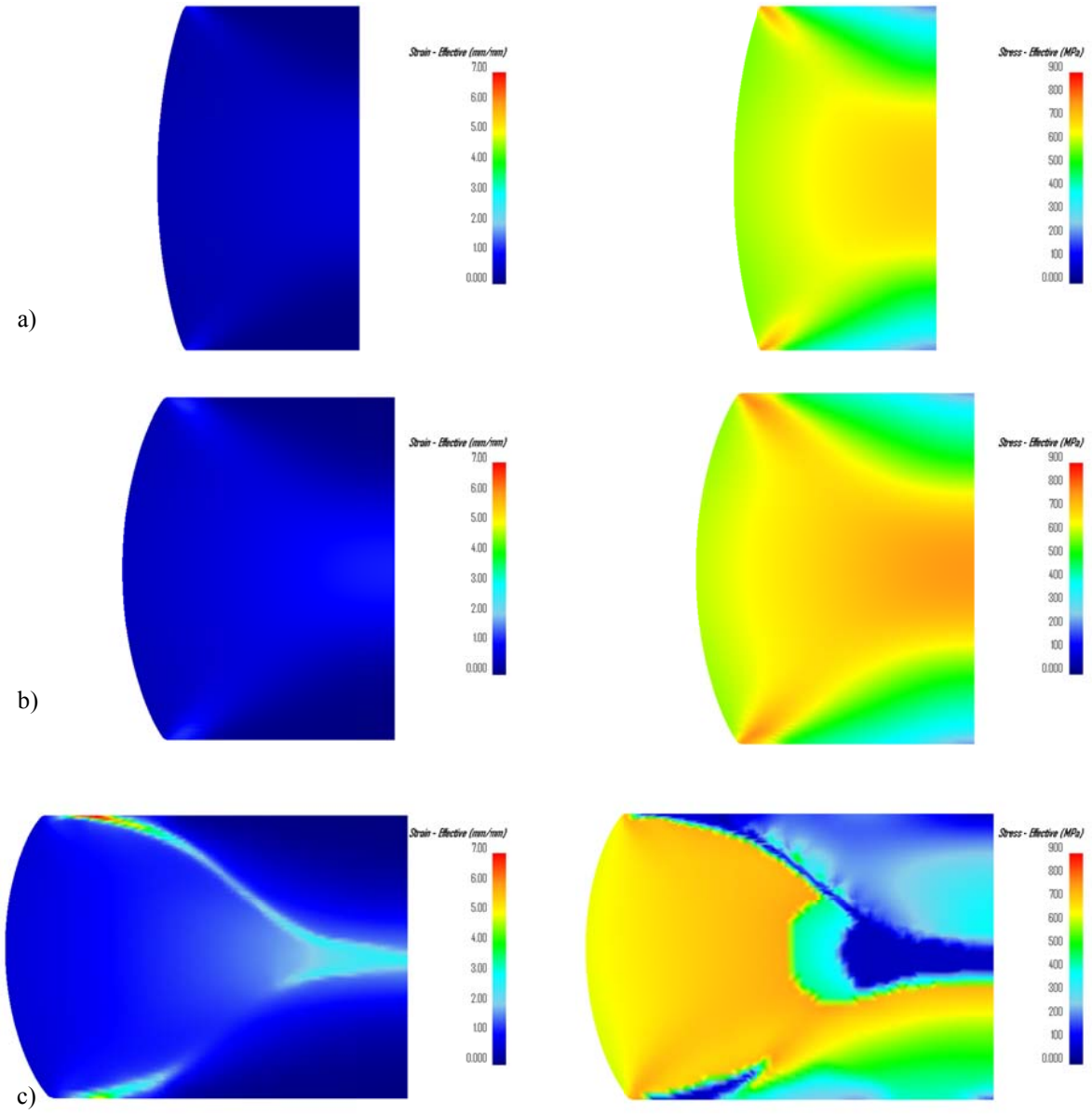

Figure 3-18: Effective strain and stress distribution in true strains of (a) 0.4 (b) 0.6 and (c) 1 with strain rate 0.01 s^{-1} and temperature 600 °C .

The results of the compression test at the temperature of 600 °C and strain rate of 1 s^{-1} (Figure 3-19) do not show shear localization at the strain 0.4 as the simulation result in Figure 3-20. Both simulation and experimental image verifies a shear instability second type at the strain of 0.6. The second type of adiabatic shear band is characterized in simulations with the partial dropping of flow stresses at the potential sites. The predicted finial failure occurs as the specimen reaches 6.7 mm (strain equals to 0.87) in simulation. The repeated shear bands in Figure 3-19.e in comparison with the unique case in Figure 3-17.e give evidence that the final failure happens before the strain reaches the value of 1.

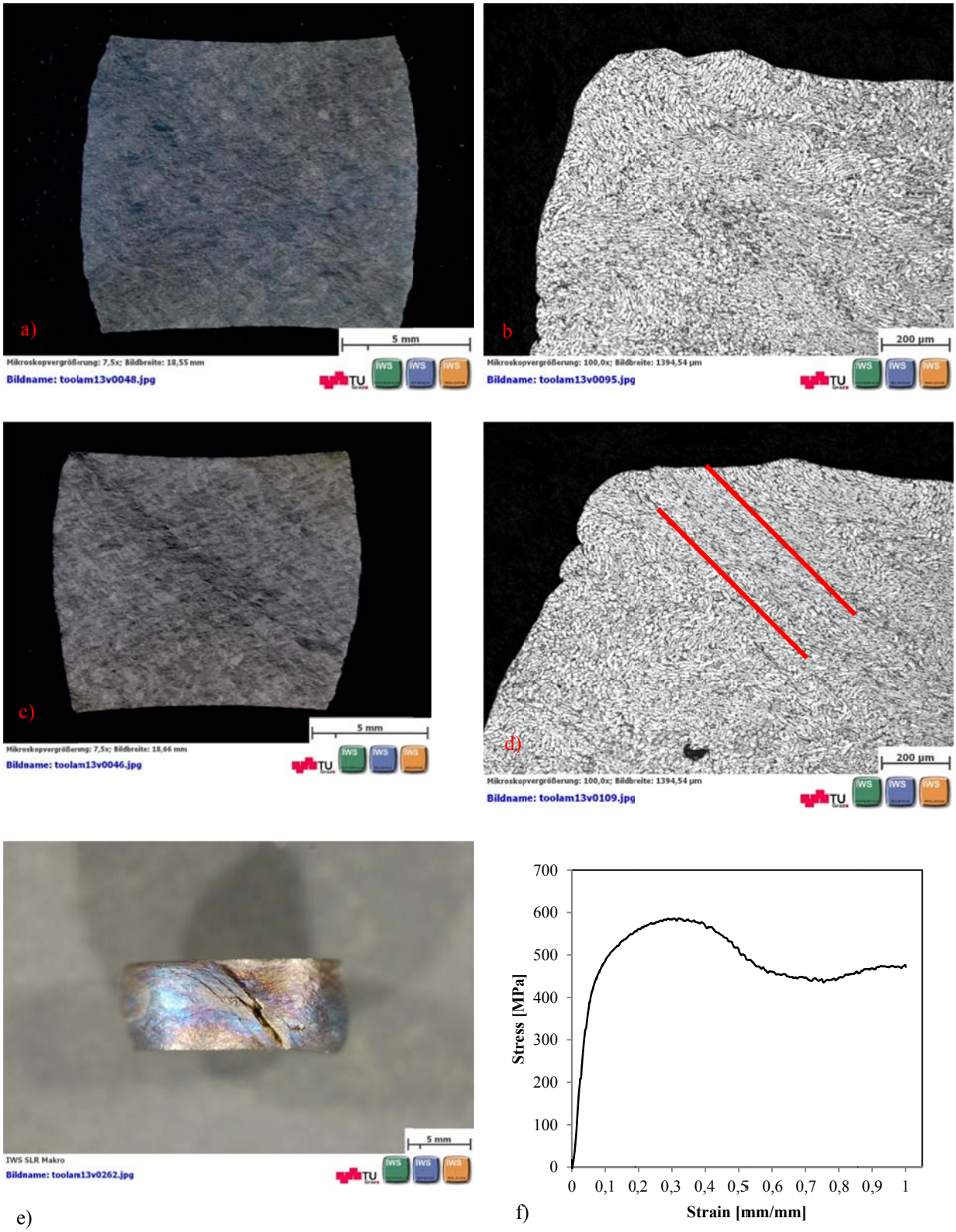

Figure 3-19: (a) The stereo cross section and (b) top-left corner at true strain of 0.4, (c) The stereo cross section and (d) top-left corner at true strain of 0.6, (e) true strain of 1 and (f) engineering stress-strain diagram with strain rate 1 s^{-1} and temperature 600 °C .

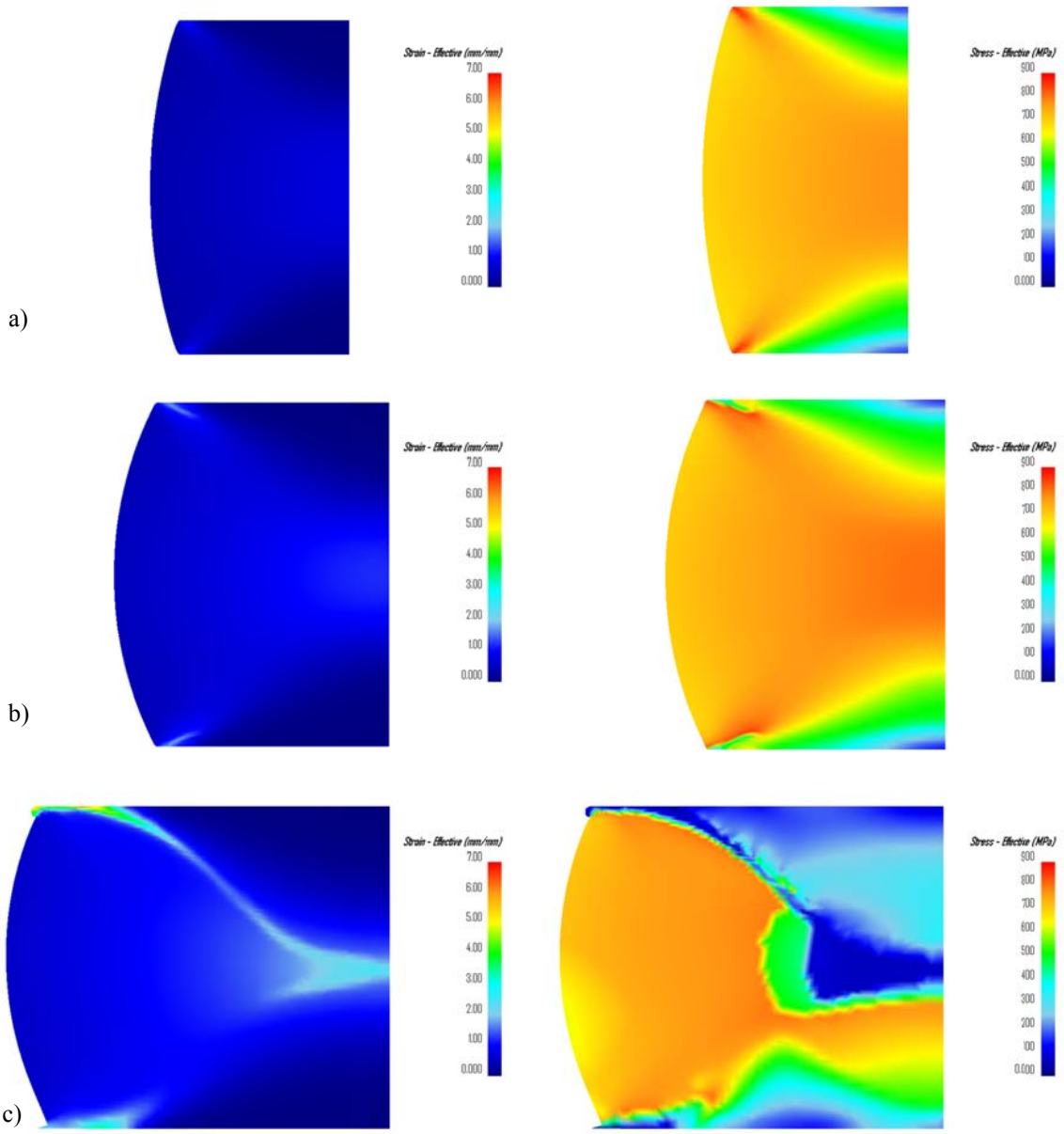

Figure 3-20: Effective strain and stress distribution in true strains of (a) 0.4 (b) 0.6 and (c) 1 with strain rate 1 s^{-1} and temperature 600 °C .

The comparison of the global stress-strain curve between the strain rates 0.01 and 1 s^{-1} states that the global critical strain for peak stress shifts from strain of 0.15 at 0.01 s^{-1}into strain of 0.27 for 1 s^{-1}. Since the goal of this work is focused on the deformation at high strain rates and temperature, the material behavior at low strain rates is not relevant.

As it has been observed for compression tests at 600 °C, the catastrophic failure appears itself in the form of cracks. However, it does not mean that the adiabatic shear band follows crack propagation such as what happened in the case of brittle materials. As the result of the simulations and microscopic images demonstrate, the vulnerable sites for nucleation of adiabatic shear band are the upper edges, bottom edges and center of specimen. As it was

mentioned, these nuclei can be declared in flow behavior as a maximum stress and in the simulation model as the critical strain where both of these aspects can be summarized in local softening. The flow softening in the center of the specimen does not follow a classical adiabatic shear band, because the according zone has undergone the compression stress state. With continuing compression loading, these local softening zones prefer to extend in one direction or in one chosen surface. Thereby, it occurred and agreed with simulation without any additional considerations. As continuous lines of shear band (with the high localized strain as it was illustrated in Figure 3-16.d) are formed, the center of specimen is also undertaken a shear stress or tensile state. This load changing leads to a catastrophic damage, as it was observed in the Figure 3-17.e and Figure 3-19.e.

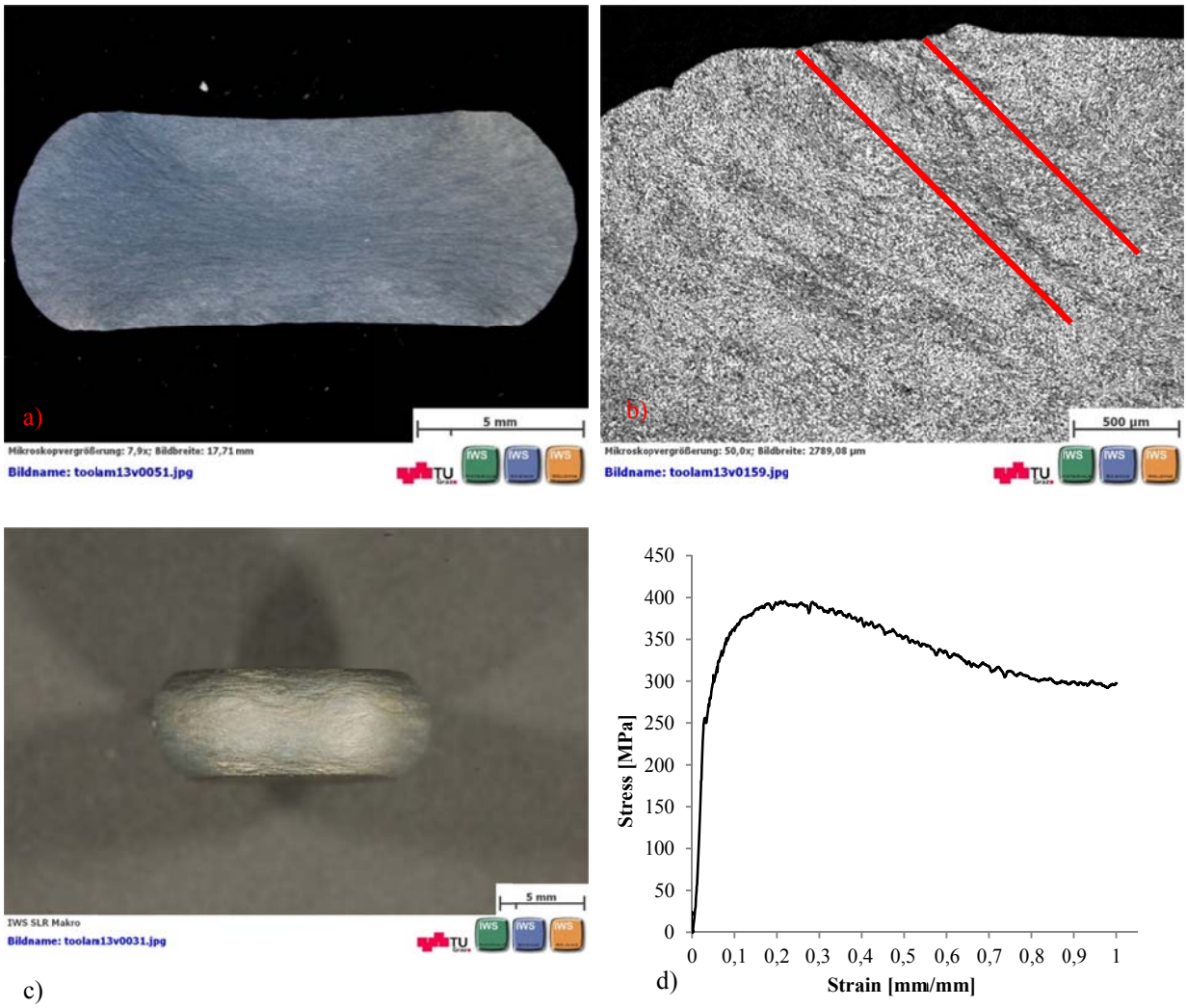

Figure 3-21: (a) The stereo cross section and (b) top-left corner at true strain of 1, (c) The whole specimen at true strain of 1 and (d) engineering stress-strain diagram with strain rate 1 s^{-1} and temperature 750 °C .

The final result of hot compression test at 750 °C and strain rate 1 s^{-1} is illustrated in Figure 3-21. The specimen reaches a strain of 1 without the occurrence of catastrophic failure.

The microscopic image shows a shear instability of the second type in the center and at the specimen edges which are in agreement with the simulation results in Figure 3-22. The FEM result shows also that the effective stress degrades slightly at the strain of 0.6 (Figure 3-22.a), which is attributed to shear instability of the first type. Figure 3-23 presents the cross section of specimen under strain rate 10 s^{-1} and temperature 750 °C. The specimen has achieved the strain of 1 without incident of final failure, although the specimen has inclined to one direction, which expresses a directional softening.

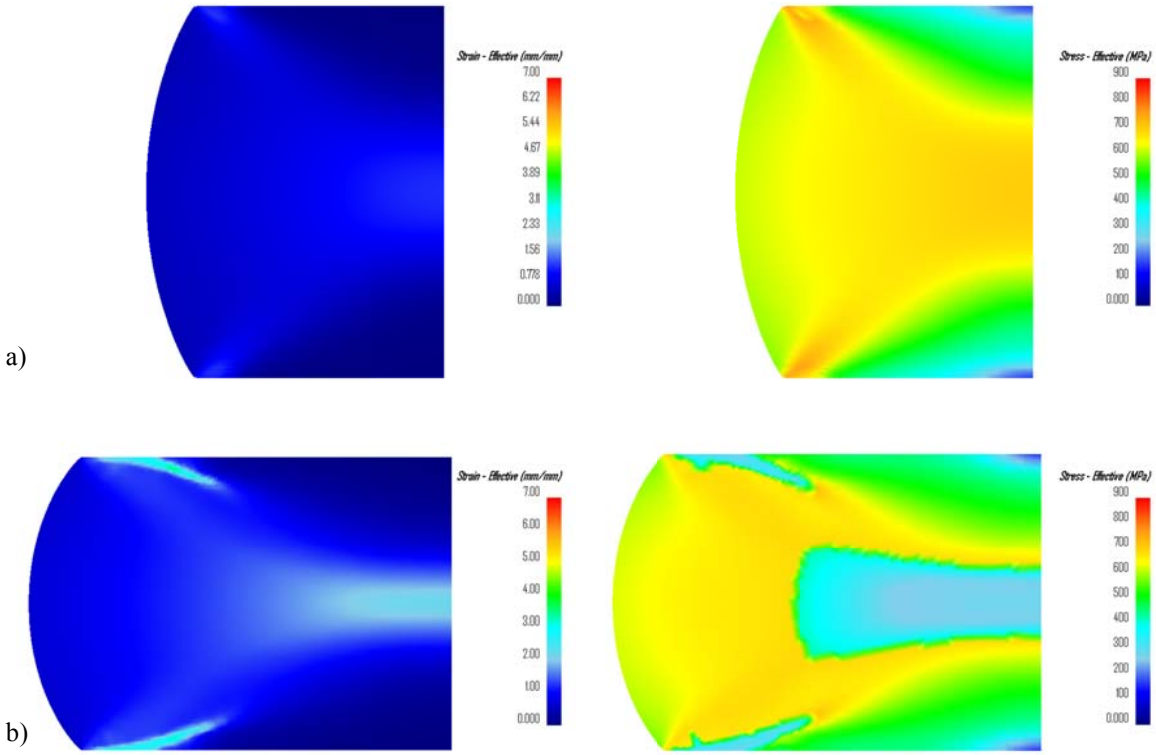

Figure 3-22: Effective strain and stress distribution in true strains of (a) 0.6 and (b) 1 with strain rate 1 s^{-1} and temperature 750 °C .

The simulation predication (Figure 3-24.a) indicates a first type of shear instability at strain 0.6, which is stronger than Figure 3-22.a. The degrading of effective stress (shear instability of second type) was expanded to the susceptible areas (X form window) at the strain of 1. In this study, the reorganization between the different shear instability levels is distinguished via the level of stress degrading. The microscopic and macroscopic investigation shows a thick shear deformation line which consists of the first and second type of shear bands. As discussed before, in low power shear instability (Figure 3-22 and Figure 3-24), the frequency of occurrence is more than the high power deformation instability (Figure 3-18 and Figure 3-20). The simulation and experimental investigation confirms this assumption.

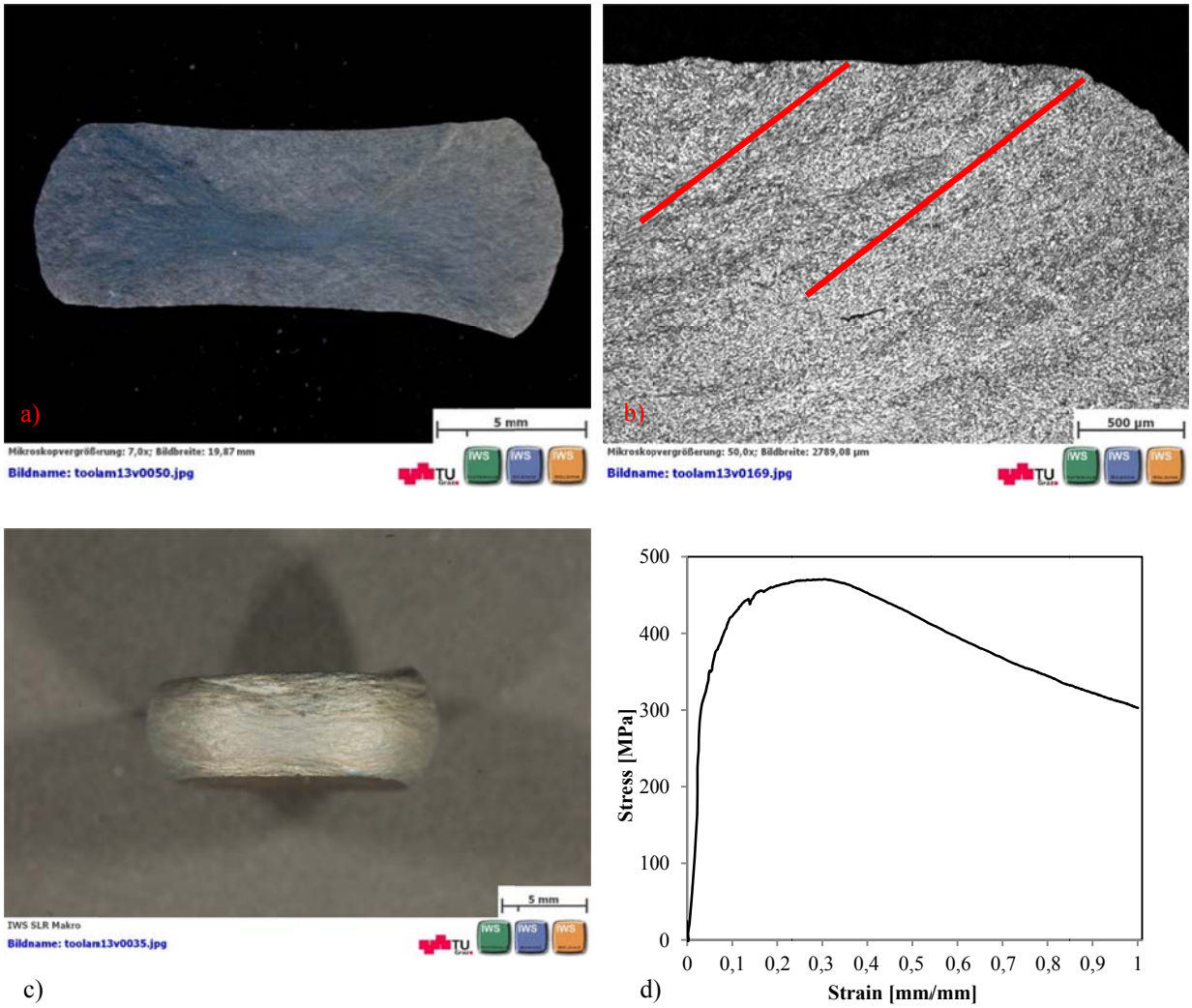

Figure 3-23: (a) The stereo cross section and (b) top-left corner at true strain of 1, (c) The whole specimen at true strain of 1 and (d) engineering stress-strain diagram with strain rate 10 s^{-1} and temperature 750 °C .

Beside temperature and deformation velocity which have been considered in this study, the degree and propagation rate of adiabatic shear bands depend on another parameters. In case of Ti-6Al-4V, morphology of microstructure (as it has been seen, equiaxed α morphology was used in this study) or grain size has an effect on hardness which affects the shear instability. Naturally, the metallurgical material defects also change the adiabatic behavior. These factors in combination with the test accuracy (for example precise contact between dies and specimen or homogeny heating) decrease or increase the stress peak or critical strain for initiation and evolution of bands.

From a numerical point of view, unfortunately, every finite element simulation result involves mesh dependency. In this work, using a relative fine mesh and absence of re-meshing has tried to minimize the interpolation error. The 2D FEM results show good agreement with the compression tests in terms of prediction of beginning of shear instability, determination of

stage of adiabatic shear band and indirectly the prediction of total undergone strain of specimen before the crucial fracture.

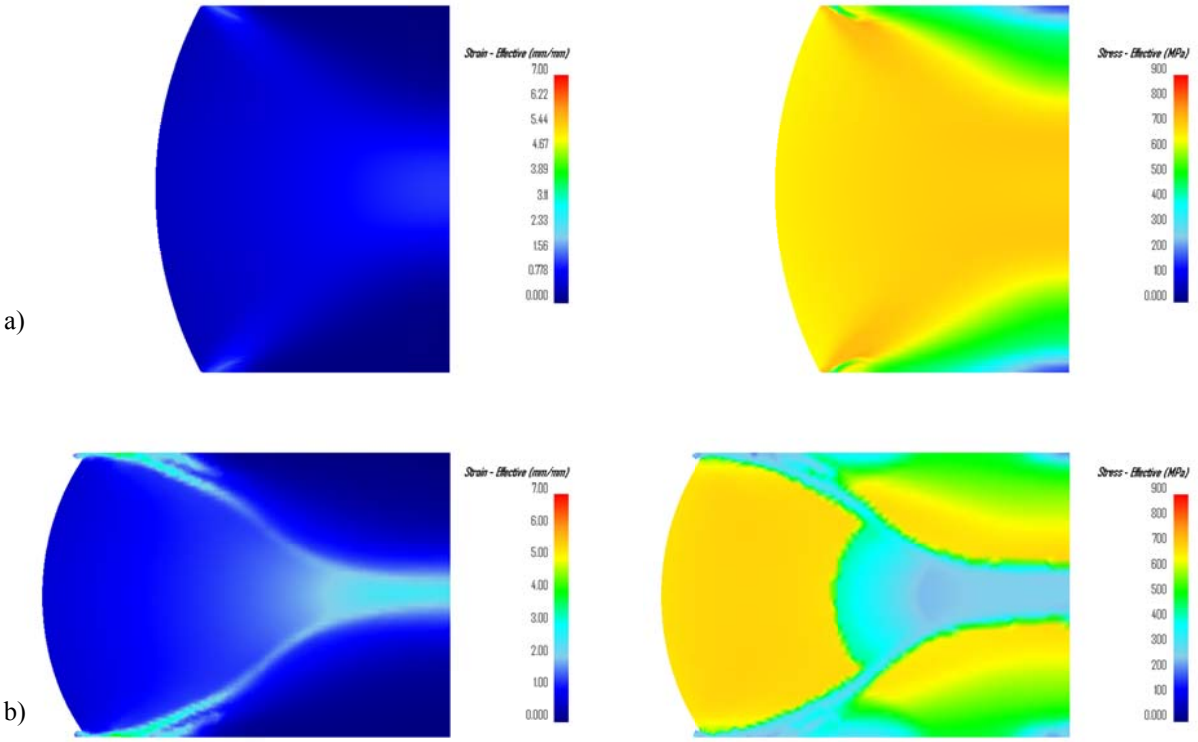

Figure 3-24: Effective strain and stress distribution in true strains of (a) 0.6 and (b) 1 with strain rate 10 s^{-1} and temperature 750 °C .

3.7 3D Material Modeling of Adiabatic Shear Instability

The description of the material behavior based on a function in which the yield stress is a function of strain, strain rate and temperature, was presented in the previous chapter. The main goal regarding the modeling of the adiabatic shear instability can be summarized in two phases: detecting of a maximum value for equivalent stress and degrading of flow stress after the according strain. Since increasing of the minimum element size in 3D simulation, the critical strain rate solely is not adequate for defining of the damage initiation or rather flow stress degradation. Hence, in this section, a critical strain rate is determined instead of the critical strain for the simple power low material behavior like Frost and Ashby [102] and then the approach is adopted for the Johnson-Cook material model.

The general condition for the flow instability is valid here, as mentioned, deformation instability begins, when:

$$\left(\frac{\partial \sigma_{eq}}{\partial \varepsilon}\right)_{T,\dot{\varepsilon}} d\varepsilon + \left(\frac{\partial \sigma_{eq}}{\partial T}\right)_{\varepsilon,\dot{\varepsilon}} dT + \left(\frac{\partial \sigma_{eq}}{\partial \dot{\varepsilon}}\right)_{T,\varepsilon} d\dot{\varepsilon} = 0 \qquad \textbf{Equation 3-29}$$

and with the assumption that the strain state does not change during adiabatic shear and the whole generated energy due the deformation converts into the heat:

$$\left(\frac{\partial \sigma_{eq}}{\partial \varepsilon}\right)_{T,\dot{\varepsilon}} = -\left(\frac{\partial \sigma_{eq}}{\partial T}\right)_{\varepsilon,\dot{\varepsilon}} \frac{\sigma_{eq}}{c_p} \qquad \textbf{Equation 3-30}$$

as the flow stress behavior defined as only function of work hardening (power law):

$$\sigma_{eq} = K\varepsilon^n \qquad \textbf{Equation 3-31}$$

then with derivation of the flow stress respect to the strain term, the corresponding critical strain regarding the maximum value of flow stress can be determined:

$$\varepsilon_c = \frac{-nc_p}{\left(\partial \sigma_{eq}/\partial T\right)_{\varepsilon,\dot{\varepsilon}}} \qquad \textbf{Equation 3-32}$$

Since the effect of temperature on the flow behavior of material is not considered in the power law material model, it is assumed that the $\left(\partial \sigma_y/\partial T\right)_{\varepsilon,\dot{\varepsilon}}$ term is a fraction of flow stress.

It was assumed that the whole deformation work converts into heat, it means that the strain rate is high enough and in these high strain rates, the time is not sufficient for the heat loss. For a better understanding, we limit our consideration only to the shear band as a control volume and try to find a critical strain rate whereby no heat goes out of this closed volume.

The general form of Fourier rule without an internal heat source for the constant thermo physical material properties can be written

$$\dot{q} = -\lambda \nabla T \qquad \textbf{Equation 3-33}$$

where $\dot{q}$ is heat flux density [W/m²] , ∇T is the gradient of temperature [K/m] and λ is the thermal conductivity [W/mK].

With one dimensional heat flow in the flat wall in one direction:

$$\dot{q} = -\lambda \frac{dT}{dX} \qquad \textbf{Equation 3-34}$$

with multiplying both sides of the above equation with according area (A_{sb}) can be achieved the heat flux ($\dot{Q}$, [W]):

$$\dot{Q} = -\lambda \frac{dT}{dX} A_{sb}$$ **Equation 3-35**

With rewriting and integration of above equation:

$$\dot{Q} \int_{x_1}^{x_2} dX = -\lambda A_{sb} \int_{T_1}^{T_2} dT$$ **Equation 3-36**

then, the heat flux can written:

$$\dot{Q} = -\lambda A_{sb} \frac{(T_2 - T_1)}{(X_2 - X_1)}$$ **Equation 3-37**

or with respect to one dimensional heat conduction through the according flat wall:

$$\dot{Q} = \frac{\lambda A_{sb}}{L_{sb}} (T_1 - T_2)$$ **Equation 3-38**

with consideration of the shear band, A_{sb} and L_{sb} can be replaced with the area and thickness of the shear band.

Now, considering the virtual heat loss, the heat balance equation for this shear control volume (V_{sb}) can be written as:

$$\rho V_{sb} c_p dT + \dot{Q} dt = V_{sb} \sigma_{eq} d\varepsilon$$ **Equation 3-39**

then, from Equation 3-38 and dividing both sides of the heat balance equation with dt , the term of $d\varepsilon/dt$ is substituted with strain rate ($\dot{\varepsilon}$):

$$\frac{dT}{dt} + \frac{\lambda A_{sb}}{L_{sb} c_p} (T_1 - T_2) = \sigma_{eq} \frac{\dot{\varepsilon}}{c_p}$$ **Equation 3-40**

with dividing again both sides with $\dot{\varepsilon}$, the heat balance equation can be rewritten:

$$\frac{dT}{d\varepsilon} + \frac{\lambda A_{sb}}{L_{sb} C_p \dot{\varepsilon}} (T_1 - T_2) = \frac{\sigma_{eq}}{c_p}$$ **Equation 3-41**

with rewriting of differential form of $dT/d\varepsilon$ term to a discrete one:

$$\frac{dT}{d\varepsilon} \cong \frac{T_1 - T_2}{\varepsilon_2 - \varepsilon_1} = \frac{T_1 - T_2}{\varepsilon_c}$$ **Equation 3-42**

Here, it is assumed that the difference between two strains is equal to the critical strain. This cannot be far from reality, because it is tried to get a strain rate in which the deformation instability begins which is the same as the initial strain to a critical strain. Thus:

$$\frac{1}{\varepsilon_c}(T_1 - T_2) + \frac{\lambda A_{sb}}{L_{sb} c_p \dot{\varepsilon}}(T_1 - T_2) = \frac{\sigma_{eq}}{c_p} \qquad \textbf{Equation 3-43}$$

Now, in order to satisfy the condition for beginning an adiabatic shear should be the conduction term much less than the first term of the left side. In this situation, the heat transfer into the outside of the control volume is hindered. Therefore:

$$\frac{\lambda A_{sb}}{L_{sb} c_p \dot{\varepsilon}}(T_1 - T_2) \ll \frac{1}{\varepsilon_c}(T_1 - T_2) \qquad \textbf{Equation 3-44}$$

Or

$$\dot{\varepsilon} \gg \varepsilon_c \frac{\lambda A_{sb}}{L_{sb} c_p} \qquad \textbf{Equation 3-45}$$

from which can be deduced that the minimum requested strain rate for beginning a shear instability is:

$$\dot{\varepsilon}_m = \frac{-\lambda A_{sb} n}{L_{sb}\left(\partial \sigma_{eq} / \partial T\right)_{\varepsilon, \dot{\varepsilon}}} \qquad \textbf{Equation 3-46}$$

As mentioned, the $\dot{\varepsilon}_m$ is an approximation of the lower limit of the critical strain rate. With considering heat conduction, the required strain rate for the setting of instability increases. With the consideration of the softening factor in a material model for the equivalent stress:

$$\sigma_{eq} = \sigma_{eq}(\varepsilon, \dot{\varepsilon}, T, D_c) \qquad \textbf{Equation 3-47}$$

and the Johnson-Cook material model is used for the describing of flow stress, it can be written like that:

$$\sigma_{eq} = (A + B\varepsilon^n)\left(1 + Cln\left(\frac{\dot{\varepsilon}}{\dot{\varepsilon}_0}\right)\right)\left(1 - \left(\frac{T - T_r}{T_m - T_r}\right)^m\right) D_c \qquad \textbf{Equation 3-48}$$

where D_c is a parameter for the material softening or rather the damage growth. This parameter can be defined in form of an exponential function with two control constants from section 3.3.4:

$$D_c = Exp(-a_1 \varepsilon^{b_1}) \qquad \textbf{Equation 3-49}$$

where a_a is equal to 0.25 and with b_1 equal to 2.5.

The numerical implementation of the shear instability routine is illustrated in Figure 3-25. The code is written in USRMTR subroutine in DEFORM 3D. First, the flow stress from the original Johnson-Cook model is calculated and then the critical area with the high strain rate is distinguished in order to decrease the number of calculations per step. For the elements with the strain rates higher than the critical value, the critical strain is calculated from Equation 3-21 numerically. If the according effective strain of the element is greater than the critical strain, the value of D_c is determined to define the degree of flow stress degradation or rather the material softening. In order to provide stability of simulations, a minimum value (greater than zero) for D_c has been chosen. This minimum value also plays a roll to coincide calculated forces with measured forces.

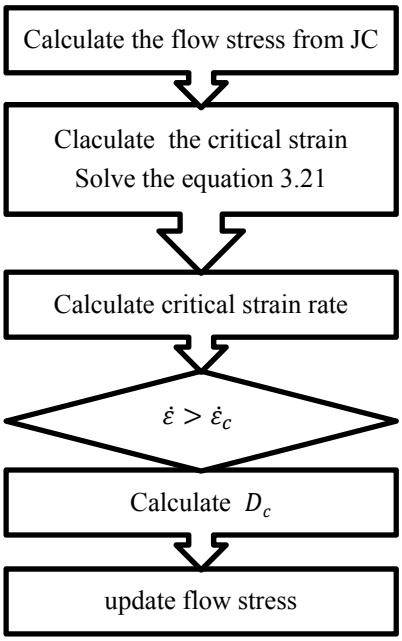

Figure 3-25: 3D shear instability approach.

3.8 3D Simulation results and Approach Validation

A 3D finite element model with 50000 tetrahedral elements was developed in commercial software Deform 3D. The work piece geometry refers to the original cylindrical specimen geometry (16 x 10 mm) with a constant temperature. The hybrid frictional condition with coulomb coefficient of 0.5 and shear constant of 0.9 was defined in the contact area between the work piece and the dies. The heat transfer coefficient between the work piece and dies is taken as constant value of 10 kW/m²K while the convection coefficient was assumed to be 20 W/m²K. The results of simulation using the above mentioned algorithms in 3D material modeling are illustrated in Figure 3-26.

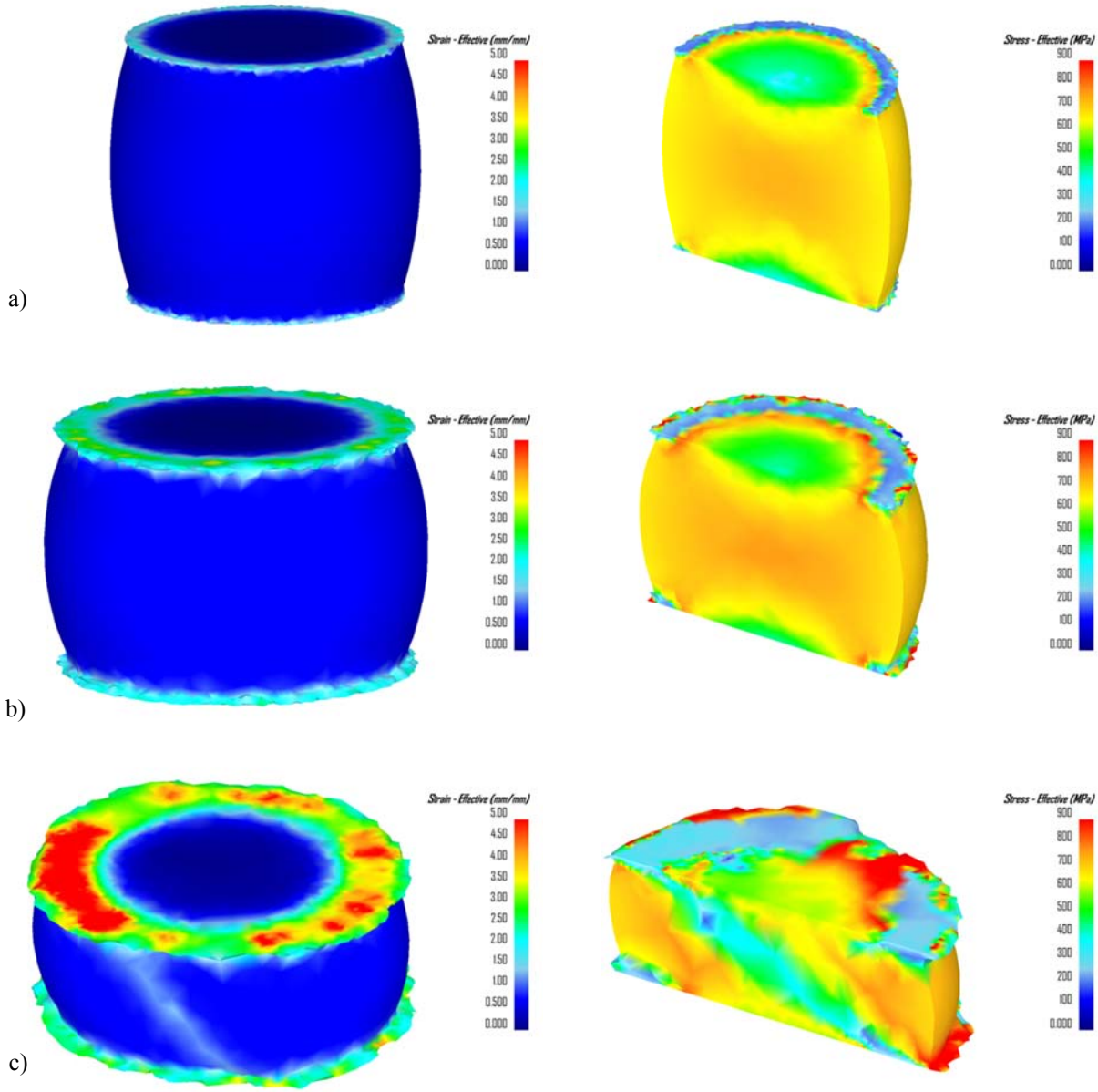

Figure 3-26: 3D presentation of effective strain and stress distribution in true strains of (a) 0.4 (b) 0.6 and (c) 1 with strain rate 1 s^{-1} and temperature 600 °C .

As can be observed, the strain localization until strain 0.6 is restricted only on the narrow rand. The remarkable strain localization has reported in the height of 6.49 mm (strain 0.9) which is corresponding to the failure. The results of 3D simulation are in accordance with 2D simulation. Furthermore, the calculated forces are in good agreement with measured forces from the Gleeble system. The maximum calculated force from the simulation is 110 kN in comparison with 103 kN in the experimental one.

Also, the material modeling approach was used to simulate a 3D chip formation in orthogonal machining with cutting velocity of 90 m/min, uncut chip thickness of 0.07 mm and tool rake face of 11 °. Figure 3-27 shows the morphology, the effective strain and temperature

distribution of the achieved chip. As can be seen in Figure 3-27.b and Figure 3-27.c, the strain and temperature localized as the strain rate achieved the critical strain rate. The comparison between the frequencies (distance between teeth) is also in the range of achieved experiments chips.

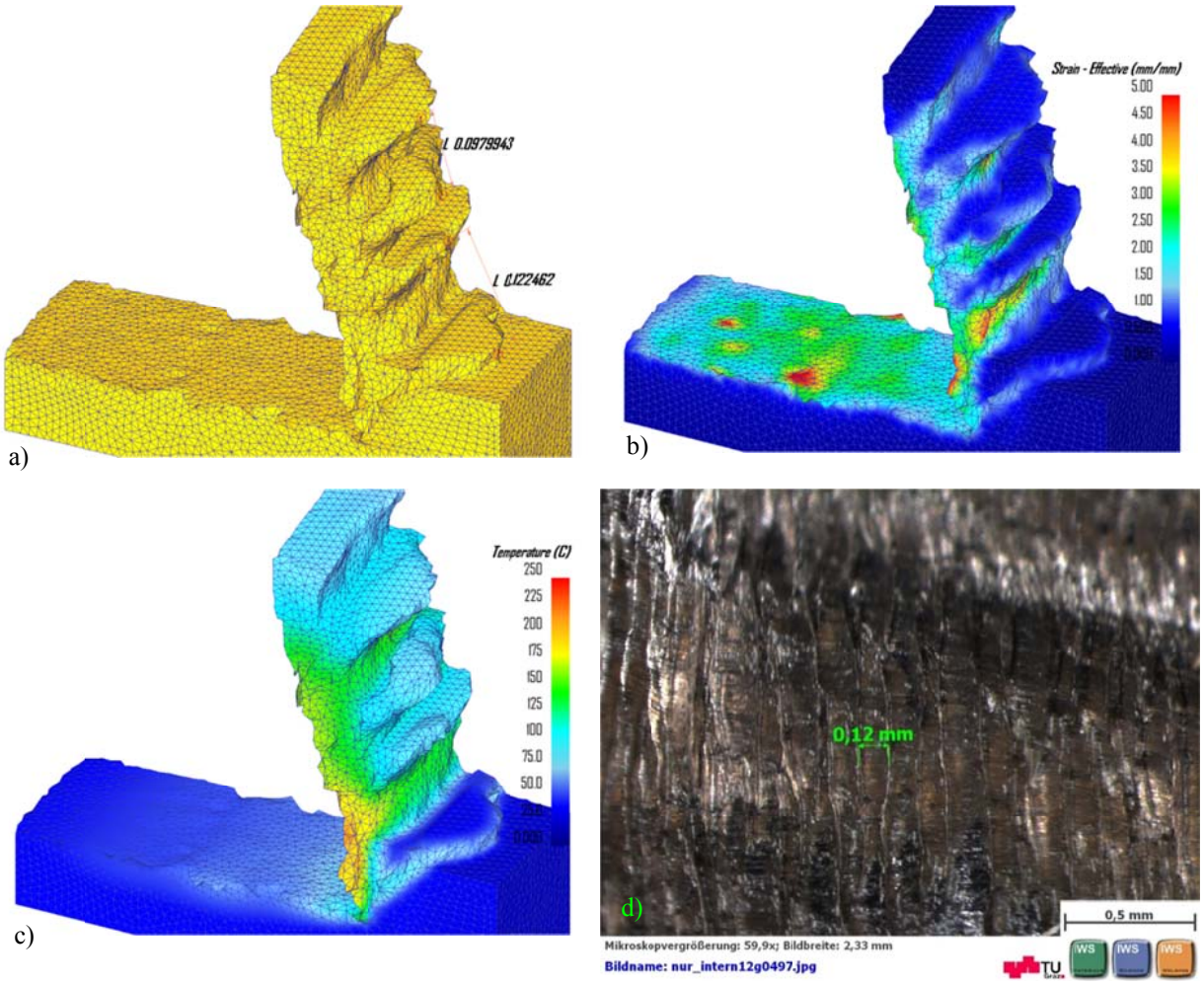

Figure 3-27: (a) 3D chip segmentation (b) localized effective strain (c) temperature distribution in the direction of maximum shear stress at a cutting velocity 90 m/min in comparison with (d) experimental achieved chip.

As it might be reflected, the numerical cost of the routine is still high; however, a critical strain is not calculated for all the elements under loading. This weakness caused the simulation stoppage which impedes the simulation investigations as a tool for the optimization and efficiency improving of the novel laser assisted milling process. However, the related routine is able to use the diverse material modeling research activities, where the adiabatic shear instability arouses interest.

From this point of view, another approach in modeling is utilized to decrease the numerical costs and enables to simulate the adiabatic shear effect on the macro scale where the minimum element size is relatively higher than the shear band thickness. The thicknesses of

shear bands are normally in the range of 0.01 up to 0.02 mm. From the other side, 3D simulation of the shear band requires at least 4 till 6 elements in these areas which is a very small element size essential for it.

Also here, the routine begins (Figure 3-28) with the determination of flow stress from the Johnson-Cook model and then calculation of the thermal softening rate from Equation 3-20, Equation 3-50 and substitute in Equation 3-46 by replacing the minimum element size instead of shear band thickness to separate the high strain rate of area. For the corresponding elements, the thermal softening coefficient (m) in the Johnson-Cook material model behaves as follows:

$$m = m_0 \exp(-a_2 T^{b_2}) \qquad \textbf{Equation 3-50}$$

where a_2 and b_2 are constants and m_0 is the initial thermal softening coefficient. The a_2 and b_2 were fixed with several machining testing with and without laser.

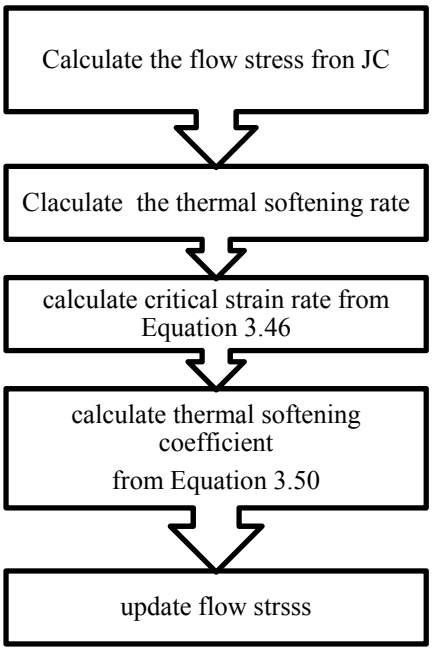

Figure 3-28: Nonlinear thermal softening (NTS) approach.

The thermal softening rate is accelerated indirectly with the falling thermal softening coefficient which satisfied the main deformation instability criterion: the adiabatic shear happens as the thermal softening rate is greater than the strain hardening rate.

Finally, it should be mentioned that using solely the nonlinear thermal softening approach does not suffice for chip segmentation studies, especially in 3D simulations. The introduced approach is appropriate and useful in the macro scale calculation of forces. With the observation of the force reduction in laser assisted experiments, it has been found that global

thermal softening is not linear and accelerated at a certain temperature. The other models such as original Johnson-Cook model and modified one in section 3.2.1 do not consider this effect which does not lead to exact prediction. The modified Johnson-Cook model (TANH) is compared and interpreted with the non-linear thermal softening approach (NTS) in the next chapter.

4 3D Simulation of Laser Assisted Milling

4.1 Modeling of the Laser Heat Source

One of the most important aspects in the efficiency of laser assisted milling is temperature management. The higher laser power and the resulting high temperature does not always mean the decrease of force reduction magnitude and tool life. The overheated work piece increases the potential of micro crack formation when it exceeds the thermal strength of the material in the finished part. Furthermore, hot machining increases the chip-tool interface temperature which may decrease surface integrity, tool life and finally machining productivity. Thus, in this Chapter, a 3D transient finite element model for the moving Gaussian laser heat source is developed to analyze the thermal gradients and thermal response of work piece material in laser-assisted milling. The suggested thermal model in this study is coupled with the removal of material and considers the temperature distribution inside the work piece due to localized laser heating. Moreover, it is useful to determine the heat affected zone (HAZ) in the work piece in relation to machining process parameters such as cutting velocity, feed rate from one side and the laser control parameters such as laser power, spot size, laser advancement and laser beam irradiation angle from other side. Coordination

between these factors provides a chance to achieve the maximum benefits of laser machining and prevents an unnecessary expanded heat affected zone.

Another step after developing an integrated and process parameter controllable thermal model is the determination of absorbed heat input portion in the material. The absorption coefficient is a physical material property which can be affected by many process-related parameters and surface quality. In present study, the depth of molten zone and the resulting microstructure changes is set as a benchmark to estimate the process depending absorption coefficient. Under different machining conditions, the laser power depth of molten zone was compared with the one calculated from simulation and the related absorption coefficients were detected.

In the following sections, the implementation of integrated moving laser heat source is presented first. Then, model validation is showed by varying the parameters of laser power and cutting speed. Finally, the validate model is used to optimize tool construction in terms of the laser advance and the laser spot size.

4.1.1 Transient 3D FEA Model

In order to analyze and determine temperature distribution in the work piece caused by laser irradiation, based on the general energy balance equation during metal forming [103], it can be written:

$$\lambda \nabla^2 T + \dot{W}_p - \rho c_p \dot{T} = 0$$

Equation 4-1

$\lambda \nabla^2 T$: heat transfer rate

$\dot{W}_p$: heat generation rate

$\rho c_p \dot{T}$: internal energy rate

where λ is thermal conductivity, $\nabla^2 T$ is the Laplace operator with respect to temperature (T), $\dot{W}_p$ is the heat generation rate due to deformation, ρ is the density, c_p is the heat capacity and $\dot{T}$ is the differentiation of temperature with respect to time.

Irrespective of elastic deformation, the generated heat due to deformation is:

$$\dot{W}_p = \beta \sigma_{eq} \dot{\varepsilon}$$

Equation 4-2

where β states the fraction of generated energy which is converted to heat, σ_{eq} is the effective stress and $\dot{\varepsilon}$ is the effective strain rate.

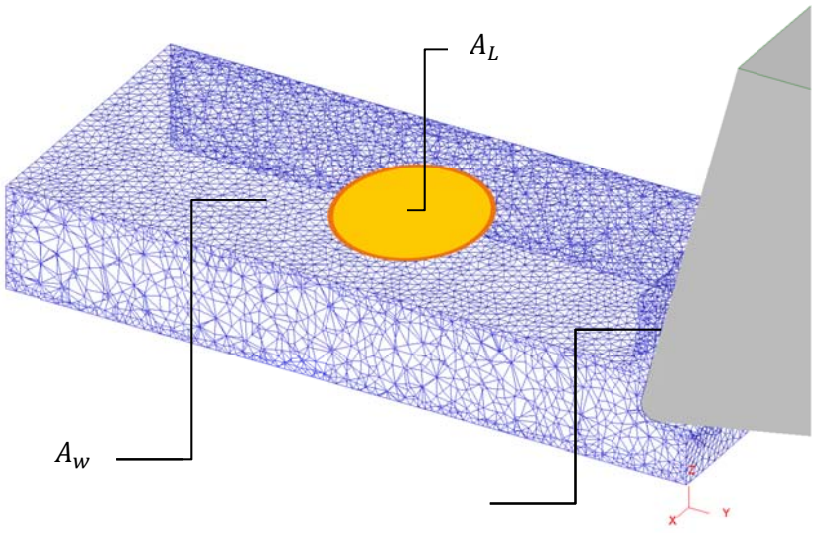

Figure 4-1: Defined boundary domain for modeling of laser heat source.

In the laser assisted machining, the heat flux comprising the input and output heat fluxes, it can be written by the following equation:

$$Q = \int_V \beta \sigma_{eq}\, \dot{\varepsilon} dV + \int_{A_w} \sigma\varepsilon(T_e^4 - T_s^4)\, dA_w + \int_{A_w} h(T_e - T_w)\, dA_w + \int_{A_L} h_L\,(T_e - T_L) dA_L + \int_{A_C} h_{int}(T_d - T_w)\, dA_C + \int_{A_C} q_f\, dA_C$$

Equation 4-3

$\int_V \beta \sigma_{eq}\, \dot{\varepsilon} dV$: generated heat due to machining (plastic deformation)

$\int_{A_w} \boldsymbol{\sigma\varepsilon}(T_e^4 - T_W^4)\, dA_w$: transferred heat due to radiation being over A_w

$\int_{A_w} h(T_e - T_w)\, dA_w$: transferred heat due to convection being over A_w

$\int_{A_L} h_L\,(T_{Le} - T_{sL}) dA_L$: transferred heat due to convection being over A_L

$\int_{A_C} h_{int}(T_t - T_w)\, dA_C$: transferred heat from the work piece to the die over the tool- work piece interface area A_C

$\int_{A_C} q_f\, dA_C$: generated heat due to friction

where the V is volume of the workpiece, the A_w is the work piece area (machined and not machined area except the laser spot surface and the tool-work piece contact area) which represents conventional and radiation heat transfer with the environment, A_C covers the contact area between chip and tool and $\boldsymbol{A_L}$ is the laser spot area (Figure 4-1).

h, h_{int}, h_L are the heat transfer coefficient between work piece-environment, work piece-tool and work piece-laser spot area, repectively. T_w, T_t, T_e , T_{Le}, T_{sL} are temperature of workpeice,

tool, enviroment, local enviroment and local surface, respectively. $\boldsymbol{\sigma}$ is the Stefan–Boltzmann constant and $\boldsymbol{\varepsilon}$ is emissivity.

As can be seen in Equation 4-3, the input heat flux from laser with integration over laser spot is defined as:

$$Q_L = A_L h_L (T_{Le} - T_{sL}) \qquad \textbf{Equation 4-4}$$

In the above equation if the local convection coefficient (h_L) approaches zero, T_{Le} gets significantly higher than the surface temperature where irradiated by laser beam (T_{AL}) which leads to:

$$T_{Le} - T_{sL} = \frac{I_L}{h_L} \cong T_{Le} \qquad \textbf{Equation 4-5}$$

Thus, in the surface region of direct laser input, the virtual environmental temperature can be calculated directly out of the laser power density (I), ($I_L = P_L/A_L$) divided by a very small value of the convection coefficient (e.g. 0.0001).

In the case of the moving laser heat source, the local coordination of the defined laser spot area (A_L) change with the laser beam. As the laser beam moves along its diameter, the temperature at laser spot reaches a steady value. Also, the position of the laser spot area can be updated with tool velocity in each moving direction.

The laser spot area (A_L) can be divided into many subdomains which makes it possible to define different beam configurations such as Gaussian or top hat laser power distribution.

4.1.2 Analytical Determination of Maximum Temperature at the Laser Spot

In this section an analytical exploration of the maximum temperature [104, 105] at the laser spot is attempted as the laser beam scans with a constant velocity. Then, the analytical result provides a comparison with the FEM calculated peak temperature.

The general form of Fourier's law for the constant thermo-physical material properties and without the internal heat source is expressed as:

$$\frac{\partial T}{\partial t} = a_d \nabla^2 T \qquad \textbf{Equation 4-6}$$

where a_d is thermal diffusivity.

The heat condition equation in one dimensional can be summarized in:

$$\frac{\partial T(z,t)}{\partial t} = a_d \frac{\partial^2 (T,t)}{\partial z^2} \qquad \textbf{Equation 4-7}$$

It assumed that the laser beam is irradiated normally on the surface. The laser power is distributed uniformly on the applied surface with a continuous wave mode as illustrated in Figure 4-2:

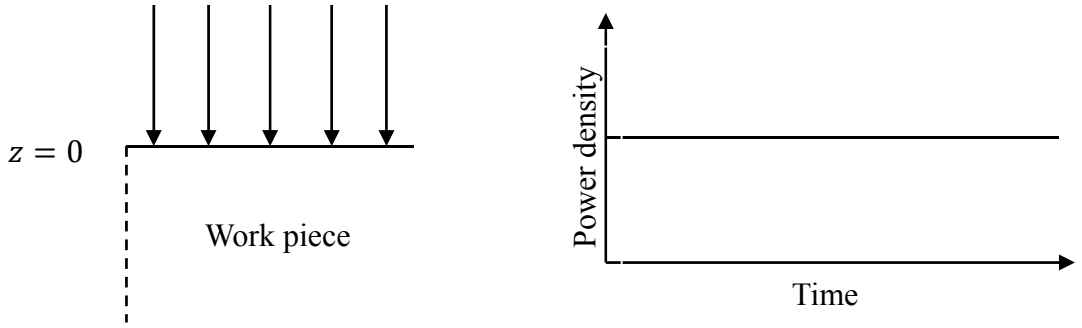

Figure 4-2: (a) Laser heat flux on the work piece surface, (b) continuous laser power mode [104].

A boundary condition of the second kind is applied at the surface

$$-\lambda \frac{\partial(0,t)}{\partial z} = \dot{q}_a \qquad \textbf{Equation 4-8}$$

where $\dot{q}_a$ is the absorbed laser power density [W/m²] which is a portion of irradiated laser power density (I_L):

$$\dot{q}_a = A_m I_L \qquad \textbf{Equation 4-9}$$

where A_m is absorption coefficient.

For the uniform beam profile the laser power density is defined as:

$$I_L = \frac{P_L}{\pi {r_0}^2} \qquad \textbf{Equation 4-10}$$

where r_0 is the radius of the laser beam.

With the consideration of boundary condition in Equation 4-8, temperature evolution during heating can be calculated [104] with:

$$\Delta T(z,t) = \frac{\dot{q}_a}{\lambda}(4a_d t)^{1/2}\left[1 - erf\left(\frac{z}{(4a_d t)^{1/2}}\right)\right] \qquad \textbf{Equation 4-11}$$

where erf is the error function:

$$\mathrm{erf}(z) = \frac{2}{\sqrt{\pi}} \int_0^z e^{-t^2} dt \qquad \textbf{Equation 4-12}$$

The surface temperature can be obtained when setting z equal to zero ($z = 0$) in Equation 4-11. Consequently, the resulting surface temperature is:

$$\Delta T(0,t) = \frac{\dot{q}_a}{\lambda} \left(\frac{4 a_d t}{\pi} \right)^{1/2} \qquad \textbf{Equation 4-13}$$

In case of the laser beam moving on the surface, as shown in Figure 4-3, the surface temperature reaches a maximum value with the laser beam moving over its diameter. Then, the interaction time (t_i) [59] can be defined:

$$t_i = \frac{2 r_0}{V_c} \qquad \textbf{Equation 4-14}$$

where V_c is laser beam scan velocity.

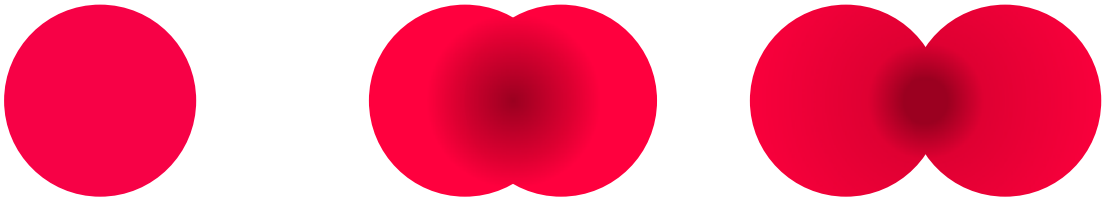

Figure 4-3: Reaching a maximum temperature with moving of the laser beam over its diameter.

4.1.3 Model development using Finite Element Method

Before discussing laser thermal modeling in the machining process in this section, a simple finite element model was developed to compare the above analytical result with the FEM calculated one. In this simulation, thermo-physical material properties were defined constant and the global heat convection coefficient with the environment (at surface A_w) was neglected.

The heat source moves with a constant velocity along Y direction on the XY surface. The laser heat flux is distributed over the whole laser spot surface uniformly. The specimen geometry investigated in the present analysis is a 4 mm × 2 mm × 0.5 mm with a fine mesh of 0.03 mm. The input data for simulation are listed in Table 4-1.

Figure 4-4 shows a similar temperature development as Figure 4-3 to achieve a maximum temperature.

Table 4-1: Simulation input data.

Used data in simulation and analytical solution	Value
Thermal conduction [W/m K]	17.6
Heat capacity [J/Kg K]	668
Density [Kg/m³]	4302
Laser power [W]	1000, 1500
Laser spot size [mm]	1, 1.5
Laser scanning velocity [m/min]	50,100,150, 200

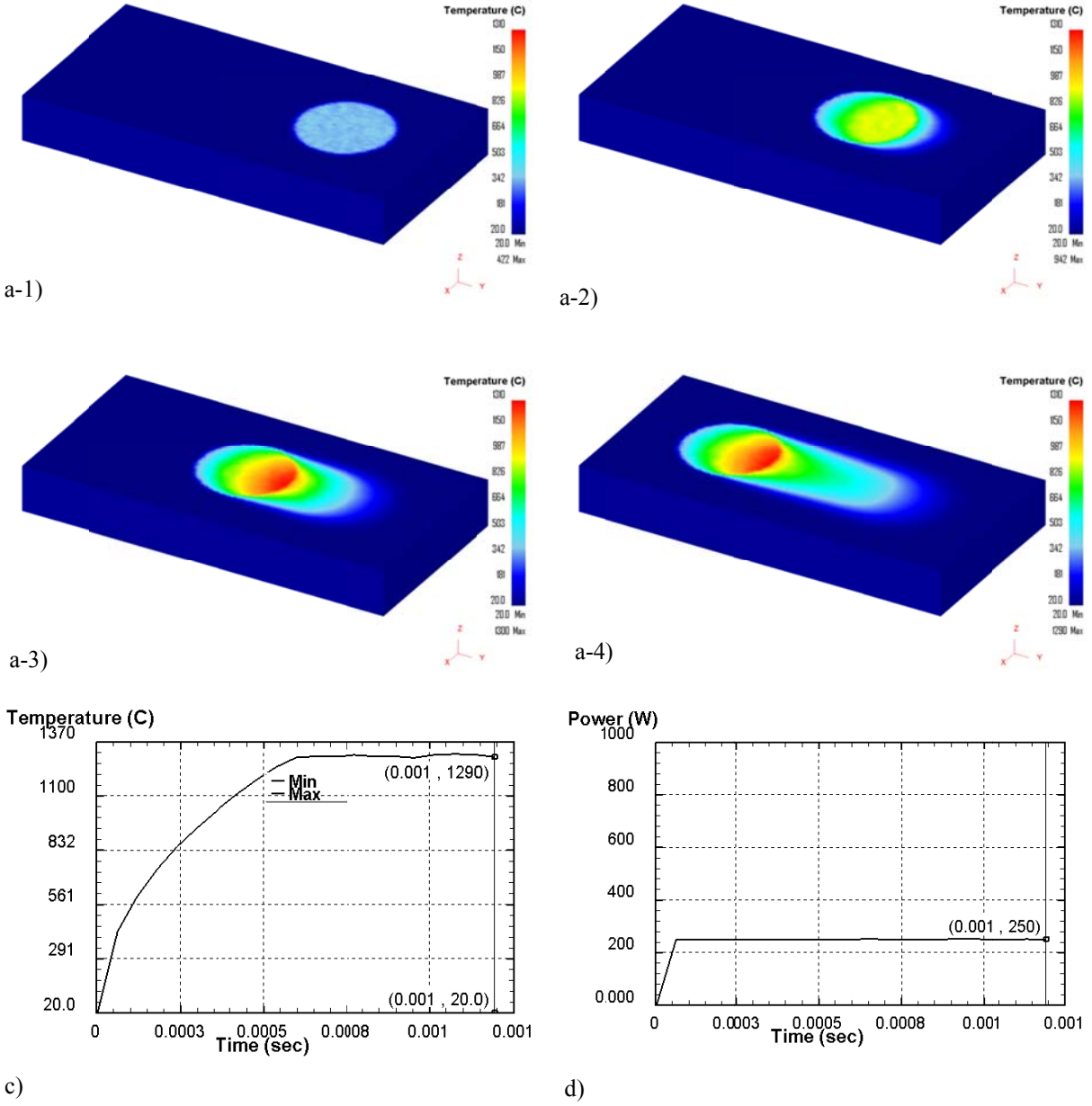

Figure 4-4: (a) Implemented moving thermal model in simple 3 D simulation in four stages, (b) reaching a steady maximum temperature, (c) inputted laser power.

The results of temperature peak at diverse laser scan velocities for two laser powers of 1000 and 1500 W with the same condition for both methods are represented in Figure 4-5.a and Figure 4-5.b. The analytically calculated peak temperatures validate the simulation results with a very good agreement. Both results show that with increasing laser scan velocity, the peak temperature decreases.

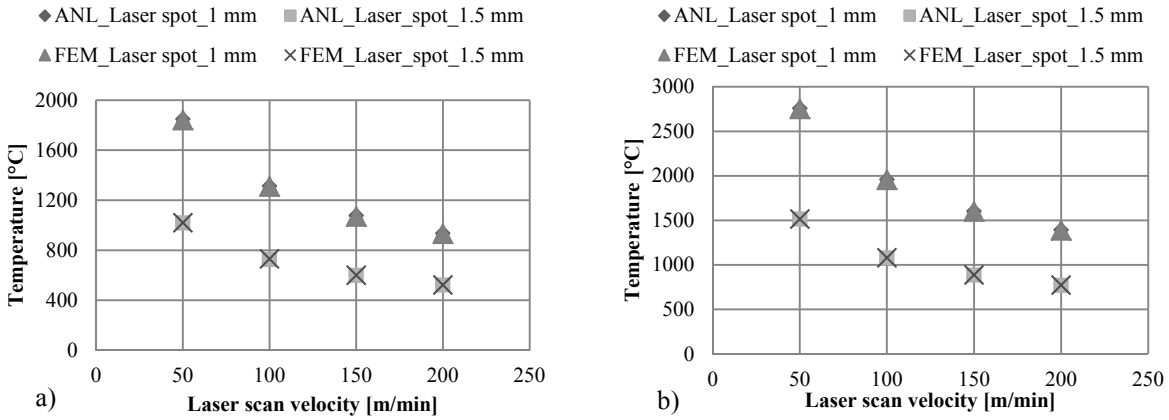

Figure 4-5: Comparison between simulated and analytically calculated results for (a) laser power 1000 W and (b) 1500 W.

4.1.4 Modeling of Incident Angle

Fresnel's [64] equations show that the absorptivity of an electromagnetic wave depends on the state of polarization, angle of incidence and optical constants:

$$A_p = \frac{4\boldsymbol{n}\cos\theta}{(\boldsymbol{n}^2 + \boldsymbol{k}^2)\ \cos^2\theta + 2n\ \cos\theta + 1} \qquad \textbf{Equation 4-15}$$

$$A_s = \frac{4\boldsymbol{n}\cos\theta}{\boldsymbol{n}^2 + \boldsymbol{k}^2 + \cos^2\theta + 2\boldsymbol{n}\ \cos\theta} \qquad \textbf{Equation 4-16}$$

$$A_m = \frac{A_p + A_s}{2} \qquad \textbf{Equation 4-17}$$

where the A_s is the absorptivity of the perpendicular polarized ray, A_p is the absorptivity of the parallel polarized ray, $\boldsymbol{n}$ (refraction coefficient) and $\boldsymbol{k}$ (extinction coefficient which is the imaginary part of the complex index of refraction) are optical constants depending on temperature and wavelength. The incidence angle (θ) is defined as the angle between the laser beam vector and the normal vector of the considered surface. A_m is defined as the absorption of circular polarization which is determined from the arithmetic mean value of the perpendicular and parallel components.

Figure 4-6.a shows an example of absorption as a function of polarization and angle of incidence for Titanium at 1.06 µm with optical constants $\boldsymbol{n} = 3.39522$ and $\boldsymbol{k} = 3.3375$. As can be seen, the absorptivity of the parallel polarized ray increases with incidence angle and takes a maximum of 80°. In contrast, the absorptivity of the perpendicular polarized ray decreases the incidence angle is increased.

In order to consider the effect of the incidence angle in finite element modeling, we have to equalize the resulting elliptical cross section of beam ($A_{ellipse}$) an interface with the circular cross section (A_{circle}) in case of normal incidence (Figure 4-6.b). For this purpose, a cross section factor (α_A) is defined from the division of two areas:

$$\alpha_A = \frac{A_{ellipse}}{A_{circle}} = \cos\theta \qquad \textbf{Equation 4-18}$$

It means that the laser power density which is used for simulations is multiplied with the cross section factor to consider the proposed angle of incidence.

Figure 4-7 illustrates the achieved temperature field and absorbed power for the incidence angles of 0, 30 and 60° in the case of Titanium (Ti). The laser power is assumed at 1000 W which moves along the Y direction with a scanning velocity of 100 m/min. The absorbed portion of power follows the absorptivity of the parallel polarized laser as achieved from Fresnel's equation (Figure 4-6.a). The results of simulation show that the developed heat source model is also functional for different angles of laser incidence. As expected, the absorbed laser power increases with the angle of incidence. The absorption coefficient for incident angle of 0, 30 and 60° are 0.447, 0.498 and 0.673 for the parallel polarized beam, respectively. Since increasing the incident angles, the laser power density decreases and the maximum temperature is approximately equal for three incident angles. However, the heat affected area enlarges itself with the incident angle which is useful in laser material processing.

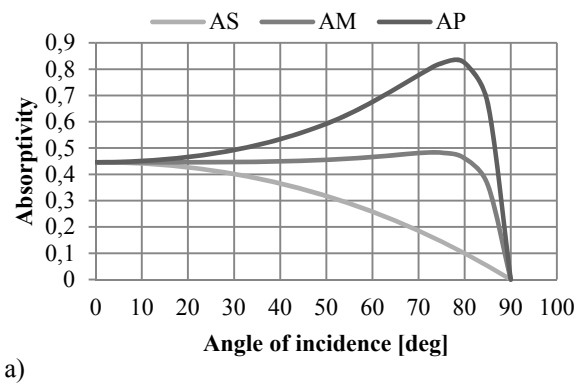

a)

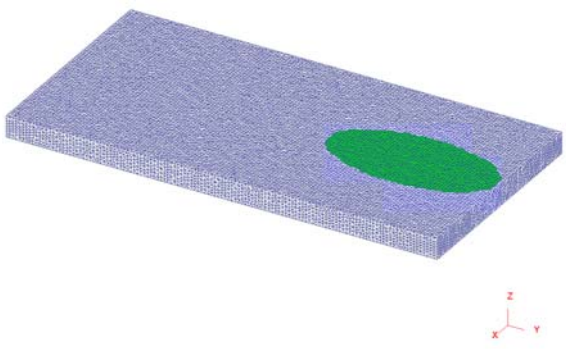

b)

Figure 4-6: Three absorption coefficients depending on the angle of incidence, (b) elliptical cross section of beam.

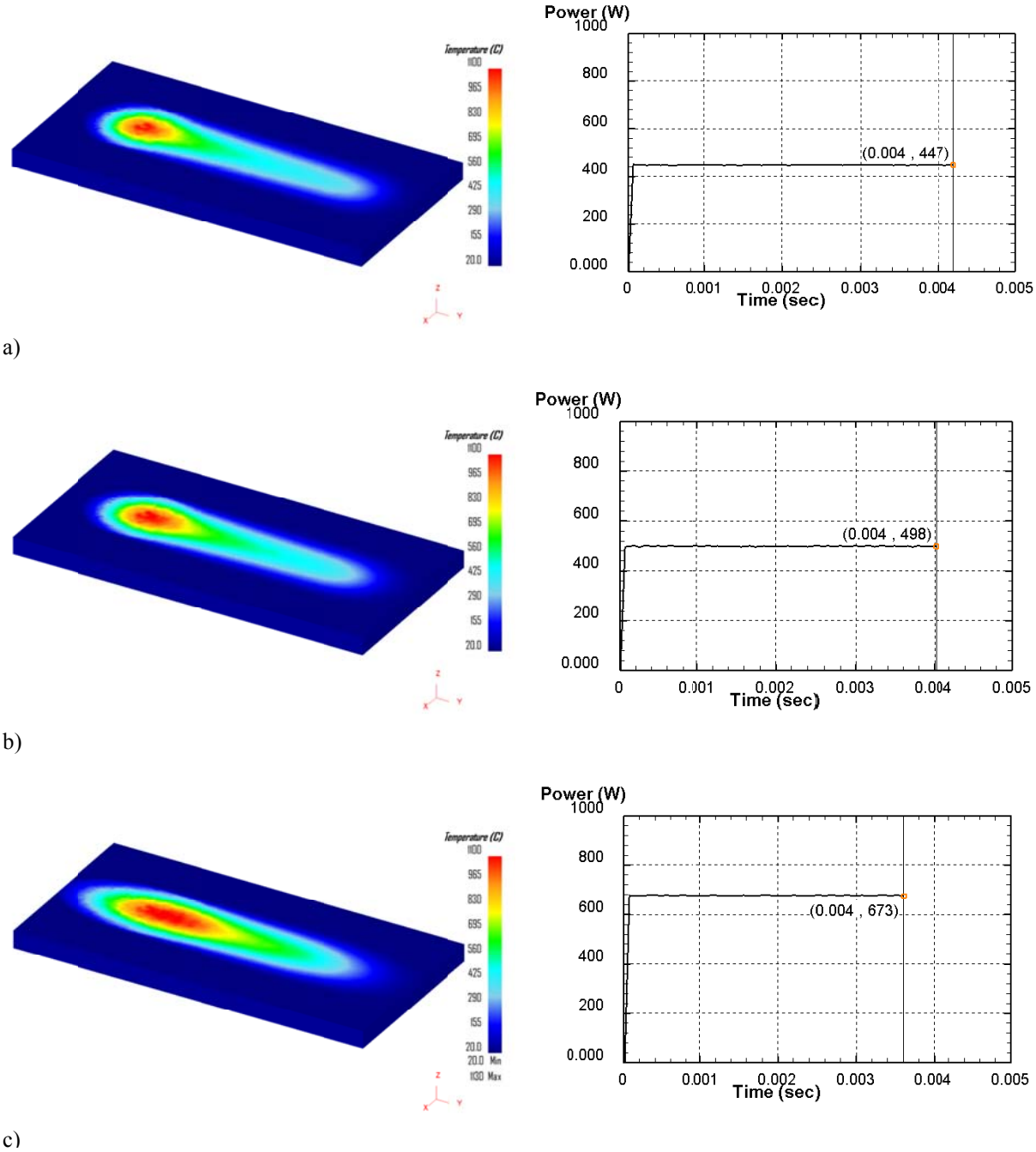

Figure 4-7: Implemented 3D moving laser heat source according the angle of incidence for (a) 0°, (b) 30° and (c) 60° for the parallel polarized beam.

4.1.5 Determination of Absorbed Laser Power

The absorption coefficient is the fraction of power absorbed by the work piece relative to the incident power. Apart from laser characterization, several process aspects affect the absorbed laser power. It should be mentioned that in the present tool system the laser beam is irradiated on the machined surface which exposes a particular surface brightness (absence of oxide layer) and surface roughness. Generally, the absorptivity of metals increases with the surface roughness and existence of the oxide layer. D. Bergstrom [106] showed that the surface

roughness causes multiple reflections and a larger incidence angle. Increasing the absorptivity result of the oxide layer can be justified by the multiple reflections.

Because of the complexity of the process, the precise online measurement of temperature on the cutting surface is not possible. Hence, in order to establish the absorbed laser power in this work, the depth of molten zone and the resulting microstructure changes at different laser powers was implemented. With reference to the calculated temperature field from the FEM simulations, the absorption coefficient in the laser assisted milling can be detected.

4.1.5.1 Experimental Setup

The following measurements were carried out in the laboratory of Fraunhofer Institute for Production Technology IPT in Aachen. The laser used as the radiation source was an Yb: YAG laser with a wavelength 1070 nm. Tests were conducted on a Titanium alloy (Ti6Al4V) with six laser powers (893, 1071, 1250, 1428, 1607 and 1758 W) with a moving speeds of 25 m/min. In order to reproduce the real machined surface, first, the machining was carried out to prepare the surface condition, then, the work piece was irradiated only once without the tool engagement. In comparison to the real situations, only probable variation in thermo-physical properties of work piece material due to heat removal by chip and heat generation by friction was not considered. The experimental set up and an optical image of the cutting surface after laser scanning is shown in Figure 4-8. For each test, a metallographic analysis of the section was performed to measure the depth of the molten zone and the expected microstructure changes.

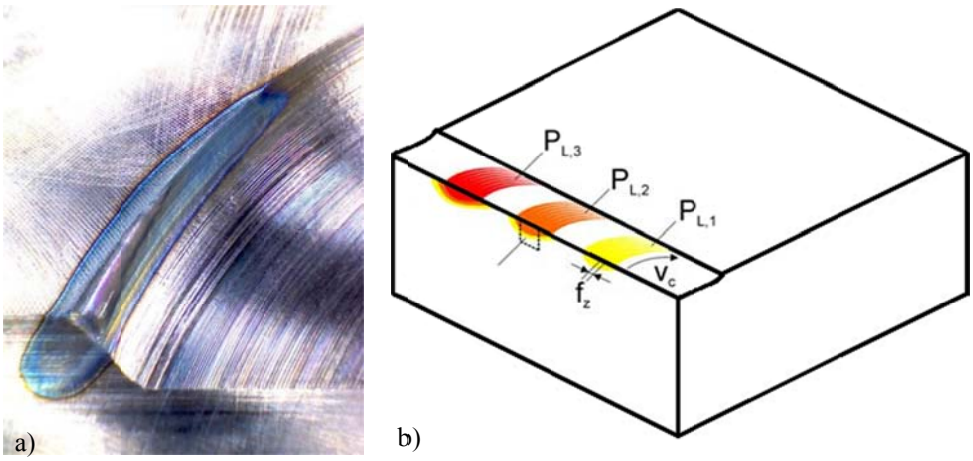

Figure 4-8: (a) Subjected surface with laser beam, (b) experimental set-up [70].

4.1.6 Comparison between the Experimental and Simulation Results

Figure 4-9.a shows the as-received α+β-microstructure of Ti-6Al-4V work piece material. As can be seen, the lamellar α-phase (hcp) is surrounded with the dark narrow β-phase (bcc). The phase diagram of Ti-6Al-4V is illustrated at the left side of Figure 4-9.b. At a temperature

above 995 °C (β- transus-temperature) the whole α-phase transforms into the β-phase. It should be mentioned that the reference temperature of 995 °C is valid for slow heating rate. With rapid cooling from temperatures above of β- transus-temperature (1050 °C) the β-phase transforms into the needle-shaped martensitic microstructure, as it is shown in Figure 4-10.a. At temperatures below the martensitic temperature (MS: 800-850 °C) more martensitic transformation does not take place.

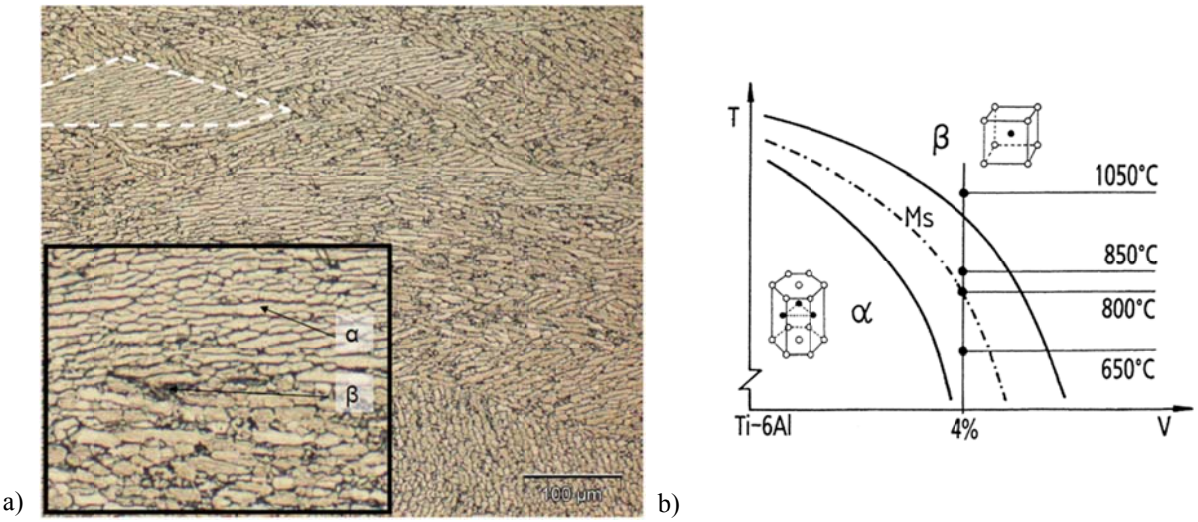

a) b)

Figure 4-9: (a) As-received α+β-microstructure of Ti-6Al-4V, (b) phase diagram of Ti-6Al-4V [70].

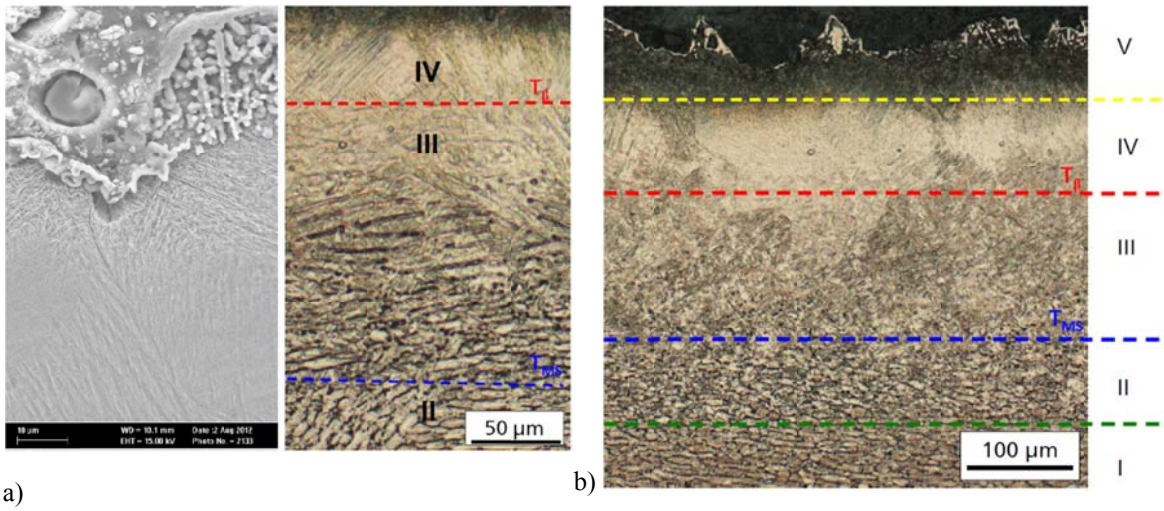

a) b)

Figure 4-10: (a) SEM and metallographic observation of needle-shaped martensitic microstructure (b) five resulting microstructure domains [70].

Figure 4-10.b shows five resulting microstructure domains as the work piece is undergoing a laser power of 1607 W: (I) initial microstructure (α+β), (II) no martensitic transformation but β transformation from α, (III) partial martensitic transformation, (IV) complete martensitic transformation, (V) oxide layer and white surface layer (as a result of surface melting).

Figure 4-11 presents the energy dispersive X-ray analysis (EDX) of white surface layer in two different points near the white surface. The chemical composition of the white layer verifies that the Titanium and alloying elements are not more in a solid solution. It means that the white layer forms on the surface due to a selective solidification procedure (segregation).

a)

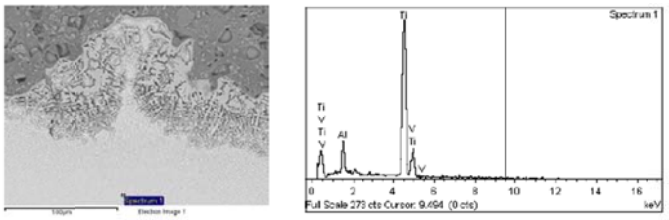

Element	Weight %
Al	6.86
Ti	87.76
V	5.37

b)

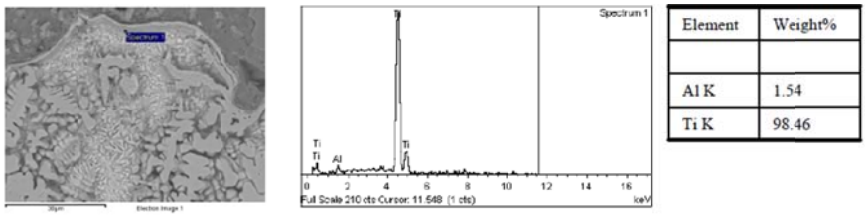

Element	Weight%
Al K	1.54
Ti K	98.46

Figure 4-11: EDX analysis of white surface layer where Ti is (a) in solid solution, (b) not in solid solution [70].

In order to compare the simulation result and experimental values, depth of melted zone and complete martensitic transformation zone below the subjected surface are attributed as a validation tool. The histograms in Figure 4-12.a and Figure 4-12.b show the comparison between the experimental results achieved. As it is observed, an absorption coefficient of 0.23 represents good correlation for a low laser powers (893, 1071, 1250, 1428) however, the melted area is deeper for a higher laser powers (1607, 1785 W). The absorption coefficient in the order of 0.3 is more acceptable. In general, the absorption coefficient does not depend on the laser power. However, by increasing the laser power, the surface temperature may exceed the melting temperature of alloy. Laser power densities of more than 10^5 Wcm^{-2} in most engineering metals lead to a surface melting [104, 107]. Some research works [106, 107] have informed that the absorption coefficient of metals increases with temperature in a light linear manner ($A_m(T) = A_{m0} + A_{mf}T$). At the melting point, the alloy state consists of a solid and liquid phase with insoluble alloying elements and consequently different optical constants. The ongoing melting phenomena simultaneously increase the number of conduction electrons and the metal density while the dc conductivity (unidirectional flow of electric charge) decreases. The absorptivity enhancement at the melting point is reported even until 200 % at the melting threshold [108].

In order to consider the effect of temperature on the absorptivity in the simulations of laser assisted machining the absorbed fraction of laser power optimized with the corresponding laser power. The suggested value of absorption coefficient for the range of power used in this

work is listed in Table 4-2. The prediction errors, according to complete martensitic transformation at the laser power 1785 W, may be attributed to precisely distinguish between complete and partial transformed martensitic domains.

Table 4-2: Absorption ratios

Power [W]	893	1071	1250	1428	1607	1758
Absorption Coefficient	0.22	0.22	0.22	0.26	0.27	0.27

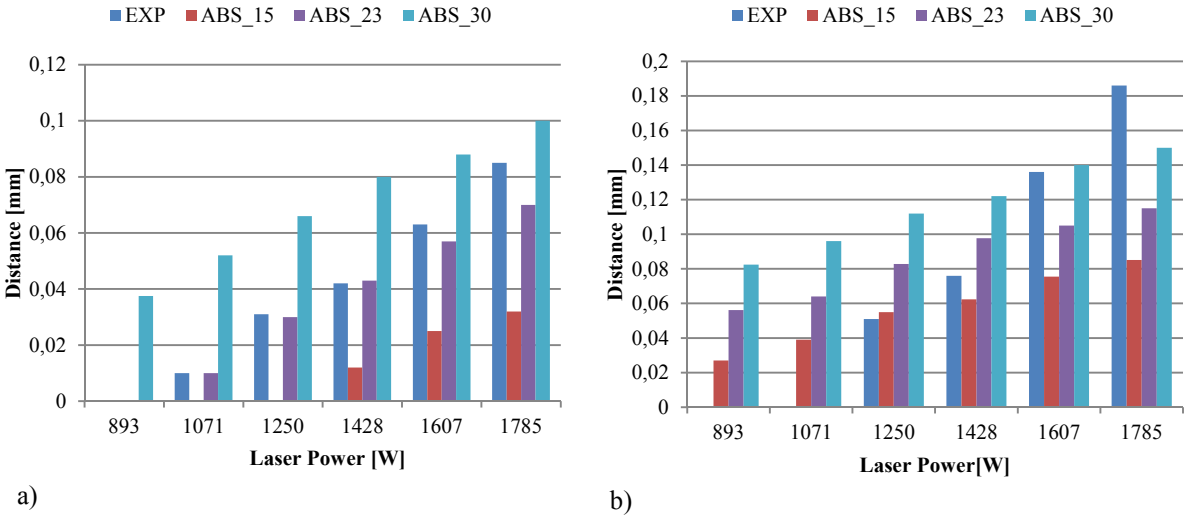

Figure 4-12: (a) Comparison between the molten depth and (b) completely transformed martensitic microstructure with assumed absorption coefficients (ABS) in simulations.

Figure 4-13 compares the resulting temperature distribution according to the absorption ratio of 0.23 for three laser powers. The melting area with the red scalar can be distinguished. As mentioned, in absence of the melting zone, the results show a very good agreement. The histogram in Figure 4-14.a illustrates the comparison between the partially transformed martensitic zones with the three absorption ratios. The relative difference between results at higher laser powers can be justified with the dwell time. The Figure 4-14.b shows the achieved zone with the 0.06 s dwell time after passing the laser (laser power 1758 W with an absorption coefficient of 0.27) which the according zone reaches 0.3 mm, which is very close to the experimented one. Figure 4-15 finally shows the implemented thermal model in laser assisted side milling, where the thermal model and milling process are fully integrated. The laser power decreases with the rotation angle as it calculated in section 2.4 . As it can be seen, the maximum temperature of 1280 °C decreases to 753 °C, as the laser spot has already rotated half-path. The model was used frequently and successfully in terms of the entire process of optimization.

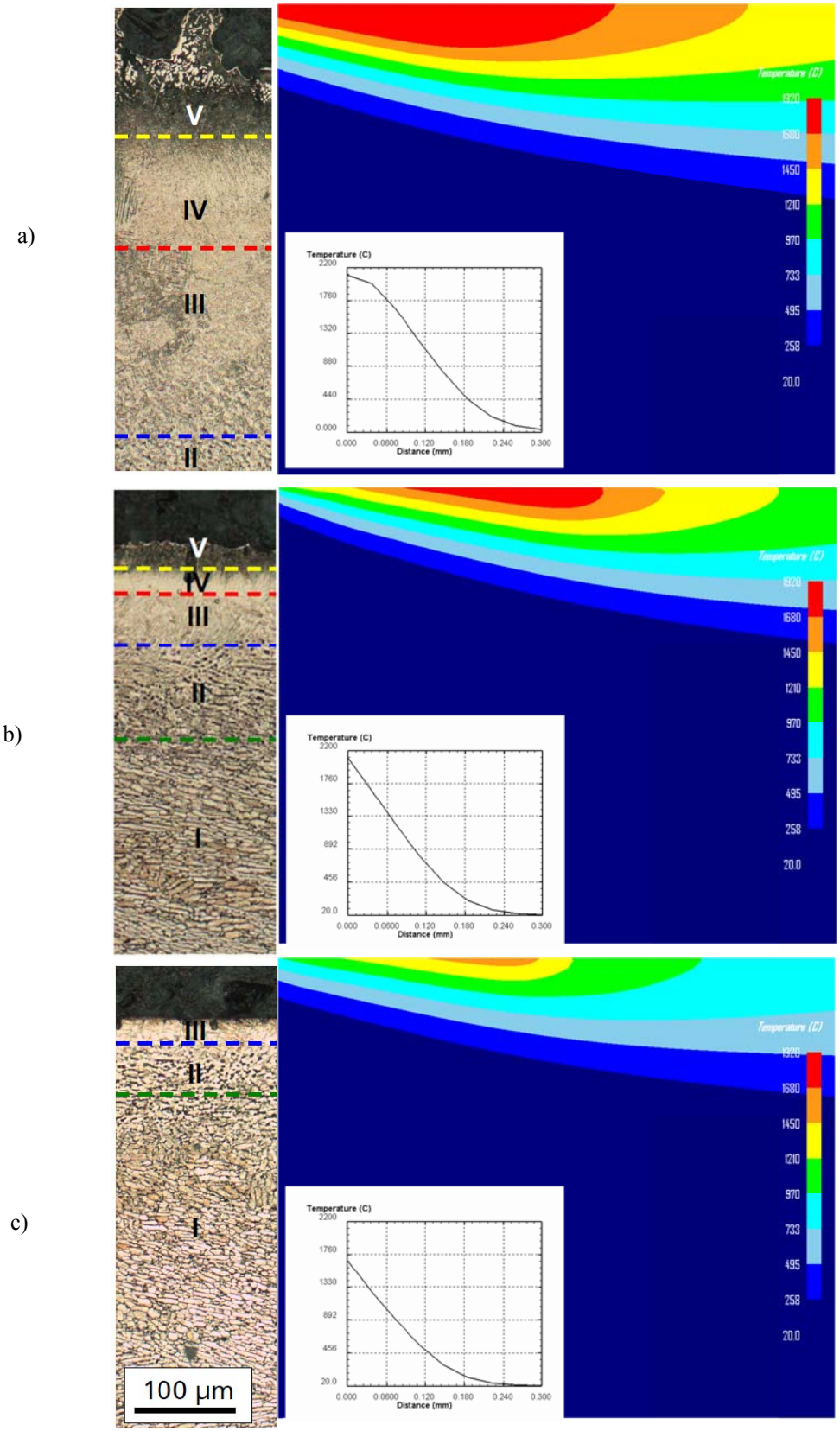

Figure 4-13: Comparison between temperature profile in simulations with attributed domains in experimental investigations at laser powers (a) 1758, (b) 1250 and (c) 893W with absorption coefficient 0.23.

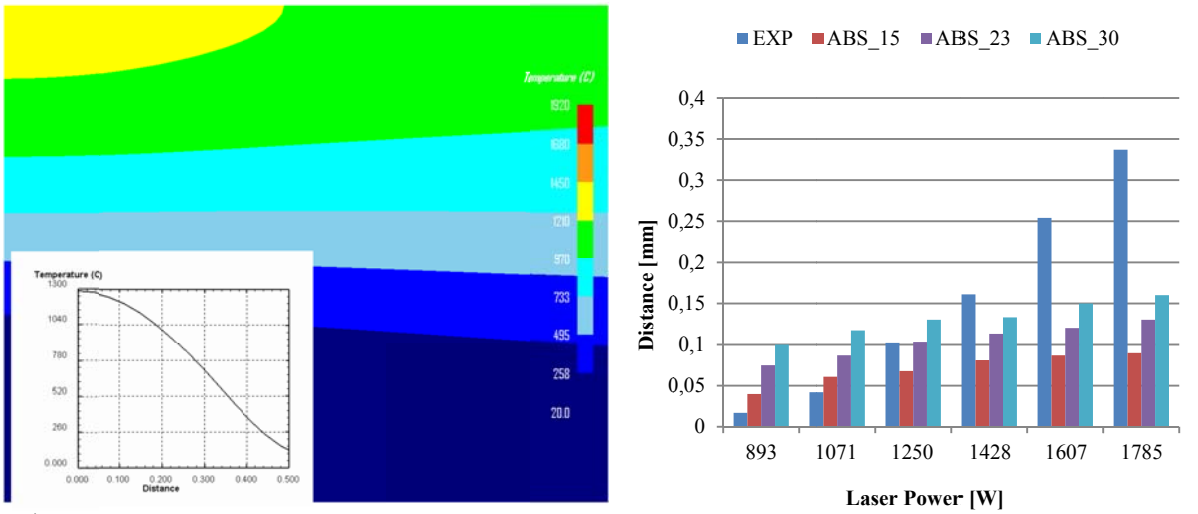

a) b)

Figure 4-14: (a) Comparison between depth of partially transformed martensitic microstructure with assumed absorption coefficients in simulations, (b) temperature distribution at laser powers 1758 W with absorption coefficient (ABS) 0.27 after dwell time.

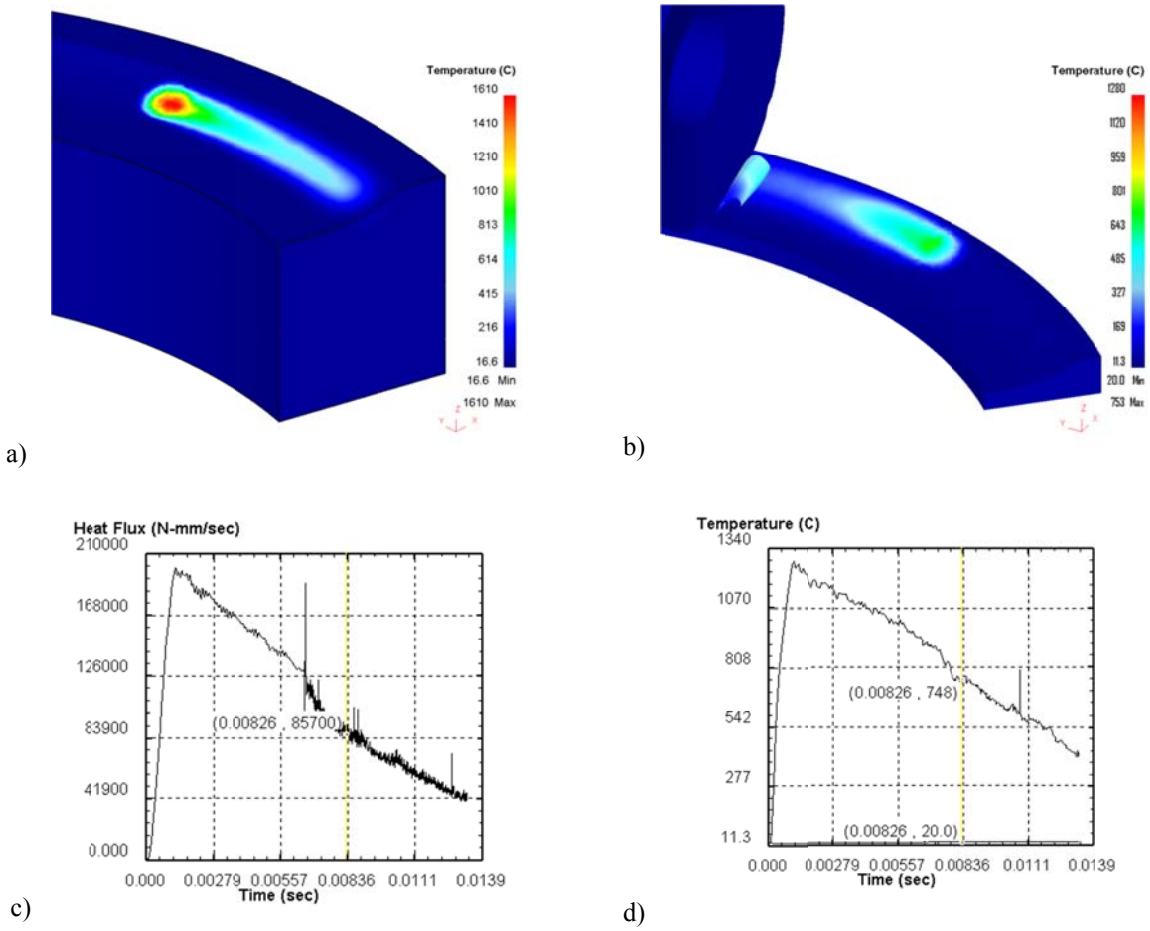

a) b) c) d)

Figure 4-15: (a) 3D rotating laser heat source (Laser power with Gaussian distribution: 1000 W, angular velocity: 70 rad/s, feed velocity: 0.77 mm/s) (b) integrated laser heat source with machining process (time dependent laser power) (c) heat flux variation during one revolution (d) maximum temperature at the laser spot [71].

4.2 Modeling of Contact Area

The tool-chip interface contact area in the machining process can be affected by the chip formation, cutting forces and tool wear. But the tool-chip interface in terms of friction and heat transfer behaviors, is not yet fully investigated from the point of view modeling. In the following sections, two aspects of contact (mechanical and thermal) are presented.

4.2.1 Frictional Behavior at Tool-Chip Interface

Frictional conditions at the interface tool-chip are difficult to determine because they are influenced by several factors such as the sliding velocity, local contact pressure, temperature and the tool and work piece material behavior in the cutting state. First, the friction coefficient in the modeling of the machining process influences the cutting temperature and secondary shear zone. Afterwards, it upsets the tool wear, the formation of built-up edges and the morphology of the achieved chip. Therefore, it is necessary to understand the mechanism of friction between the tool and the chip in order to estimate correctly the above mentioned appearance in the machining process. In the literature, there are several friction laws and models which allow for determining the tangential component of the stress vector in the tool-chip interface. The friction stress is always opposite to the sliding direction. The ratio between the stress and the contact pressure is represented by a coefficient, called coefficient of friction, often denoted μ. This is usually considered constant, but in reality it depends on several parameters such as the contact pressure, the rate of slip, the average temperature, the roughness of the contact surfaces, etc. However, the exact quantitative interrelation is still unclear. Model friction Zorev is among the most commonly used machining models to represent the nature of the contact between the tool and the chip within the sticking-sliding region aspects. Based on the Zorev's model [98], distribution of compressive and shear stress at the interface tool/chip are used by many researchers. Zorev states that the compressive stress (normal stress) is high at the cutting edge and becomes zero as the chip miss its contact with the tool while the shear stress (tangential stress) profile takes a more stable run along the rake face and then goes into zero at the end of the contact area (Figure 4-16). The friction model of Zorev is used on the rack face of sharp tools. Another friction assumption based on the round edge tool is developed by Ulutan [109]. In this model, the contact areas between the tool and work piece are separated into three regions of rake face, round face and clearance face. The friction behavior similar to the Zorev model governs on the rake face, where both sliding and sticking conditions are expected. The pure sticking condition is assumed along the tool curvature, which means that in these areas the tool and work piece are completely in contact. Furthermore, the clearance face presents only sliding behavior regarding to its contact with the workpiece. In current simulations on the rake face, the friction behavior follows a sliding-sticking condition. On the tool (insert) round face a full sticking condition (shear

friction stress is equal to equivalent shear chip flow stress) while on the clearance angle the sliding condition.

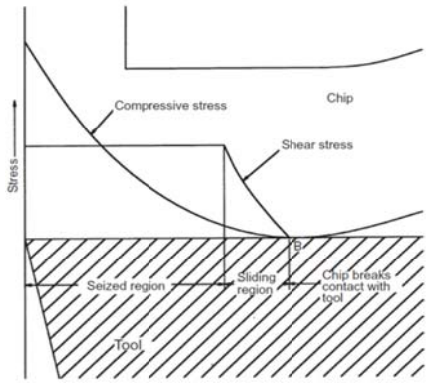

Figure 4-16: The stress distributions on the tool face according to Zorev [98].

4.2.2 Heat Transfer Condition between Tool and Chip

In the machining process, dissipated mechanical energy at the primary shear zone, secondary zone and the interface shear friction converts to heat and is transferred into tool, chip and work piece. This energy dissipation is caused by raising the temperature in the tool. Temperature levels often reach several hundred degrees in a machining process. To determine the level and distribution of temperature, several analytical and thermal models have been developed. The heat transfer coefficient at the tool-workpiece interface determines the portion of heat which transfers into the tool in the contact areas. The full contact condition (very high value of the coefficient) gives the contact nods (in work piece and tool) the same temperature at each time step. As it is known, heat is transmitted only over rough spots which are in the contact together. The real contact area increases with plastic and elastic deformation of asperities due to the high normal stresses (high cutting velocity and feed rate). The resulting deformations increase the real contact area and respectively, the amount of heat transfer rate. Egana et al. [110] investigated experimentally to determine the heat portion coefficient in the machining of Ti-6Al-4V. They have found a heat portion ratio between 0.5- 0.6, a value which varies with temperature, contact velocity and contact pressure. The ratio decreases with the sliding velocity up to 0.3. The value at the higher temperature (at 1000 °C) is near to 0.6. At low cutting velocities based on the Egana et al. investigation, the heat transfer coefficient is estimated as a function of contact pressure (σ_n: N/mm^2):

$$h_{int} = 25 \exp\ (0.0001\ \sigma_n) \qquad \textbf{Equation 4-19}$$

Where the h_{int} is between 25 and 55 kW/m²K. For example at a cutting velocity of 120 m/min the calculated heat portion ratio at tool-work piece interface in simulation is 0.37 which is in good agreement. Generally, in the laser assisted machining, the contact pressure is lower than in conventional machining, which prevents high thermal damage in the tool. This

assumption helps to adjust the interface heat transfer coefficient at the different laser assisted machining conditions.

4.3 Simulation of LAM of Ti-6Al-4V

The commercial software DEFORM 3D has been used to set up a thermo-mechanical FEM model for the laser-assisted machining process. The implicit Lagrange mesh formulation provided can handle large deformations, but requires frequent re-meshing. The software supports automatic local re-meshing, based on the impacted weighting factors [97]. In the regions with high strain, strain rate and temperature, the generated mesh is finer (in the primary shear zone and the area near the tool tip). The model consists (Figure 4-17.a) of the work piece as a rigid-plastic part and the tool as a rigid body with tetrahedral elements for both. The thermal boundary conditions (convection and radiation) were considered by applying the convection heat transfer coefficients and the emissivity to all the elements with external contact. Tool movement was defined as rotation around the vertical axes and a constant velocity in the feed direction, while the coordinate system (mill center) moves according to the tool. The bottom surface of the work piece was fixed in three directions. The effect of process gas was considered by defining a heat transfer coefficient as the forced convection of 2000 W/m²K. The FEM simulation is capable of predicting the resulting forces as the work piece is impacted with the laser simultaneously (Figure 4-17.b).

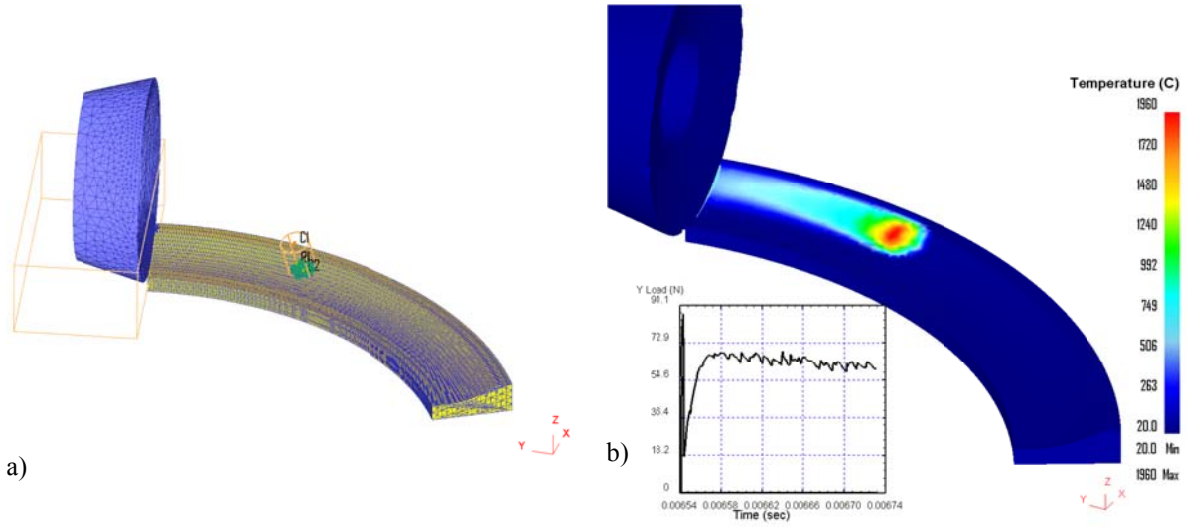

Figure 4-17: (a) 3D FE-model and boundary condition of laser-assisted-side milling process and (b) parallel calculation of cutting force.

4.3.1 Simulation Input

Table 4-3 shows the input data for the all the performed simulations. The same thermo-physical material properties for work piece and tool, frictional behavior and mesh characters including re-meshing criterion have been used. The laser assisted milling conditions (laser

power adjustment, feed rate and cutting velocity) have been corresponded to experimental investigation.

Table 4-3: Used input data for performed simulations.

	Inelastic heat fraction		0.9	
	Conductivity (W/mK)	Work piece (Ti6Al4V) [111]	T [° C]	W/mK
			25 500 900 995 1100 1650	7 12.6 20.2 19.3 21 28.4
		Tool (TiAlN-coated cemented carbide) [97]	T [° C]	W/mK
			25 1000	12 20
	Heat capacity (J/Kg K)	Work piece (Ti6Al4V) [111]	T [° C]	J/Kg K
			25 500 900 995 1100 1650	546 651 734 641 660 759
		Tool (TiAlN-coated cemented carbide) [97]	598	
Contact area	Heat transfer coefficient (kW/m²K)		$h_{int} = 25 \exp\ (0.0001\ \sigma_n)$	
	Friction coefficient	Rake face	$\bar{m}$= 0.7 μ= 0.5	
		Tool round face	$\bar{m}$=1	
		Clearance face	μ= 0.5	
	Friction energy transformed into heat		1	
Environment	Forced convection (Air jet cooling, Overhead) (W/m²K)		2000	
Milling conditions	Cutter		RDHX 0702 MOT	
	Cutting width(mm)		8	
	Rake angle (°)		11	
	Nose radius(mm)		0.02	
	Depth of cut (mm)		0.5	
	Cutting velocity(m/min)		25, 50, 75, 100	
	Rotation velocity of tool (rpm)		332, 663, 995, 1326	
	Feed (mm/rev)		0.05, 0.07, 0.09	
	Laser power (W)		536, 714, 893, 1071, 1250, 1428	
Work piece	Number of elements		319200	
	Weighting factors		strain	0.4
			strain rate	0.6
	Minimum element size (mm)		0.005, 0.007, 0.01	
	Size ratio		15	
Tool	Number of elements		25000	
	Minimum element size		0.0837	
	Size ratio		4	

4.3.2 Material Model Parameters

In order to provide a comparative study between the presented approaches (NTS) in this work, the simulation results are compared with the result achieved using the TANH model and also with the experimental results. The applied material constants are listed in Table 4-4.

Table 4-4: Material constants for TANH and NTS modified models.

Constants for NTS [41]	**Values**
A (MPa)	724
B (MPa)	683.2
C	0.035
m	1.0
n	0.47
T_m (°C)	1660
a_2	10^{-7}
b_2	2.9
m_0	1
$\dot{\alpha}$	10^{-4}

Constants for TANH [109]	**Values**
A (MPa)	724
B (MPa)	683.2
C	0.035
m	1.0
n	0.47
T_m (°C)	1660
a	2
b	5
c	2
d	1
e	0.05

4.3.3 Results

In order to validate the model, developed in the present work, the numerically calculated cutting forces were compared to the experimentally determined ones. The simulations have been done for different stands of the cutting velocity, feed rate and laser power.

Before starting the interpretation of mechanical results, the maximum temperature curve in the work piece during one tool rotation are illustrated in Figure 4-18. As it calculated in section 2.4, the laser power varied with respect to the entrance, exit and uncut chip thickness. The variation of laser power led to optimization of temperature profile in work piece. As it can be observed in Figure 4-18.a and .b, the peak temperature decreased from 1780 °C approximately 400 °C at end of the cutting insert rotation. For instance, in the represented laser assisted cutting condition (cutting velocity= 50 m/min, feed rate= 70 µm/rev, laser power= 1428 W), the surface melting was occurred only at beginning of cutting edge path, where the uncut chip thickness was large as well. With respect to this feature, the protection against unwanted phase transformations was ensured. Figure 4-18.c shows the temperature distribution in the work piece after one cutting insert revolution and just before the laser beam meets the work piece for second times. The work piece temperature ranged between 100°C and 175 °C. The according temperature distribution in the work piece varied depending on the applied laser power and performed machining conditions). Figure 4-18.d shows the temperature field, as the work piece was subjected for second times by the laser beam. The peak temperature on the laser spot surface increased slightly (around 1810 °C). The reason is that the thermo-physical properties of work piece changes with increasing the initial

temperature of work piece and consequently has an effect on the maximum laser spot temperature.

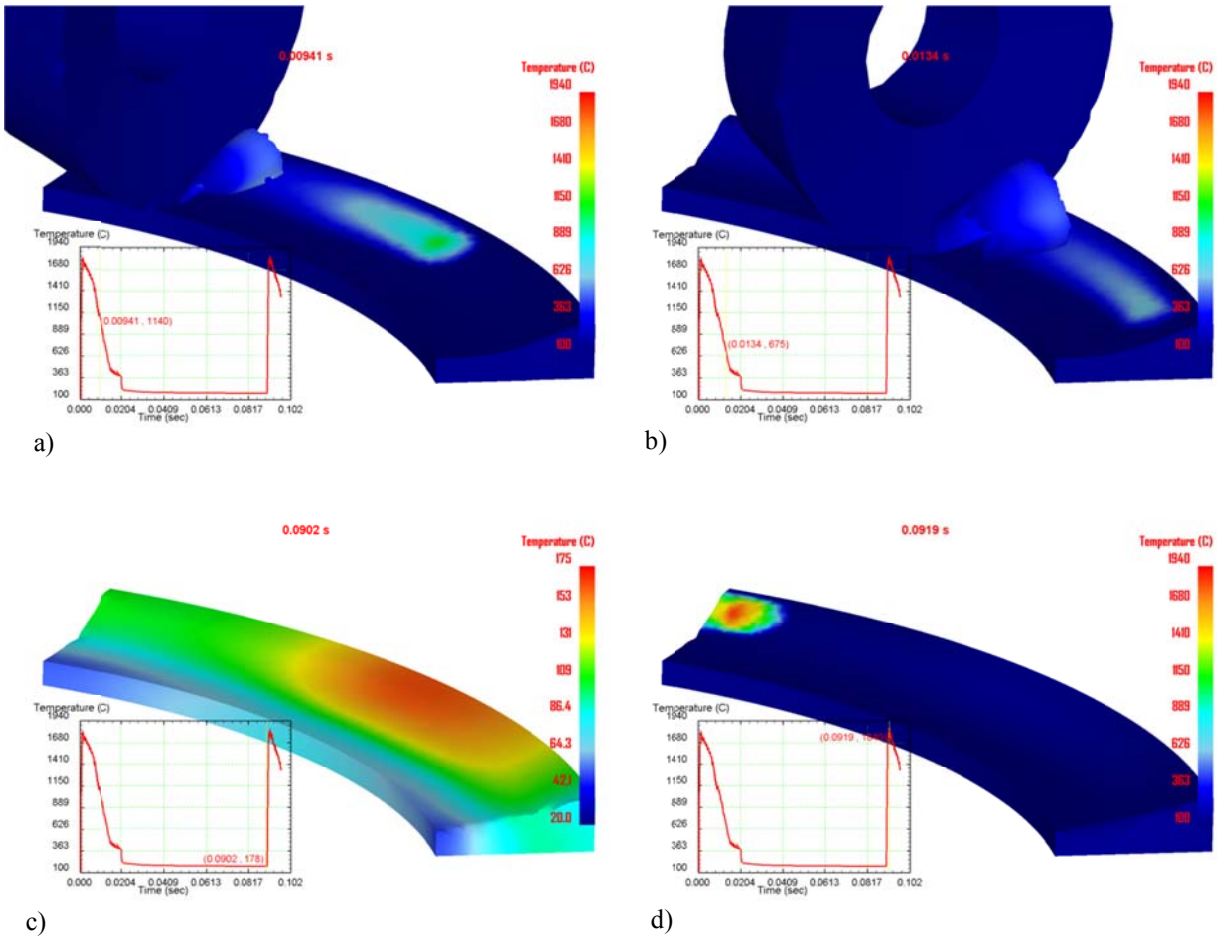

Figure 4-18: Temperature distribution and variation in work piece at (a) 0.00941, (b) 0.0134, (c) 0.0902 and 0.0919 s.

As concluded in the earlier section, 3D prediction of chip morphology requires a fine mesh. The small element size is not attainable in many cases of 3D simulation of cutting processes. Because of the large element size used in the simulations (minimum element size was between 0.007 -0.015 mm in the primary shear zone) the chip morphology in this process was not considered in standard cases. However, Figure 4-19 shows a typical difference between the achieving chip morphology in 3D simulation for the used Johnson-Cook model (NTS) and modified Johnson-Cook material model (TANH). The both simulations was carried out in the same cutting condition (cutting velocity= 50 m/min, feed rate= 90 µm/rev, laser power= 1428 W) and simulation input data (Table 4-3). Since the chip thickness decreases along the cutting edge line (the end side of chip is finer), tendency to rib is higher. The results indicated that the depth of ribs in the TANH predicted chip was higher than the Johnson-Cook based approach (NTS). The reason is that the chip undergoes more deformation than the Johnson-Cook based

approach (NTS). Figure 4-19.a illustrates the chip surface is more deformed than Figure 4-19.b.

The computed effective stresses for both material modeling approaches in the similar cutting conditions (cutting velocity= 50 m/min, feed rate= 70 µm/rev, laser power= 1428 W) are illustrated in Figure 4-20. Because of nonlinearity thermal softening at high strain rates, the effective stress decreased sharply with the temperature in case of NTS approach (Figure 4-20.b) comparing to the TANH approach (Figure 4-20.a). The laser spot with radius of 0.5 mm cannot cover the whole of the cutting edge. Hence, the effective stress was reduced only at the according area, where was subjected by the laser spot. Moreover, Figure 4-20 shows the effective stress at the non-affected area for NTS approach was higher than the TANH approach. Thus, the lower value of effective stress at the end of cutting edge for the TANH approach is major cause of the deformed chip with deeply penetrated ribs.

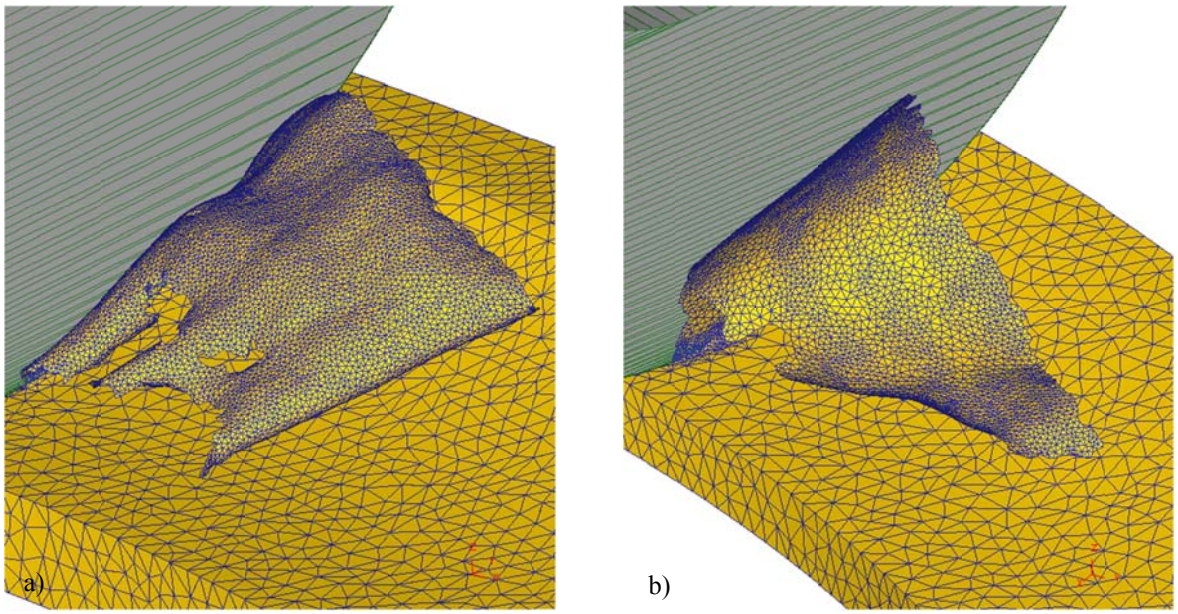

Figure 4-19: Typical chip morphology using (a) modified Johnson-Cook material model (TANH) and (b) applied Johnson- Cook approach.

The effective stress has a direct influence on the achieved cutting forces, as it can be observed in the load-time curves in Figure 4-20. Despite higher value of effective stress at the end of cutting edge line in the NTS approach, the global force was lower than the TANH one. The spontaneous jump of forces corresponded to the re-meshing procedure, which caused the interpolations failure. Using specific re-meshing (with defining specific weighting ratio at particular simulation steps) instead of automatic re-meshing, helped to decrease the number of occurred interpolation failure. The predicted forces reported in the histograms of Figure 4-21 and Figure 4-22 were obtained as maximum values of the load signals before the simulation approaches the steady state (in Figure 4-17.b, Figure 4-20.a and .b) for further calculations

such as temperature. A detailed explanation related to the determination of experimentally achieved cutting forces explained in section 2.6.

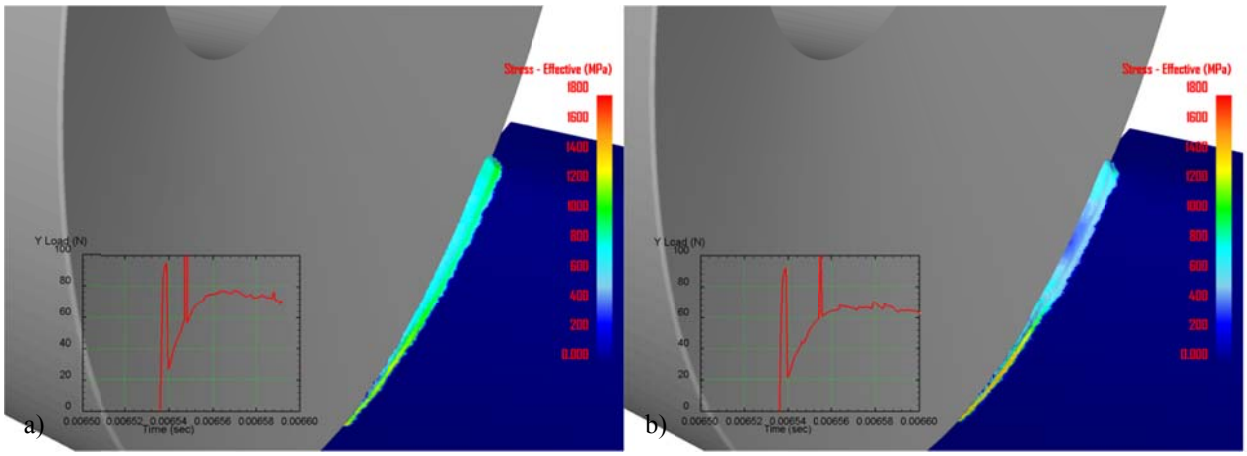

Figure 4-20: Effective stress distribution and calculated force using modified Johnson-Cook material model (TANH) and (b) applied Johnson- Cook approach (NTS).

As is observed in Figure 4-21 and Figure 4-22, the non-linear thermal softening at high strain rates (NTS) provides a wide range of validity for the simulation results. Contrary to NTS approach in material modeling, the TANH material model produces lower forces in case of machining without laser and is not capable of fairly predicting the varying force reduction with laser power. An excellent agreement for cutting forces in Y direction was found for the NTS material, modeling approach. In Figure 4-21 and Figure 4-22, the cutting forces in Y direction for laser power 0 W into laser power 893 W reduced sharply. This significant fall of forces could be predicted only with NTS approach. For example in Figure 4-22, difference between the forces in Y direction (between laser powers 0 and 893 W) are 24 N, 11 N and 28 N for experimental forces, TANH and NTS, respectively. The reason is that the linear thermal softening of the TANH material model which is not in accordance with the nature of thermal softening. By accepting that the force reduction in the laser assisted machining refers to the thermal softening effect, non-linear behavior of the force reduction justified the NTS approach. In Figure 4-21 for the laser powers more than 1428 W, the predictive forces in Y direction from the TANH approach did not decrease remarkable (between 1 and 2 N), while the achieved forces from NTS approach corresponded the experimental one.

The forces in Z direction showed a very good agreement for laser powers up to 1428-1607 W for both material modeling approaches. In Figure 4-21, at very high laser powers (1758 W), the experimentally achieved force in Z direction increased suddenly to 103 N, which is not in accordance with typical reduction of forces with the laser power. The reason is that the interface temperature between the cutting insert is very high (more than softening point of cutting insert material) at these laser powers, which increases the tool wear. As showed in section 2.6.2, the tool wear has a direct influence on the forces in Z direction.

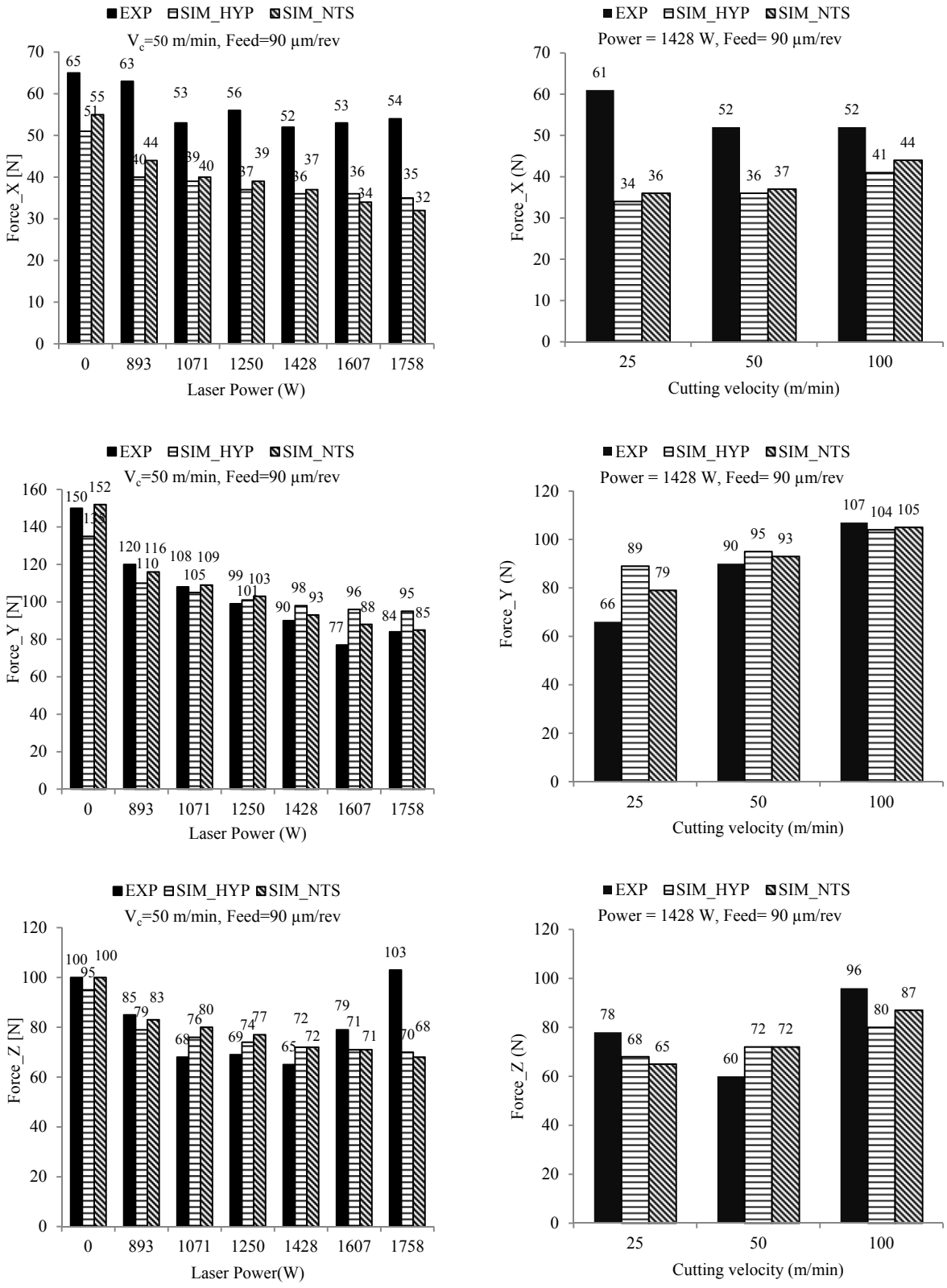

Figure 4-21: Comparison between simulated and measured milling forces with increasing laser power for used-JC-model (NTS) and TANH model (HYP).

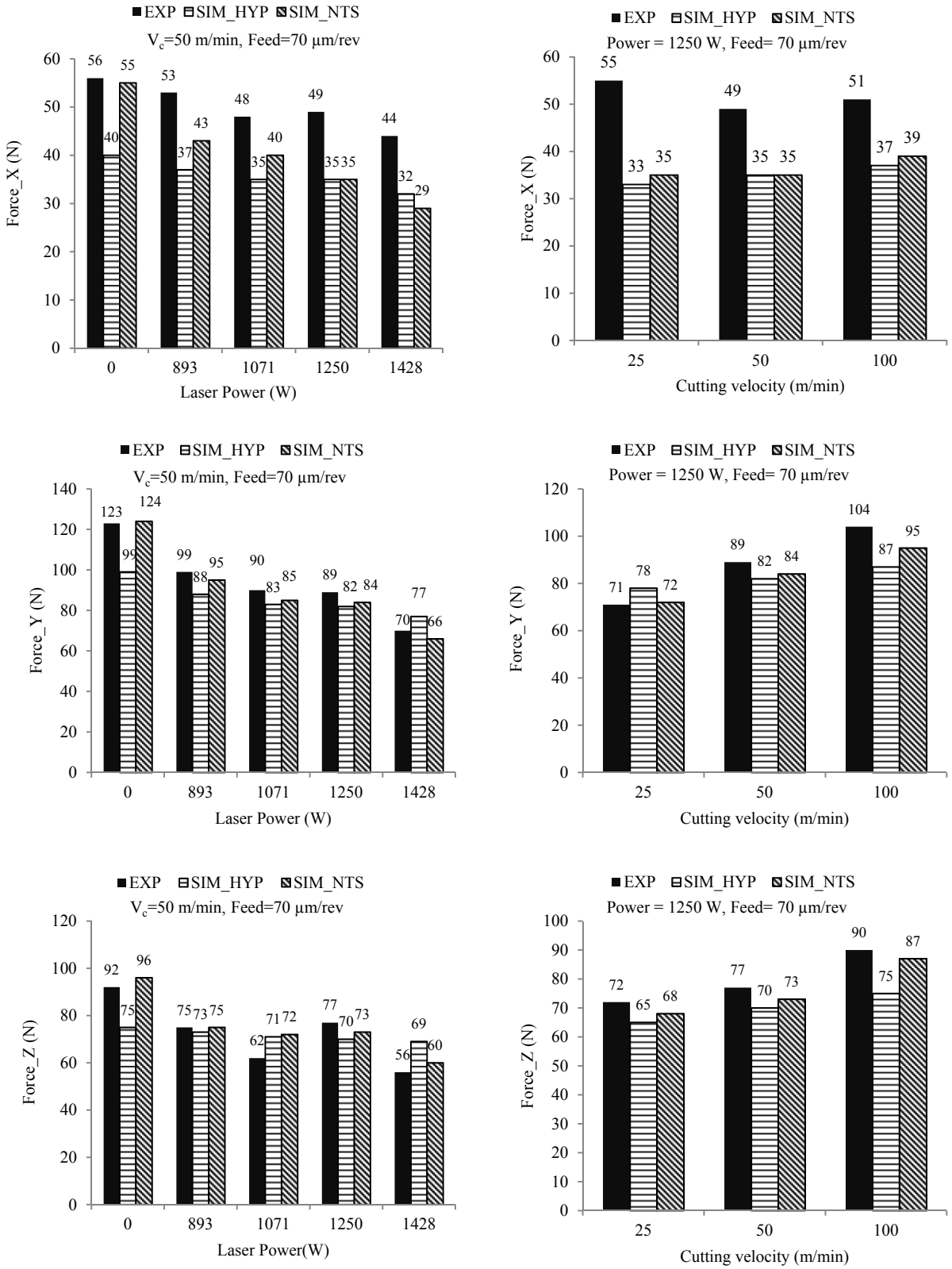

Figure 4-22: Comparison between simulated and measured milling forces with increasing laser power for used-JC-model (NTS) and TANH model (HYP).

The predicted the forces in X direction by the NTS approach showed very good agreement in case of without laser. However, the calculated reduction of forces in X direction is higher than the experimental results. The reason is that additionally to the mechanical workpiece strength, the value of cutting forces in X direction depends on the tool vibration and tool thrust. The dynamic properties of machine did not include in simulation and FEM results considered only the physical and mechanical material properties.

The simulation results validate that the developed thermo-mechanical FEM model for laser-assisted machining in the tested cutting conditions is robust and can be utilized for process optimization.

5 Conclusion and Outlook

The present research aims to develop and to optimize an integrated laser assisted tool machine system. The developed tool is based on the free propagation laser beam through the spindle. A modular tool with the mechanical interface (HSK 63) is connected to spindle which consists of a focal lens and a prism for deflecting the laser beam onto the working plane. The laser power is adjusted according to the tool entrance angle, tool exit angle, maximum chip thickness and minimum chip thickness. The developed machine was operated to the laser assisted side milling of Ti-6Al-4V alloy with the down (climb) strategy. Because of the potential phase transformation at high temperature, Ti-6Al-4V has been selected as a good choice for material that is hard to machine. The short term and long term of cutting forces in three directions were measured for the milling with and without laser, where the long term forces subsume the amount of tool wear indirectly. The process forces progressed slowly with the assistance of the laser beam during milling. The value of the three process forces decreased with the laser power in all of the conducted tests which shows that laser input significantly enhances the machinability for Ti-6Al-4V. The high force reduction-to-laser power ratio were achieved in combination with the laser powers up to 1428 W and low cutting velocities (25-50 m/min). In contrast, the laser powers more than 1428 W requires the high cutting velocities (100 m/min). Due to the potential of the chip melting and sticking with

the cutter tip, a very low feed rate interrupts the advantages of laser and especially for forces in the direction of normal to working plane.

In order to focus on the main core of the current research, the three common chip segmentation criterions were emphasized in the simulation of the machining process (modified Johnson-Cook model at high strains, Cock and Latham crack criterion and Johnson-Cook damage model) in comparison with the thermo-plastic shear instability. In this work, thermo-plastic shear instability was adjusted for the Johnson-Cook flow stress with finding a critical strain and for first time, the according approach was applied to simulate the serrated chip in the machining of Ti-6Al-4V. On the basis that the segmented chip in machining is as a result of the adiabatic shear and neither fracture nor the dynamic recrystallization can assume its responsibility. The shear instability was considered in term of frequency and power. It is assumed that as the shear instability happens, this instability tries to develop and present itself as an adiabatic shear band. The stronger shear instability (power) is less than the number of trials (frequency) to form a mature adiabatic shear. The introduced model was approved at the very low and very high cutting velocity in 2D orthogonal cutting simulations. A qualitative and comparative analysis was conducted in term of occurrence and the stage of adiabatic shear band. The microscopic cross sectional images of hot compression tests at two temperatures (600 and 750 °C) and two strain rates (0.01 and 1 s^{-1}) were verified the simulation results in 2D and 3D simulations. Since the constants of the Johnson-Cook material models determined in several studies and also covered a wide range of material spectrum, the applied approach can save cost of extra investigation and gives a good chance of finding the remaining constants in comparison with other models, especially, with the modified Johnson-Cook at high strains which also presents acceptable results.

In the next step, in order to reduce the computational costs (simulation interruptions) and realize shear instability effect even for large scale mesh, the present work provides a linking between thermal softening constant in the original Johnson-Cook model and a definition of shear instability. The thermal softening coefficient is not dropped not more linearly as the strain rate exceeds a critical value. According to a defined control volume (shear band thickness or an element size in FEM mesh) and not the sufficient time for heat transfer, the relating critical strain rate can be found. The model was adapted using several cutting force measurements in different cutting conditions and was utilized for the optimization of the real laser assisted side milling.

Also, first attempt was to develop and apply a completely coupled moving laser heat source with the mechanical simulation. Both analytical and numerical methods have been used for describing the transient thermal model. When defining a domain (as laser spot) with local boundary condition, the local convection coefficient approaches zero the virtual environmental temperature can be calculated directly from the laser power density by a very

small value of the convection coefficient. The model validated analytically and experimentally based on the estimated absorption coefficient.

Finally, a series of 3D simulations of laser assisted side milling for Ti-6Al-4V were selected to validate the full coupled thermo-mechanical model. The results are in very good agreement with the experimental results at diverse cutting conditions.

Despite of the good results regarding modeling and machinability improvement, further experimental investigations are well-intentioned. Increasing the number of tests for diverse strain rates and temperatures helps to find out the instability point with illustration variation of flow stress versus temperature. Also, the shear instability approach can be extended regarding phase transformation at 1050 °C using hot compression tests at related temperatures. And in the next, the approach can be applied to other materials which adiabatic shear is susceptible, for example Inconel 718 or AISI 4340 are proper materials.

From a machinability point of view, the productivity of process (material removal rate) can be improved by increasing the number of insert, as predicted in the cutting tool module also. These aspects first avoid possible surface damage at the high laser power and spread the material induced boundary conditions.

6 List of Figures

7 List of Tables

8 References

[1] S. P. F. C Jaspers, J. H. Dautzenberg, "Material behaviour in metal cutting: strains, strain rates and temperatures in chip formation," *Journal of Materials Processing Technology ,* vol. 121, pp. 123-135, 2002.

[2] T. Childs, K. Maekawa, T. Obikawa, Y. Yamane, Metal machining, theory and application, New York: John Wley & Sons, 2000.

[3] S. Jaspers, Metal cutting mechanics and material behaviour, Einhoven: Technische Universiteit Eindhoven, 1999.

[4] V. Kalhori, "Doctral thesis: modelling and simulation of mechanical cutting," LuLea Tekniska Universitet, Lulea, 2001.

[5] W. Grzesik, Advanced machining processes of metallic materials: theory, modeling and applications, Elsevier, 2008.

[6] A. Atkins, "Modelling metal cutting using modern ductile fracture mechanics:quantitative explanations for some longstanding problems," *International Journal of Mechanical Sciences ,* vol. 45 , p. 373–396, 2003.

[7] F. Klocke, W. König, Fertigungsverfahren 1, Drehen, Fräsen, Bohren, Aachen: Springer, 2008.

[8] S. Sun, M.Brandt, M.S.Dargusch,, "Characteristics of cutting forces and chip formation in machining of titanium alloys," *International Journal of Machine Tools & Manufacture,* vol. 49, p. 561–568, 2009.

[9] R. Komanduri, B.F. Von Turkovich, "New observations on the mechanism of chip formation when machining titanium alloys," *wear,* vol. 69, no. 2, p. 179–188, 1981.

[10] Z. B. Hou, R. Komanduri, "Modeling of themomechanical shear instabiity in machining," *International Journal of Mechanical Sciences,* vol. 39, no. 11, pp. 1279-1314, 1997.

[11] J. Huang, W. W. Olson, J. W. Sutherland, E. C. Aifantis, "On the shear instbility in chip formation in orthogonal machining," *Journal of the Mechanical Behaviour of Materials,* vol. 7, no. 4, pp. 279-292, 1996.

[12] R. Komanduri, Z.-B. Hou , "On thermoplastic shear instability in the machining of a titanium alloy (Ti-6Al-4V)," *Metallurgical and Materials Transactions A,* vol. 33, no. 9, pp. 2995-3010 , 2002.

[13] E. M. Trent, P. K. Wright, Metal cutting, Woburn: ButterWorth-Heinemann, 2000.

[14] P. L. B. Oxley, The mechanics of machining: an analytical approach to assessing machinability, Kensington: Ellis horwood limited, 1989.

[15] N. Fang, "Slip-line modeling of machining with a rounded-edge tool—part I: new model and theory," *Journal of the Mechanics and Physics of Solids,* vol. 51, p. 715 – 742, 2003.

[16] N. Fang, P. Dewhurst,, "Slip-line modeling of built-up edge formation in machining," *International Journal of Mechanical Sciences,* vol. 47, p. 1079–1098, 2005.

[17] B. Li, X. Wang, Y. Hu, C. Li, "Analytical prediction of cutting forces in orthogonal cutting using unequal division shear-zone model," *The International Journal of*

Advanced Manufacturing Technology , vol. 54, pp. 431-443, 2011.

[18] B. Shi, H. Attia, N. Tounsi, "Identification of material constitutive laws for machining—part I: an analytical model describing the stress, strain, strain rate, and temperature fields in the primary shear zone in orthogonal metal cutting," *Journal of Manufacturing Science and Engineering,* vol. 132, pp. 051008-1-11, 2010.

[19] B. Shi, H. Attia, N. Tounsi, "Identification of material constitutive laws for machining—part II: generation of the constitutive data and validation of the constitutive law," *Journal of Manufacturing Science and Engineering,* vol. 132, pp. 051009-1-9, 2010.

[20] N. Tounsi, J. Vincenti, A. Otho, M.A. Elbestawi, "From the basic mechanics of orthogonal metal cutting toward the identification of the constitutive equation," *International Journal of Machine Tools & Manufacture ,* vol. 42, p. 1373–1383, 2002.

[21] M. Shatla, C. Kerk, T. Altan, "Process modeling in machining, part I: determination of flow stress data," *International Journal of Machine Tools & Manufacture,* vol. 41, p. 1511–1534, 2001.

[22] M. Shatla, C. Kerk, T. Altan, "Process modeling in machining, part II: validation and applications of the determined flow stress data," *International Journal of Machine Tools & Manufacture,* vol. 41, p. 1659–1680, 2001.

[23] Y. Huang, S.Y. Liang, "Cutting forces modeling considering the effect of tool thermal property-application to CBN hard turning," *International Journal of Machine Tools & Manufacture ,* vol. 43 , p. 307–315, 2003.

[24] A. H. Adibi-Sedeh, V. Madhavan, B. Bahr, "Extension of Oxley's analysis of machining to use different material models," *Journal of Manufacturing Science and Engineering,* vol. 125, pp. 656-666, 2003.

[25] D. I. Lalwani, N.K. Mehta, P.K. Jain, "Extension of Oxley's predictive machining theory for Johnson and Cook flow stress model," *Journal of Materials Processing Technology,* vol. 209, p. 5305–5312, 2009.

[26] A. O. Tay, M. G. Stevenson, G. de V. Davis, "Using the finite element methode to determine temperature distribution in orthogonal machining," *Applied Mechanics Group,* vol. 188, no. 55/74, pp. 627-638, 1974.

[27] A. J. Shih, "Finite element simulation of orthogonal metal cutting," *Journal of Engineering for Industry,* vol. 117, pp. 84-93, 1995.

[28] T. Özel, E. Zeren, "Finite element modeling the influence of edge roundness on the stress and temperature fields induced by high-speed machining," *The International Journal of Advanced Manufacturing Technology ,* vol. 35, p. 255–267, 2007.

[29] D. Umbrello, "Finite element simulation of conventional and high speed machining of Ti6Al4V alloy," *Journal of Materials Processing Technology,* vol. 196, p. 79–87, 2008.

[30] T. D. Marusich, M. Ortiz, "Modelling and simulation of high-speed machining," *International Journal For Numerical Methods in Engineering,* vol. 38, pp. 3675-3694, 1995.

[31] J. Lorentzon, N. Jarvstrat, "Modelling tool wear in cemented-carbide machining alloy 718," *International Journal of Machine Tools & Manufacture,* vol. 48, p. 1072– 1080, 2008.

[32] J. C. Outeiro, J. C. Pina. R. M. Saoubi, F. Pusavec, I.S. Jawahir, "Analysis of residual stresses induced by dry turning of difficult-to-machine materials," *CIRP Annals - Manufacturing Technology ,* vol. 57, p. 77–80, 2008.

[33] Marıa H. Miguelez, A. M. Sachez, J. L. Cantero, J. A. Loya, "An efficient implementation of boundary conditions in an ale model for orthogonal cutting," *Journal of Theoretical and Applied mechanics,* vol. 47, no. 3, pp. 599-616, 2009.

[34] O. B. Adetoro, P. H. Wen, "Prediction of mechanistic cutting force coefficients using ALE formulation," *The International Journal of Advanced Manufacturing Technology ,* vol. 46, pp. 79-90, 2010.

[35] P. M. Dixit, U. S. Dixit, Modeling of metal forming and machining processes by finte element and soft computing methods, london: Springer, 2008.

[36] V. Schulzea, F. Zanger, "Numerical Aanalysis of the influence of Johnson-Cook material parameters on the surface integrity of Ti-6Al-4V," *Procedia Engineering,* vol. 19, p. 306 – 311, 2011.

[37] J. Shi, C. R. Liu, "The influence of material models on finite element simulation of machining," *Journal of Manufacturing Science and Engineering,* vol. 126, pp. 849-857, 2004.

[38] P. J. Arrazola, D. Ugarte, X. Domınguez, "A new approach for the friction identification during machining through the use of finite element modeling," *International Journal of Machine Tools & Manufacture,* vol. 48 , p. 173–183, 2008.

[39] G. Shi, X. Deng, C. Shet, "A finite element study of the effect of friction in orthogonal metal cutting," *Finite Elements in Analysis and Design,* vol. 38, p. 863–883, 2002.

[40] T. Childs, "Friction modelling in metal cutting," *Wear,* vol. 260 , p. 310–318, 2006.

[41] W. S. Lee, C. F. Lin, "Plastic deformation and fracture behaviour of Ti–6Al–4V alloy loaded with high strain rate under various temperatures," *Materials Science and Engineering ,* vol. A241 , p. 48–59, 1998.

[42] A. Attanasio, M. Gelfi, A. Pola, E. Ceretti, C. Giardini, "Influence of material microstructures in micromilling of Ti6Al4V alloy," *Materials,* vol. 6, pp. 4268-4283, 2013.

[43] R. Filip, K. Kubiak, W. Ziaja, J. Sieniawski, "The effect of microstructure on the mechanical properties of two-phase titanium alloys," *Journal of Materials Processing Technology ,* vol. 133, p. 84–89, 2003.

[44] E. O. Ezugwu, Z. M. Wang, "Titanium alloys and their machinability-a review," *Journal of Materials Processing Technology,* vol. 68, pp. 262-274, 1997.

[45] E. Ezugwu, "Key improvements in the machining of difficult-to-cut aerospace superalloys," *International Journal of Machine Tools & Manufacture,* vol. 45, p. 1353–1367, 2005.

[46] P. J. Arrazola, A. Garay, L. M. Iriarte, M. Armendia, S. Marya, F. Le Maître, "Machinability of titanium alloys (Ti6Al4V and Ti555.3)," *Journal of Materials Processing Technology,* vol. 209, p. 2223–2230, 2009.

[47] N. Fang, Q. Wu, "A comparative study of the cutting forces in high speed machining of Ti–6Al–4V and Inconel 718 with a round cutting edge tool," *Journal of Materials Processing Technology ,* vol. 209 , p. 4385–4389, 2009.

[48] E. Abele, B. Fröhlich, "High speed milling of titanium alloys," *Avances in Production Engineering & Management,* vol. 3, pp. 131-140, 2008.

[49] E. O. Ezugwu, J. Bonney, Y. Yamane, "An overview of the machinability of aeroengine

alloys," *Journal of Materials Processing Technology,* vol. 134, p. 233–253, 2003.

[50] J. Hua, R.Shivpuri, "A cobalt diffusion based model for predicting crater wear of for predicting crater Wear of Titanium alloys," *Transactions of the ASME,* vol. 127, pp. 136-144, 2005.

[51] C. Brecher, M. Emonts, C. J. Rosen, J. P. Hermani, "Laser-assisted milling of advanced materials," *Physics Procedia,* vol. 12, p. 599–606, 2011.

[52] S. Sun, M. Brandt, M. S. Dargusch, "Thermally enhanced machining of hard-to-machine materials—a review," *International Journal of Machine Tools & Manufacture,* vol. 50, p. 663–680, 2010.

[53] C. J. Rosen, Laserunterstützte Fräsbearbeitung hochfester Werkstoffe, Aachen: Apprimus Verlag, 2012.

[54] C. Brecher, C. J. Rosen, C. Wenzel, S. Bausch, "Fräsen von Hochleistungskeramik, Hybride Prozess- und Systemtechnologie für eine effiziente spanende Materialbearbeitung," *Wt Werkstattstechnik Online,* vol. 99, no. 3, pp. 177-185, 2009.

[55] C. Brecher, C. J. Rosen, L. Beegen, C. Wenzel, "Systemtechnik zum Fräsen hochfester Werkstoffe, Hybride Spindel-Werkzeugtechnologie für die laserunterstützte Zerspanung," *Wt Werkstattstechnik Online,* vol. 99, no. 10, pp. 793-800, 2009.

[56] C. Brecher, C. J. Rosen, D. Lindemann, M. Emonts, "Prozesssteuerung für laserunterstützte Fräsbearbeitung, Energieeffizienz und Bearbeitungsflexibilität durch Echtzeit-Synchronisation von Laser und Spanungsprozess," *Wt Werkstattstechnik Online Jahrgang,* vol. 100, no. 5, pp. 338-345, 2010.

[57] C. Brecher, M. Emonts, M. Seidler, J. -P. Hermani, B. Sonderegger, H. Zamani, T. Wenzel, A. Pätz, B. Heinemann, A. Walter, G. Toesko, T. Rineck, H. Fissmer, P. Temme, S. Friedl, J. Thieme, „TooLAM-2. Projektstatustreffen: Entwicklung adaptiver Werkzeugsysteme für die laserunterstützte Fräsbearbeitung von schwerzerspanbaren Werkstoffen," WZL/Fraunhofer IPT, Wendelstein, 21. October.2011.

[58] J. Sieniawski, W. Ziaja, K. Kubiak and M. Motyka, "Microstructure and mechanical properties of high strength two-phase Titanium alloys," *InTech,* no. http://dx.doi.org/10.5772/56197, pp. 69-80, 2013.

[59] S. Sun, M. Brandt, M. S. Dargusch, "The effect of a laser beam on chip formation

during machining of Ti6Al4V alloy," *Metallurgical and Materials Transactions ,* vol. A41, p. 1573–1581, 2010.

[60] G. Germain, F. Morel, J. l. Lebrun, A. Morel, "Machinability and surface integrity for a bearing steel and a Titanium alloy in laser assisted machining," *Lasers in Engineering,* vol. 17, p. 329–344, 2007.

[61] C. R. Dandekar, Y. C.Shin, J. Barnes , "Machinability improvementof titanium alloy (Ti–6Al–4V) via LAM and hybrid machining," *International Journal of Machine Tools & Manufacture,* vol. 50, p. 174–182, 2010.

[62] S. Sun, J. Harris, M. Brandt, "Parametric investigation of laser-assisted machining of commercially pure titanium," *Advanced Engineering Materials,* vol. 10, pp. 565-572, 2008.

[63] K. Krastel, Konzepte und Konstruktionen zur laserintegrierten Komplettbearbeitung in Werkzeugmachinen, Universität Stuttgart: Herbert Utz Verlag. Wissenschaft, 2002.

[64] M. Born, E. Wolf, Principles of optics, Oxford: Pergamon Press, 1986.

[65] A. Walter, Interviewee, *Personal comunication.* [Interview]. 2013.

[66] C. Brecher, M. Emonts, M. Seidler, J. P. Hermani, B. Sonderegger, H. Zamani, T. Wenzel, A. Pätz, B. Heinemann, A. Walter, G. Toesko, T. Rineck, H. Fissmer, P. Temme, S. Friedl, J. Thieme, "TooLAM-3. Projektstatustreffen: Entwicklung adaptiver Werkzeugsys für die laserunterstützte Fräsbearbeitung von schwerzerspanbaren Werkstoffen," WZL/Fraunhofer IPT, Aachen, Aachen, 25. Mai 2012.

[67] C. Brecher, M. Emonts, M. Seidler, J. P. Hermani, B. Sonderegger, H. Zamani, T. Wenzel, A. Pätz, B. Heinemann, A. Walter, G. Toesko, T. Rineck, H. Fissmer, P. Temme, S. Friedl, J. Thieme, "TooLAM-5. Projektstatustreffen: Entwicklung adaptiver Werkzeugsys für die laserunterstützte Fräsbearbeitung von schwerzerspanbaren Werkstoffen," WZL/Fraunhofer IPT, Aachen, 24. Mai 2013.

[68] C. Brecher, M. Emonts, M. Seidler, J. P. Hermani, B. Sonderegger, H. Zamani, T. Wenzel, A. Pätz, B. Heinemann, A. Walter, G. Toesko, T. Rineck, H. Fissmer, P. Temme, S. Friedl, J. Thieme, "TooLAM-1. Projektstatustreffen: Entwicklung adaptiver Werkzeugsys für die laserunterstützte Fräsbearbeitung von schwerzerspanbaren Werkstoffen," WZL/Fraunhofer IPT, Aachen, 20 Mai 2011.

[69] C. Brecher, C. J. Rosen, S. Bausch, "Mehrachsige laserunterstützte Fräsbearbeitung, Leistungsfähige Fertigung komplexer Bauteilgeometrien aus schwer zerspanbaren Werkstoffen," *Wt Werkstattstechnik Online,* vol. 100, no. 11/12, pp. 892-896, 2010.

[70] C. Brecher, M. Emonts, M. Seidler, J. -P. Hermani, B. Sonderegger, H. Zamani, T. Wenzel, A. Pätz, B. Heinemann, A. Walter, G. Toesko, T. Rineck, H. Fissmer, P. Temme, S. Friedl, J. Thieme, "TooLAM-4. Projektstatustreffen: Entwicklung adaptiver Werkzeugsys für die laserunterstützte Fräsbearbeitung von schwerzerspanbaren Werkstoffen," WZL/Fraunhofer IPT, Graz, 31. Oktober 2012.

[71] H. Zamani, J. P. Hermani, B. Sonderegger, C. Sommitsch, "3D Simulation and process optimization of laser assisted milling of Ti6Al4V," *Procedia CIRP,* vol. 8, pp. 75 - 80, 2013.

[72] H. Zamani, J. P. Hermani, B. Sonderegger, C. Sommitsch, "Numerical and experimental investigation of laser assisted side milling of Ti6Al4V alloy," in *The Materials Science & Technology 2012 Conference and Exhibition proceedings*, Pittsburgh, Pennsylvania, 2012.

[73] Y. Huang, S. Y. Liang, "Modeling of cutting forces under hard turning conditions considering tool wear effect," *Journal of Manufacturing Science and Engineering,* vol. 127, pp. 262-270, 2005.

[74] H. Zamani, J. P. Hermani, B. Sonderegger, C. Sommitsch, "3D simulation of laser assisted side milling of Ti6Al4V alloy using modified Johnson-Cook material model," *Key Engineering Materials,* Vols. 554-557, pp. 2054 - 2061, 2013.

[75] G. R. Johnson, W. H. Cook, "A constitutive model for metals subjected to large strains, high strain rates and high temperatures," in *Proceedings of the Seventh International Symposium on Ballistics 54*, Hague, Netherlands, 1983.

[76] W. S. Lee, C. F. Lin, "High-temperature deformation behaviour of Ti6Al4V alloy evaluated by high strain-rate compression tests," *Journal of Materials Processing Technology,* vol. 75, p. 127–136, 1998.

[77] H. W. Meyer, D. S. Kleponis, "Modeling the high strain rate behavior of titanium undergoing ballistic impact and penetration," *International Journal of Impact Engineering,* vol. 26, p. 509–521, 2001.

[78] G. Kay, "Failure modeling of Titanium-61-4V and 2024-T3 Aluminum with the

Johnson-Cook material model," Lawrence Livermore National Laboratory, 2003.

[79] S. Seoa, O. Min, H. Yanga, "Constitutive equation for Ti–6Al–4V at high temperatures measured using the SHPB technique," *International Journal of Impact Engineering,* vol. 31, p. 735–754, 2005.

[80] M. Jutras, "Master of science thesis: improvement of the characterisation method of the Johnson-Cook model," Defence Research and Development for Canada (DRDC) Valcartier, Universite Laval Quebec, 2008.

[81] T. W. Wright, The physics and mathematics of adiabatic shear bands, Cambridge University Press, 2002.

[82] M. Calamaz, D. Coupard, F. Girot, "A new material model for 2D numerical simulation of serrated chip formation when machining titanium alloy Ti–6Al–4V," *International Journal of Machine Tools & Manufacture,* vol. 48 , p. 275–288, 2008.

[83] M. Sima,T. Oezel, "Modified material constitutive models for serrated chip formation simulations and experimental validation in machining of titanium alloy Ti–6Al–4V," *International Journal of Machine Tools & Manufacture,* vol. 50, p. 943–960, 2010.

[84] D. Rittel and Z. G. Wang, "Thermo-mechanical aspects of adiabatic shear failure of AM50 and Ti6Al4V alloys," To Appear in Mechanics of Materials , Faculty of Mechanical Engineering Technion, Haifa, 2008.

[85] D. Rittel, "A different viewpoint on adiabatic shear localization," *Journal of Physics D: Applied Physics,* vol. 42, p. 214009 (6pp), 2009.

[86] C. Z. Duan, M.. Wang, Y. J. Cai, T. Dou, "Microcosmic mechanism of material softening and fracture in primary shear zone during high speed machining of hardened steel," *Materials Science and Technology,* vol. 27, no. 3, pp. 625-630, 2011.

[87] J. Peirs, W. Tirry, B. Amin-Ahmadi, F. Coghe, P. Verleysen, L. Rabet, D. Schryvers, J. Degrieck, "Microstructure of adiabatic shear bands in Ti6Al4V," *Materials Characterization,* vol. 75, p. 79–92, 2013.

[88] M. G. Cockcroft, , D. J. Latham, "Ductility and the workability of metals," *Journal of the Institute of Metals,* vol. 96, p. 33–39, 1968.

[89] J. Hua, R. Shivpuri, "Prediction of chip morphology and segmentation during the machining of titanium alloys," *Journal of Materials Processing Technology,* vol. 150 ,

p. 124–133, 2004.

[90] M. Jutras, "Master of science thesis: improvement of the characterization method of the Johnson-cook model," Research and Development for Canada (DRDC), 2008.

[91] C. A. Essig, "Dissertation: Vorhersage von Spanbruch bei der Zerspanung mit geometrisch bestimmter Schneide mit Hilfeschädigungsmechanischer Ansätze," RWTH Aachen University,, Aachen, 2010.

[92] H. Sadeghinia, M.R. Razfar, J. Takabi, "2D finite element modeling of face milling with damage effects," in *3rd WSEAS International Conference on Applied and Theoretical Mechanics*, Spain, 2007.

[93] C. Duan, L. Zhang, "A reliable method for predicting serrated chip formation in high-speed cutting: analysis and experimental verification," *The International Journal of Advanced Manufacturing Technology,* vol. 64, no. 9-12, pp. 1587-1597, 2013.

[94] Y. C. Zhang, T. Mabrouki, D. Nelias, Y. D. Gong , "Chip formationin orthogonal cutting considering inter facelimiting shear stress and damage evolution based on fracture energy approach," *Finite Elements in Analysis and Design,* vol. 47, p. 850–863, 2011.

[95] Y. L. Bai, "Thermo-plastic instability in simple shear," *Journal of the Mechanics and Physics of Solids,* vol. 30, no. 4, pp. 195-207, 1982.

[96] M. N. Raftenberg, "A Shear Banding Model for Penetration Calculations," Army Research Laboratory, 2000.

[97] "Deform-user manual SFTC-Deform V10.0.2," Columbus (OH), USA, 2010.

[98] N. N. Zorev, "Inter-relationship between shear processes occurring along tool face and shear plane in metal cutting," *International Research in Production Engineering ASME,* pp. 42-49, 1963.

[99] G. G. Ye, S. F. Xue, M.Q. Jiang, X. H. Tong, L. H. Dai, "Modeling periodic adiabatic shear band evolution during high speed machining Ti-6Al-4V alloy," *International Journal of Plasticity,* vol. 40, p. 39–55, 2013.

[100] J. Yanga, S. Suna, M. Brandt, W.Yan, "Experimental investigation and 3D finite element prediction of the heat affected zone during laserassisted machining of Ti6Al4V

alloy," *Journal of Materials Processing Technology,* vol. 210, p. 2215–2222, 2010.

[101] B. Dodd,Y. Bai, Adiabatic shear localization, frontiers and advances, Elsevier Ltd, 2012.

[102] H. J. Frost, M. F. Ashby, Defomation mrchanism maps, the plasticity and creep of metals and ceramics, Pergamon Press, 1982.

[103] S. Kobayashi, S. I. OH, T. Altan, Metal forminf and the finite-element method, New york: Oxford University Press, 1989.

[104] N. B. Dahotre, S. P. Harimkar, Laser fabrication and machining of materials, Springer, 2008.

[105] J. M. Dowden, The mathematics of thermal modeling, an introduction to the theory of laser material processing, Chapman&Hall/CRC, 2001.

[106] D. Bergström, A. Kaplan, J. Powell, "Mathematical modelling of laser absorption mechanisms in metals: a Review," in *M4PL16 - 16th Meeting on Mathematical Modelling of Materials Processing with Lasers*, 2003.

[107] W. Pitscheneder, "Contributions to the understanding and optimazation of laser surface alloying," Department of physical metallurgy and materials testing, University of Leoben, 2001.

[108] M. Boivineau, C. Cagran, D. Doytier, V.Eyraud, M. -H. Nadal, B.Wilthan, G. Pottlacher, "Thermophysical properties of solid and liquid Ti-6Al-4V (TA64) Alloy," *International Journal of Thermophysics,* vol. 27, no. 2, pp. 507-529, 2006.

[109] D. Ulutan, M. Sima, T. Özel, "Prediction of machining induced surface integrity using elastic-viscoplastic simulations and temperature-dependent flow softening material models in Titanium and Nickel-based alloys," *Advanced Materials Research,* vol. 223, pp. 401-410, 2011.

[110] A. Egana, J. Rech, P. J. Arrazola, "Characterization of friction and heat partition coefficients during machining of a TiAl6V4 Titanium alloy and a cemented carbide," *Tribology Transactions,* vol. 55, pp. 665-676, 2012.

[111] J. Yanga, S. Sun, M. Brandt, W. Yan, "Experimental investigation and 3D finite element prediction of the heat affected zone during laser assisted machining of Ti6Al4V

alloy," *Journal of Materials Processing Technology,* Vols. 210,, no. 15, p. 2215–2222, 2010.